

Alma Mater Studiorum - Università di Bologna

**DOTTORATO DI RICERCA IN
INGEGNERIA ELETTROTECNICA**

Ciclo XXVII

Settore Concorsuale di afferenza: 09/E2

Settore Scientifico disciplinare: ING-IND/32

**ANALYSIS AND DESIGN OF HIGH
PERFORMANCE MULTIPHASE
ELECTRIC DRIVES FOR VEHICLE
AND AIRCRAFT APPLICATIONS**

Presentata da: GIANCARLO RINI

Coordinatore Dottorato
Prof. Domenico Casadei

Relatore
Prof. Giovanni Serra

Esame finale anno 2015

TABLES OF CONTENTS

Preface	7
Chapter 1 Tools for automation electromagnetic finite element analysis about rotating electrical machines	10
1.1 Introduction	10
1.2 Finite Element Analysis with FEMM	11
1.2.1 Partial Differential Equations	11
1.2.2 Magnetostatic Problem	12
1.3 About "Lua Motor"	13
1.3.1 Aims of Lua Motor	13
1.3.2 Using the "Lua Motor"	15
1.3.3 Construction of Geometric Models	17
Chapter 2 Analysis of Synchronous Machine with External Rotor for "Emilia 3" Solar Car	22
2.1 Summary of the PMSM design details	23
2.1.1 Cogging Torque	24
2.1.2 No Load condition	25
2.1.3 Load condition	27
2.2 Experimental result	29
Chapter 3 Developments about More Electric Aircraft	30
3.1 Introduction	30
3.2 More Electric Aircraft (MEA)	32
3.3 Power generator	36
3.3.1 Generating power at constant frequency	37
3.3.2 Generating power at variable frequency	38
3.4 More Electric Engine (MEE)	38
3.5 System Security	41
3.5.1 Drive for flight control application	42
3.5.2 Electromechanical Actuators (EMA)	43
3.5.3 Electric-Hydraulic Actuator (EHA)	44
3.6 Electric Fuel Pump	46
3.7 On board Power Generation	46
3.8 Regeneration energy onto the electrical power bus	47
3.8.1 Local energy dissipation	48

3.8.2	Centralized energy storage	48
3.8.3	Return energy to the source	49
3.9	Multi-Phase Drivers and Machine	50
Chapter 4	Design of a Multiphase Induction Machine for an Open Rotor Aero-Engine Shaft Line Embedded Starter/Generator.....	52
4.1	Abstract	52
4.2	Introduction	53
4.3	Open rotor Jet Engines	53
4.4	Fault tolerant multi-phase drives	54
4.5	Machine Design Criteria	56
4.6	Design Procedure	56
4.7	Target design ad prototype	59
4.8	Equivalent Circuit Parameters Measurements	63
4.8.1	No Load Tests	63
4.8.2	Locked rotor tests	67
4.9	Load Test and Validation of the Simulations	68
4.10	Prototype Performance Comparisons	70
4.11	Conclusions	73
Chapter 5	Dynamic Stator Current Sharing in quadruple Three-Phase Induction Motor Drive.....	76
5.1	Abstract	76
5.2	Introduction	77
5.3	Quadruple three-phase induction machine	78
5.3.1	Machine Model	79
5.3.2	Three-Phase space vector	81
5.3.3	Multiple Space Vectors	81
5.4	Stator and current sharing control strategy	82
5.5	Control Scheme	83
5.5.1	Torque and Rotor Flux Control	84
5.5.2	Auxiliary Stator Current Control	84
5.5.3	Modulation Strategy of the Four Three-phase Inverters	86
5.6	Simulation Results	86
5.7	Conclusion	90
Chapter 6	A Modulation Strategy for Matrix Converter with Extended Control Range and Reduced Switching Power Losses.....	92
6.1	Abstract	92
6.2	Introduction	92

6.3	A Review of the Modulation Strategy for Matrix Converters	94
6.4	Extension of the operating range	97
6.5	Optimization of the Switching Losses	98
6.5.1	Switching Losses	99
6.6	Simulation Result	102
6.7	Experimental Result	106
6.8	Conclusion	108
Chapter 7	Modulation Strategy with Minimum Switching Losses for Three-Phase AC-DC Matrix Converters	110
7.1	Abstract	110
7.2	Introduction	110
7.3	Modulation Strategy for AC/DC Matrix Converters	112
7.3.1	Input Output Equations of the AC/DC Matrix Converters	112
7.3.2	Input-Output Equations in Terms of Space Vectors	113
7.3.3	Control Range of the output Voltage	114
7.4	Improvement in the Switching Losses and Output Current Ripple	116
7.4.1	General Expression of the Switching Losses	116
7.4.2	Optimal Zero Sequence Component for the Reduction of the Switching Losses	117
7.4.3	Optimal Expression of the Switching Losses	119
7.4.4	Numerical Simulations	119
7.5	Experimental Results	123
7.6	Conclusion	123
Final Conclusion		125
List of the main Used acronyms		127
References		128
Appendix A		137
Hardware		137
Driver Board		137
Power Board		147
List of paper of Giancarlo Rini		153

PREFACE

In the transport sector the "more electric" solutions are gaining attention in order to reduce energy and increase efficiency and reliability and at the same time to reduce emissions and maintenance costs. Many examples can be found: from road transport, where hybrid electric vehicles are gaining popularity, to the sea transport, where the electric drive propulsion system is a very active and fast-growing research area. In this general frame, aerospace applications have found that the progressive electrification of on-board services is a way to reduce or to remove the dependence on hydraulic, mechanical and the bleed air/pneumatic systems.

The technological process in the transport sector has brought significant improvements. Currently it is expected a continuation of this growth, especially as regards the freight traffic. They are, therefore, considerable pressures from aviation manufacturers for the improvement of new aircraft in terms of safety, emissions and noise. Growing interest to adopt new technologies on board the aircraft, and it is widely agreed that the entire aviation system should be profoundly rethought. In this sense, the concept of greatest impact on the architecture of the aircraft is summed up in the expression More Electric Aircraft (MEA), which indicates the increasing adoption of electrical systems instead of conventional hydraulic, pneumatic and mechanical systems.

For the future it is expected that the new generation of civil aircraft require high electrical power to meet the growing demand for electrical loads of the aircraft. And then next to the MEA concept is born the More Electric Engine (MEE), in which one or more electrical machines integrated into the engine aeronautical performing functions of generation and start-up.

In order to use the MEA/MEE, the most important technology is undoubtedly the power electronics. However, aerospace applications present some challenging conditions for electronic systems; There are still a number of studies to be carried out to make improvements in terms of weight, cost and reliability of the systems. A significant improvement in machines and electric drives for applications MEA can certainly come from the use of multi-phase drives.

The field of study of multiphase machines is a relatively new field and in great development, but it is already possible to say that these machines are able to provide better performance than three phase. This technology, is characterized by a number of issues that make it attractive in comparison to conventional systems.

Multiphase systems, allow to redistribute power at a higher number of phases, thus making possible the construction of electronic converters which otherwise would be very difficult to achieve due to the limits of present power electronics. Multiphase drive have an intrinsic reliability thanks to the fact that a failure on one phase, caused by the possible failure of a component of the converter, can be solved by reducing performance of the machine.

The control of the magnetic spatial harmonics in the air-gap with order higher than one allows to reduce torque noise and to obtain high torque density motor.

The aerospace specific requirements in terms of lightness, reliability, cost, fault tolerance, fault propagation, harsh ambient conditions and standard compliance have challenged the body of knowledge and the creativity of the electrical designers both in the industry and academic environments. In the past years many EU projects and initiatives have been developed to explore the MEA/MEE concepts. The research results have already brought to the development of many electric devices that are now installed in large civil aircraft by Airbus and Boeing, which are the beginning of the adoption of the MEA concept.

During the Ph.D. course several themes have been developed that, while obtaining the recent and growing interest of scientific community, have much space for the development of research activity and for industrial applications.

Chapter 1

TOOLS FOR AUTOMATION ELECTROMAGNETIC FINITE ELEMENT ANALYSIS ABOUT ROTATING ELECTRICAL MACHINES

1.1 INTRODUCTION

The initial purpose of these first activity was to develop some tools for automating electromagnetic finite element analysis of rotating electrical machines.

The analysis of a generic electromagnetic structure consists in the study of the distribution of the electromagnetic fields that develop inside the structure studied and particularly so in the region of the air gap.

Usually one of the first steps to be taken in the design of rotating electrical machine, is the geometric design in a CAD (Computer-Aided Design). In fact, consolidated knowledge of CAD applications have to dedicate a lot of time to both the design of the lamination geometric (which could also show complex geometry) that the setting of the relevant physical parameters responsible for simulation development environments prone to simulation (FEMM by David Maker, Flu By Cedrat, MagNet By Infolytica, etc.).

These operations are repetitive but essential and in this context we find the development of a software package that automates the operations, giving easy access to the simulations and a safe time savings.

In particular the work done personally has been the development of a software that integrates directly with FEMM (open source software for analysing electromagnetic finite element) and automatically generate some geometries of laminations relative to rotating electrical machines.

In order to achieve the result shown in this discussion, reference was made to the knowledge assodate thanks to the courses of machines and electrical drives, performing a job analysis of the problems closely related to the design of such machines. In this work has been supported a study of the tools necessary for the development of the software and in particular the techniques of parametric design.

The results were the basis of the development of "**Lua Motor**" as they have allowed to associate with specific aspects of the design of electric machines and computer tools that enable the creation of parametric models.

The global solution obtained is therefore the result of a survey aimed at obtaining tools characterized by ease of use and reliability of the results, these features allowed thanks to the knowledge of both aspects of the design, electromagnetic and computer science. These qualities make the software developed a useful and important in the design phase of machines and electrical drives.

1.2 FINITE ELEMENT ANALYSIS WITH FEMM

FEMM (Finite Element Method Magnetics) is a suite of programs for solving low frequency electromagnetic problems on two-dimensional planar and axisymmetric domains. The program currently addresses linear/nonlinear magnetostatic problems, linear/nonlinear time harmonic magnetic problems, linear electrostatic problems, and steady-state heat flow problems.

FEMM is divided into three part:

1. Pre-processor
2. Solver
3. Post-Processing

The Pre-Processor sets the problem both from a geometrical point of view, and to a physical point of view, defining the materials and the boundary conditions of the system.

The phase Solver consists in analysis to the computer calculations necessary to the solution of the problem.

The phase of Post-Processor allows, finally, an accurate analysis of the results obtained.

1.2.1 PARTIAL DIFFERENTIAL EQUATIONS

FEMM addresses some limiting cases of Maxwell's equations. The magnetics problems addressed are those that can be considered as "low frequency problems," in which displacement currents can be ignored. Displacement currents are typically relevant to magnetics problems only at radio frequencies.

1.2.2 MAGNETOSTATIC PROBLEM

Magnetostatic problems are problems in which the fields are time-invariant. In this case, the field intensity (H) and Flux Density (B) must obey:

$$\nabla \times H = J \quad (1-1)$$

$$\nabla \cdot B = 0 \quad (1-2)$$

subject to a constitutive relationship between B and H for each material:

$$B = \mu H \quad (1-3)$$

If the material is nonlinear (e.g. saturating Iron or AlNiCo magnets), the permeability, μ is actually a function of B:

$$\mu = \frac{B}{H(B)} \quad (1-4)$$

FEMM goes about finding a field that satisfies (1-1) - (1-3) via a magnetic vector potential approach. Flux Density is written in terms of the vector potential, A, as:

$$B = \nabla \times A \quad (1-5)$$

Now, this definition of B always satisfies (1-2). Then, **(1-1)** can be rewritten as:

$$\nabla \times \left(\frac{1}{\mu(B)} \nabla \times A \right) = J \quad (1-6)$$

For a linear isotropic material (and assuming the Coulomb gauge $\nabla \cdot A = 0$), eq. (1-6) reduces to:

$$-\frac{1}{\mu} \nabla^2 A = J \quad (1-7)$$

FEMM retains the form of (1-6), so that magnetostatic problems with a nonlinear B-H relationship can be solved.

In the general 3-D case, A is a vector with three components. However, in the 2-D planar and axisymmetric cases, two of these three components are zero, leaving just the component in the "Out of the page" direction.

The advantage of using the vector potential formulation is that all the condition to be satisfied have been combined into a single equation. If A is found, B and H can then be deduced by differentiating A. The form (1-6), an elliptic partial differential equation, arises in the study of many different types of engineering phenomenon.

1.3 ABOUT "LUA MOTOR"

The program created for the satisfaction of the features set out above, "Lua Motor", was developed through the Visual Basic .NET language. Visual Basic .NET (VB.NET) is a multi-paradigm, high level programming language, Implemented on the .NET Framework.

The software "Lua Motor" allows you to create a generic plate of a motor directly in FEMM. Along with this software have created a set of libraries ready to interface with FEMM using another language, Lua (Version 4.0). So it's easy to understand how it is possible to create a design abandoning the traditional method (mouse and keyboard) in favour of a programming approach.

The possibilities of using these two languages cover a wide range of applications but in this case only a small part of them have been exploited. This discussion will be given particular attention given to the problems concerning geometric constructions, especially in view finite element study.

1.3.1 AIMS OF LUA MOTOR

Verified the usefulness of the software capable of generating the drawing, it is important to establish the characteristics that it must possess.

First, the software needs to be **effective** and therefore must perform a correct drawing corresponding to reality and compatible to the needs of the remaining simulation environment.

Second, the software must be **easy to use** (user-friendly), that is capable of being able to build the chart pattern starting with little information that must be able to be communicated to the application in a simple and intuitive.

The ease of use also involves the efficient management of the errors that may occur, due, for example, the inconsistencies of the data provided by the user.

In response to these needs the software has a series of solutions, listed below, which have led to the final result shown in this discussion:

- To ensure the efficiency of the software and a correct execution of the design has been conducted a study on the geometric construction of the different types of laminations which the application is able to generate. Have been identified for each type of design of the basic parameters (and not redundant so as to minimize the number) on which you can go to reconstruct the whole geometry of the sheet. This was achieved by identifying the Cartesian coordinates of each point necessary for the construction of lines and arcs of a circle belonging to the design and making use of trigonometric and algebraic tools. This will ensure that the fundamental equations obtained, the design generated based on the starting parameters provided by the user always corresponds to what it really means to represent.
- Compatibility with both development environments (Lua Motor and FEMM) has necessitated the creation of geometries specifically designed for the simulation program and the possibility to store some data, related to the design generated in text files with a specific structure.
- The first aspect of ease of use, that is the opportunity to create the drawing starting with little information, is closely linked with the first of the points outlined here and also justifies the reason for the minimization of the basic parameters. The user, in fact, to be able to realize the design, will only have to indicate some specific measures for the sheet of interest.
- The simplicity of communication with the program suggested the importance of the development of a graphic interface able to guarantee a simple procedure for the input of data, as well as the possibility of using text files, as well as an interface for FEMM , also as a data base from which to quickly recall previously created projects.

Importantly, it has come to the development of such solutions gradually and in response to the needs that, carrying on the work, were to occur.

At first it has been an increased attention to the development of that part of the software that allow to generate the drawing (Library Lua) and immediately with it has been taken into consideration the possibility of creating interface files. At this stage of development are followed those concerning the graphical interface.

1.3.2 USING THE "LUA MOTOR"

The first step to use Lua Motor is run the file LuaMotor.exe on a Windows Operating System. After launching the application will open the GUI (Graphical User Interface), see Figure 1-1.

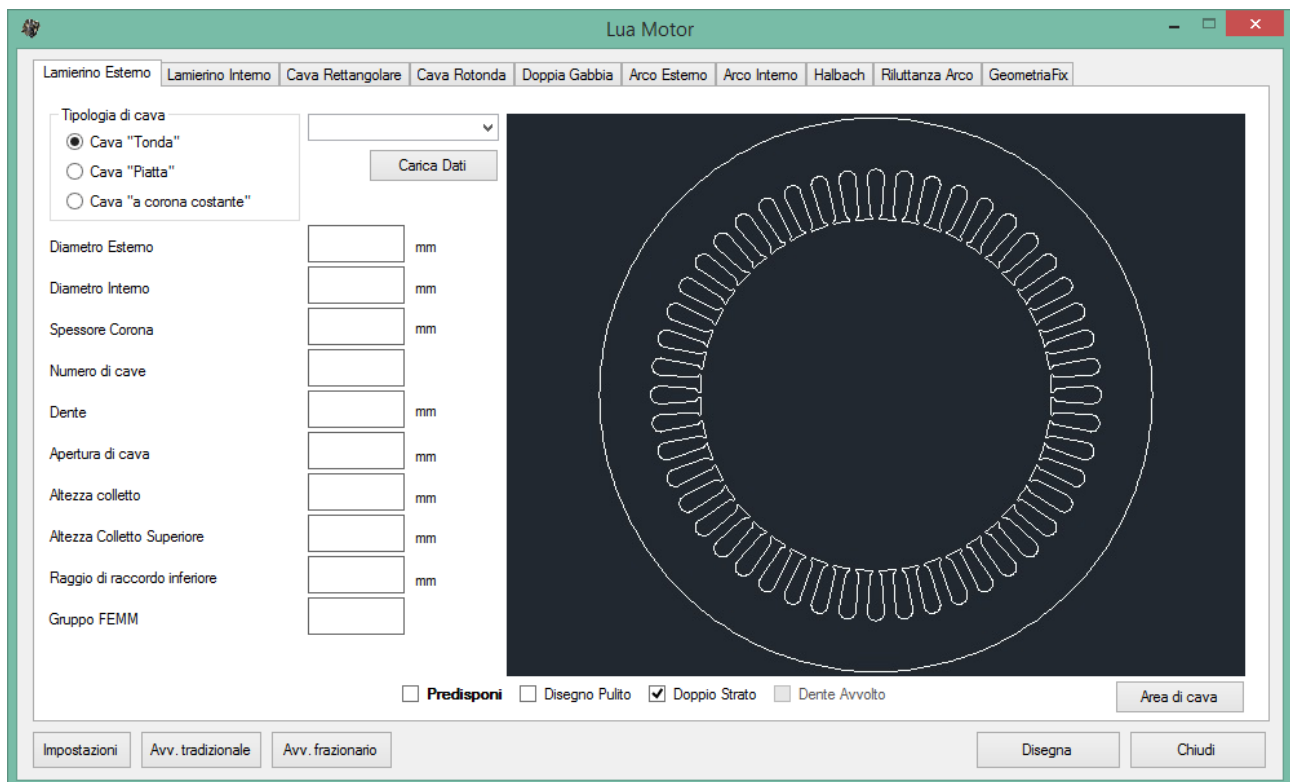


Figure 1-1 - GUI of Lua Motor

Lua motor is divided into several sections. Each section has parameters to be set in order to create a correct geometry. these parameters are visible on the left side of the GUI. In the upper part of the GUI can select the various types of sheet lamination to be generated by acting on the tabs in the figure below.



Figure 1-2 - Types of sheet lamination in Lua Motor

For the realization of a design you can manually enter the data required in their respective fields, or they can be called up via the import function, from projects previously created.

In case you follow this second procedure is necessary to go to select a project among those saved using the Combo-Box.

Once the filling of fields with the appropriate data can generate the design simply by clicking the "Disegna" button, remembering before you specify a name for the export file in the Combo-Box

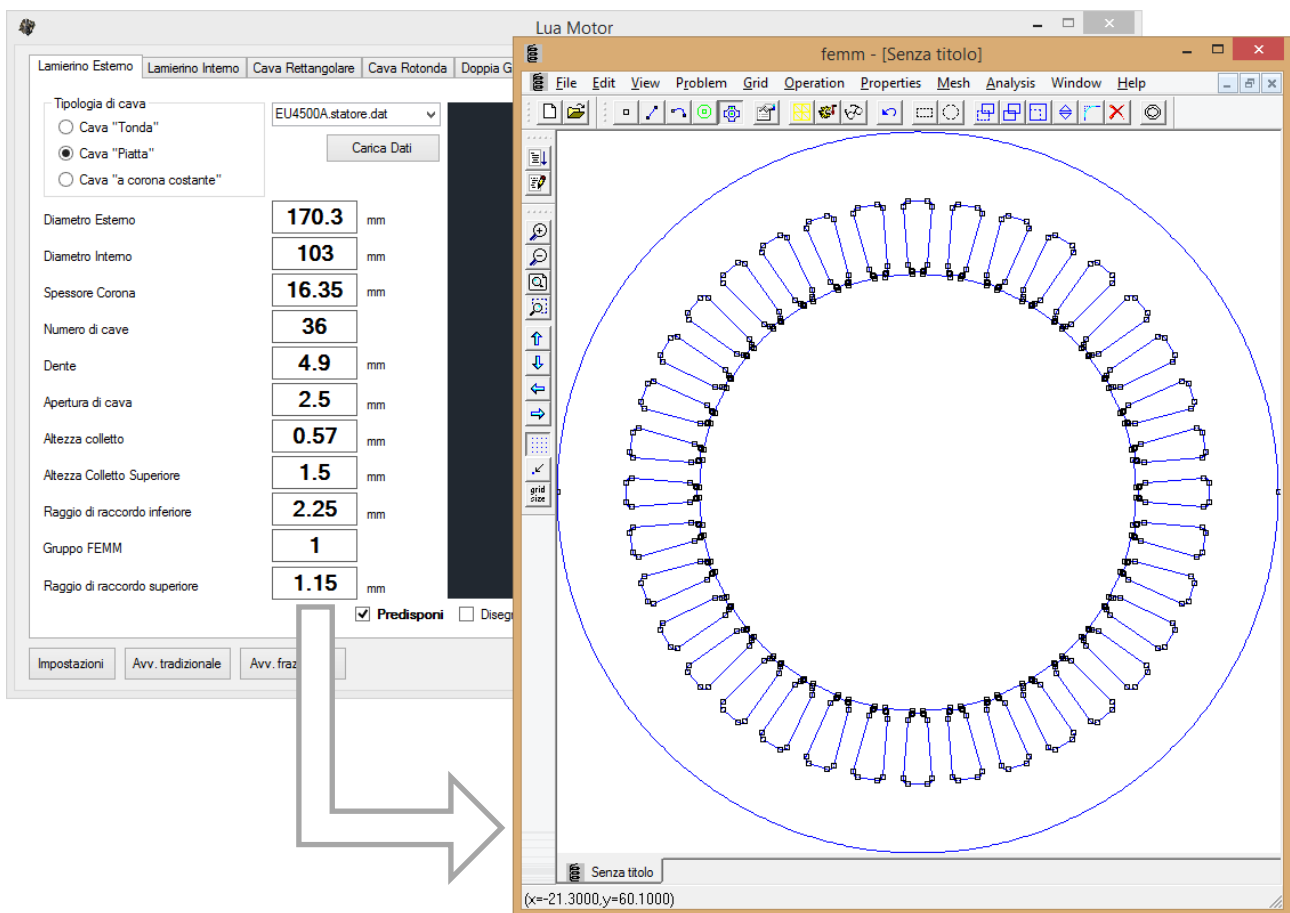


Figure 1-3 - Example of creation of lamination sheet

When this operation is completed, immediately displays the result in FEMM, see Figure 1-3.

Any operation is not performed correctly, such as the failure to specify a name for the export file, is duly reported by the program. The design generated can then be saved in .dxf file which is used other program based on Finite Element Analysis such as Flux, MagNet etc. The Lua Motor besides generating the exact geometry of the sheet lamination, it creates also several text files. This files has a dual function:

- constitute an interface between FEMM and other files for analysis of electromagnetic electrical machines

- as a database of projects

These .txt files are automatically saved in folders created in order to organize these files in a correct mode.

1.3.3 CONSTRUCTION OF GEOMETRIC MODELS

The current version of Lua Motor is able to generate different types of sheet in order to study:

- Asynchronous machines
 - Inner rotor with single cage or double cage
 - External rotor with single cage
- Synchronous machines
 - Inner rotor
 - External rotor
 - Hallbach rotor
 - Inner reluctance rotor (SynRM)

As can be seen the software is able to cover a large number of cases of different types of electrical machines.

To analyse an asynchronous electrical machine it is necessary to have all geometric details about sheet lamination and the characteristics of materials used.

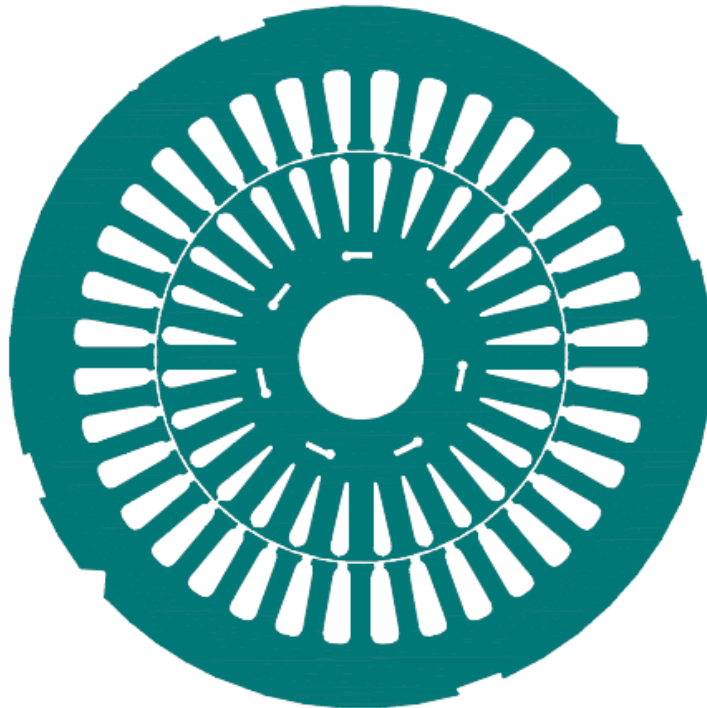
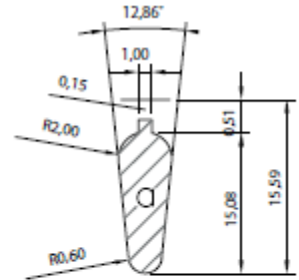
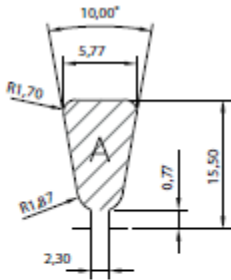


Figure 1-4 - Example of induction machine (4 poles)



IEC.90/4.80.2 Lamierini tranciati - Macchine asincrone **SA135P** **RA080P CPK**

DE mm	DI mm	N	A mmq	LD mm	LC mm	LS mm	AC mm
135,00	80,00	36	69,40	3,60	12,00	0,00	2,30

de mm	n	a mmq	ld mm	ac mm
80,00	28	39,80	4,40	1,00

#	RI	GR	SA	MT	PT	RF	V	P ₁ mm g
4		✓				✓	✓	52
5		✓				✓		52,21

#	di mm	pz	c	l	fv	ri	P ₁ mm g
1	25	✓					26,43
2	30	✓					24,75
5	30						24,75

Figure 1-5 - Example of induction machine (4 poles)

Lamierino Esterno | Lamierino Interno | Cava Rettangolare | Cava Rotondo

Tipologia di cava: IEC.90.4.80.Statore.dat

Cava "Tonda"
 Cava "Piatta"
 Cava "a corona costante"

Carica Dati

Diametro Esterno: 135 mm
 Diametro Interno: 80 mm
 Spessore Corona: 12 mm
 Numero di cave: 36
 Dente: 3.6 mm
 Apertura di cava: 2.3 mm
 Altezza colletto: 0.77 mm
 Altezza Colletto Superiore: 1.5 mm
 Raggio di raccordo inferiore: 1.87 mm
 Gruppo FEMM: 1
 Raggio di raccordo superiore: 1.7 mm

Predispo

Impostazioni | Avv. tradizionale | Avv. frazionario

Lamierino Esterno | Lamierino Interno | Cava Rettangolare | Cava Rotondo

Tipologia di cava: IEC.90.4.80.Rotore.dat

Cava "Tonda"
 Cava "Piatta"

Carica Dati

Diametro Esterno: 79 mm
 Diametro Interno: 25 mm
 Spessore Corona: 11.41 mm
 Numero di cave: 28
 Dente: 4.4 mm
 Apertura di cava: 1 mm
 Altezza colletto: 0.51 mm
 Altezza Colletto Superiore: 1 mm
 Raggio di raccordo inferiore: 2 mm
 Gruppo FEMM: 2

Predispo

Impostazioni | Avv. tradizionale | Avv. frazionario

Figure 1-6 - Example of induction machine (4 poles)

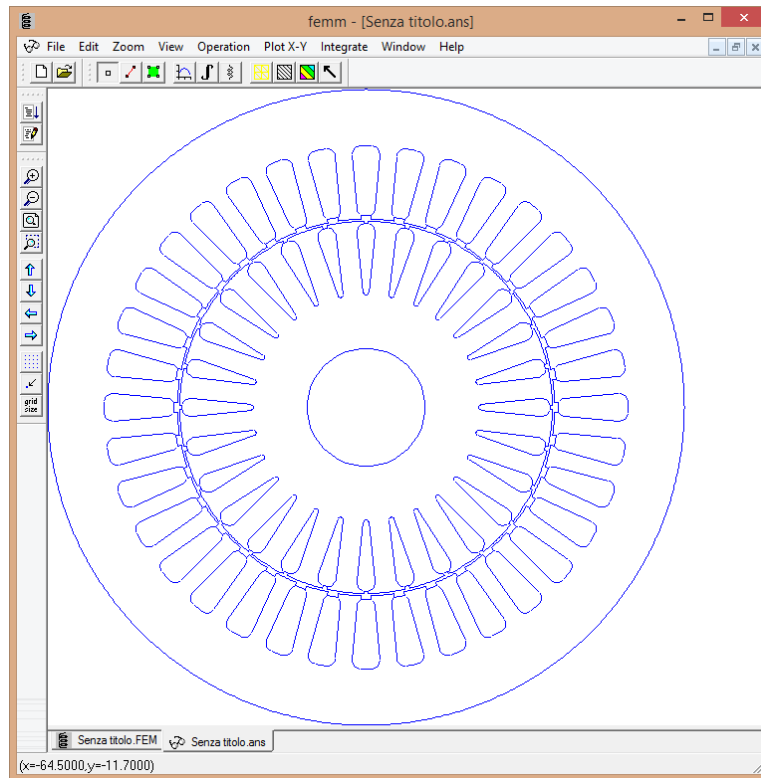


Figure 1-7 – Result of Lua Motor in FEMM application

In Figure 1-5, Figure 1-6 and Figure 1-7 is possible to see the correct design flow of a machine. The first step is to extract the all required parameters from Lua Motor for automatic generation of design. In this case are:

- For the stator
 - External diameter
 - Internal diameter
 - Thickness yoke
 - Number of slots
 - Slot opening
 - Thickness edge

for the rotor the same data. In total there is about twenty parameters to set.

Software Lua Motor is able to generate all the nodes, lines, arcs and circles to the automatic creation of the drawing. To do this, the software based on some key nodes (see Figure 1-8), selected on chosen by the parameters entered and slot type, goes to create lines and arcs to define the geometry.

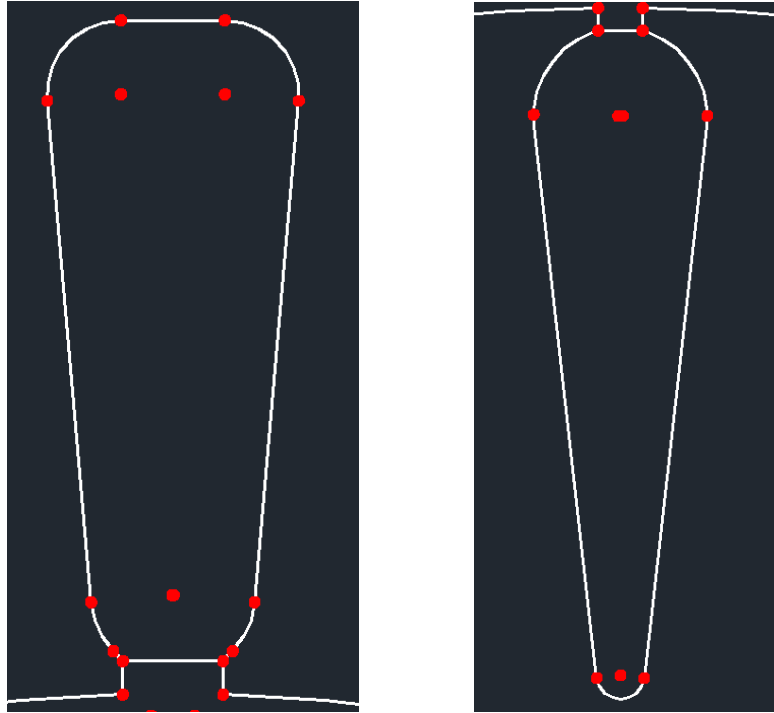


Figure 1-8 - Key nodes to generate the exact geometry for two types of slots ("Cava Piatta" for the stator (left picture) and "Cava Tonda" for the rotor (right picture))

Lua Motor also allows to create the regions of space destined to allocate the windings, both in the case of winding a single layer and double layer.

The work presented in this argument has related to the realization of the software Lua Motor.

The program was designed with the aim to simplify and accelerate of the operations necessary for the study of finite element rotating electrical machines and practical applications have proven their effectiveness.

There is perfect compatibility between software packages designed making them useful tools and simple to use and free.

The development of these tools has been possible thanks to the knowledge of the theories regarding the machines and electric drives but equally important role was played by the acquisition of knowledge and skills in the field of computer programming. The simultaneous attention to aspects electrical and computer has allowed to obtain a complete product complex but not able to meet in a comprehensive manner the needs of electromagnetic design.

Although the software package is fully functional, it is only a base which, although strong, is bound to and significant future expansions. The continuous evolution of the sector, in fact, raises the need for new types of laminations.

Just in anticipation of a future development I conceived the Lua Motor as a modular software, so as to make it easily expandable with the addition of new models without changing anything of what already exists.

Chapter 2

ANALYSIS OF SYNCHRONOUS MACHINE WITH EXTERNAL ROTOR FOR "EMILIA 3" SOLAR CAR

A permanent magnet synchronous motors (PMSM) are widely used in automotive applications and in industrial sector of medium and low power application.

A synchronous electric motor is an AC motor in which, at steady state, the rotation of the shaft is synchronized with the frequency of the supply current; the rotation period is exactly equal to an integral number of AC cycles. Synchronous motors contain multiphase AC electromagnets on the stator of the motor that create a magnetic field which rotates in time with the oscillations of the line current. The rotor with permanent magnets or electromagnets turns in step with the stator field at the same rate and as a result, provides the second synchronized rotating magnet field of any AC motor.

The brushless motor is an electric motor that in contrast to a DC motor, has no need of sliding electrical contacts on the motor shaft to work (hence the name "brushless"). The commutation of the current flowing in the windings, in fact, is not made by mechanically, but through electronic devices, with the consequence of a lower mechanical strength, eliminating the possibility of forming sparks, with increasing speed of rotation. With this type of engines is significantly reduced the need for periodic maintenance.

From an energy point of view, the brushless motors dissipate heat better than an AC motor. The absence of copper on the rotor and the presence of the windings on the stator allows to realize machines without cooling fins. This is because the Joule losses are only due to the stator windings.

These characteristics make them suitable for use in the aircraft industry, automotive, in marine and increasingly popular hybrid vehicles or electric vehicles.

In this chapter, I will describe the design of a brushless machine. The engine has been designed, manufactured and tested. The engine is directly mounted in a wheel, through a direct coupling (direct drive). The synchronous machine will be part of the one vehicle powertrain salt Italian who has successfully participated in the World Solar Challenge 2013 (WSC2013) and the Abu Dhabi Solar Challenge 2015 (ADSC2015). The vehicle has completed over 4000km road proving in fact the correct design of the electric motor.

2.1 SUMMARY OF THE PMSM DESIGN DETAILS

The Permanent Magnets Synchronous machine (PMSM) consists of 20 magnets and 18 slots. The PM Material adopted is NdFeB having a coercitivity of $H_c = 780 \text{ kA/m}$ and relative permeability $\mu_r = 1.07$.

The 18 slot - 20 pole structure with non-overlapping concentrate winding was adopted. The $2\pi/3$ electrical shift between coil sides results in magnetically de-coupled windings. Triplen harmonic are naturally eliminated in the single phase EMF. The main dimension and parameters are reported in Table 2-1.

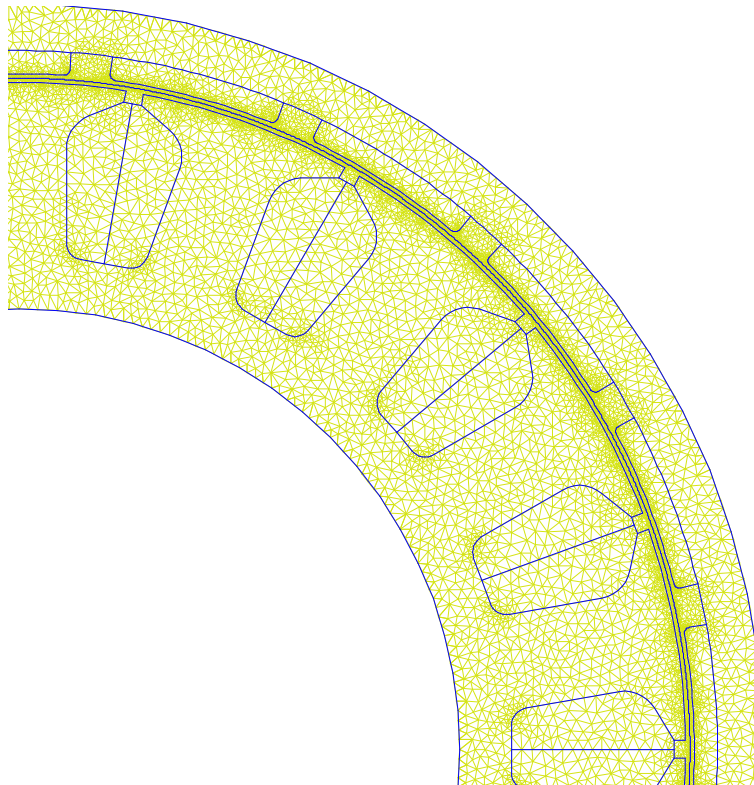


Figure 2-1 - Finite Element Model: solution mesh

In Figure 2-1 it is possible to see the finite element model used for the analysis. Circumferential magnet segmentation is considered as a standard technique to reduce the magnet eddy

current losses, but in this case it isn't necessary to divide the magnetics because this motor cannot be used at high speed (< 1000rpm).

The main features of the used materials are listed below:

- Magnets => Material: NdFeB, $H_c = 780 \text{ kA/m}$, $\mu_r = 1.07$
- Stator/rotor core => Laminated non-oriented silicon steel
- Copper => Resistivity $\rho = 2.15e - 8 \Omega\text{m}$

Torque (S1)	14 [Nm]
Max Torque	45 [Nm]
Rated Voltage	105 [V]
Type of connection	Star connection
Number of poles	20
Rated speed	805 [rpm]
Number of slots	18

Outer stator diameter	230 [mm]
Inner stator diameter	152 [mm]
Air-gap thickness	1.5 [mm]
Magnets thickness	4 [mm]

Table 2-1 - Motor parameters

The adopted mesh used for the FE Analysis is presented in Figure 2-1. The refinement of the mesh in the main air gap is necessary to achieve a reasonable accuracy of the results. A three phase winding configuration has been considered (star connection). Two-dimensional time stepping analysis is considered.

2.1.1 COGGING TORQUE

Cogging torque results from the interaction of the permanent magnets on the rotor with the slots in the stator. Motor design techniques such as fractional pitch arrangements can minimise cogging torque. For this PMSM, many simulations were conducted with the objective of minimizing the cogging torque. In particular, by changing the angular aperture of the magnet is found the corresponding angle minimizes the cogging torque. This value is 14.6 deg. The cogging torque is possible to see in Figure 2-2.

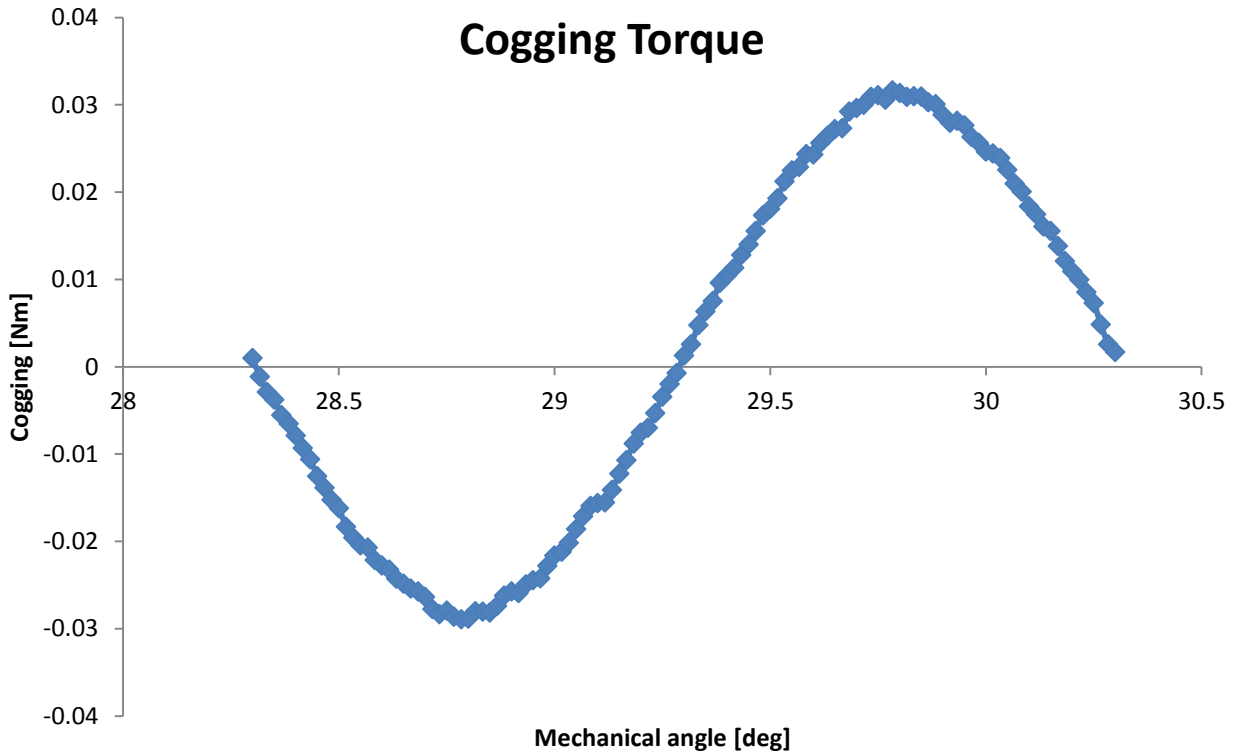


Figure 2-2 - Cogging Torque versus mechanical angle

2.1.2 NO LOAD CONDITION

The no load condition is analysed to evaluate the no load EMF, the relationship of the voltage with respect the speed (k_v) and the cogging torque featured by the machine. The Fourier Series transformations has been applied to the calculated no load EMF waveforms and the fundamental Harmonic has been considered. Linear dependency of the no load voltages with respect the mechanical speed is expected: the coefficient is calculated according to (2-1)

$$k_v = \frac{32.5 V}{805 rpm} = 0.04 \quad (2-1)$$

where 805 rpm is the mechanical speed in root per minute. The harmonic content of the no load EMF result limited at the fundamental and some other harmonic, in particular the 5th and the 7th harmonic whereas no 3rd harmonic is present as expected.

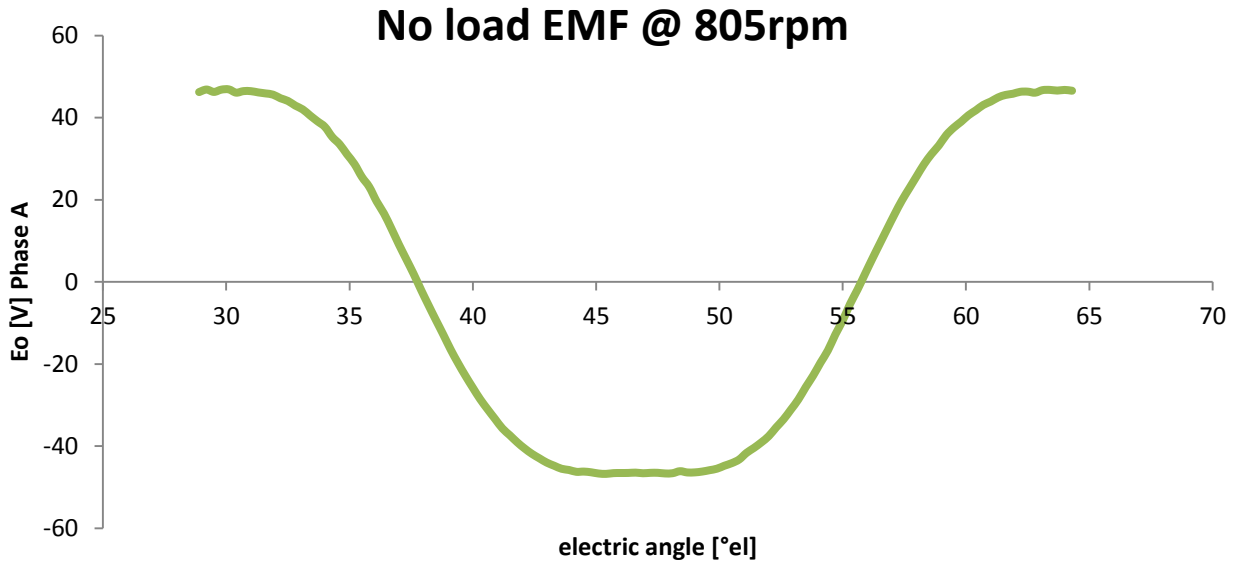


Figure 2-3 - No load EMF @ 805rpm

Figure 2-3 show the back electromotive force (BEMF) for 805rpm. Considering that the no load voltage is calculated according with the Faraday-Lenz Law, the maximum of the no load flux linkage for the phase A can be seen in Figure 2-4.

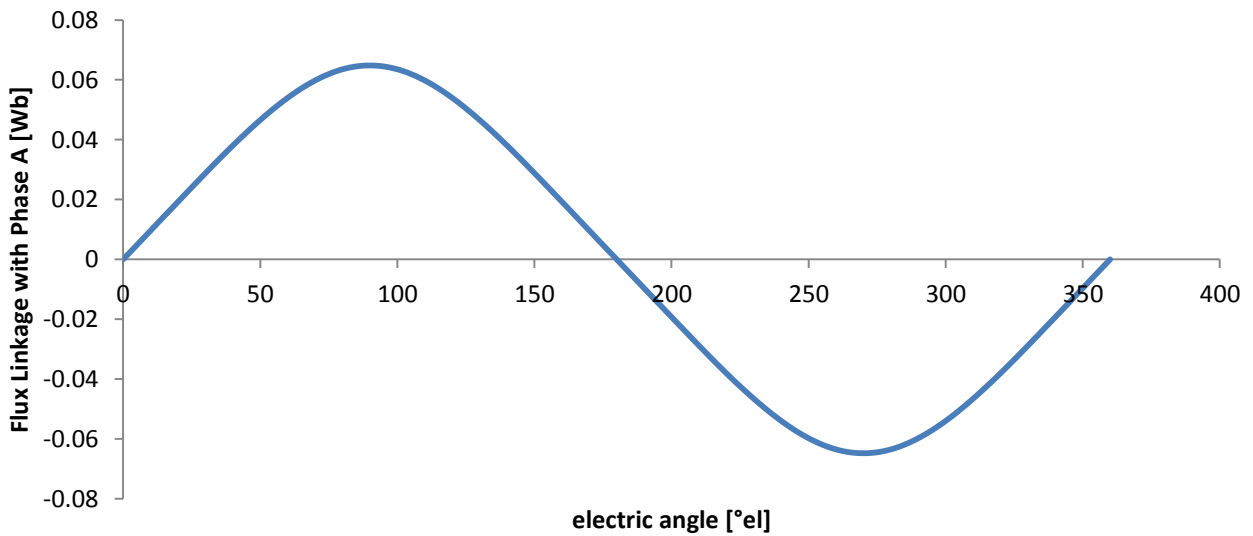


Figure 2-4 - Flux Linkage versus electric angle

2.1.3 LOAD CONDITION

Loaded conditions are investigated with the aim to evaluate ratio of the torque with respect the load current, iron and ohmic stator winding losses. Transient 2D simulation are considered for this analysis.

The magnetic axis related with one of the phases is aligned with the magnetic axes of the rotor magnets to provide only a no load positive d-axis component, coherent with the no load EMF shown in Figure 2-3. A current-fed symmetric 3 phase supply in-phase with the back-EMF is considered (i.e. q-axis current). Maxwell Stress Tensor is the adopted technique to estimate the instantaneous torque featured by the machine; the continuous torque is calculated as the average over an electrical period of the instantaneous result. The output torque is independent of the speed of the machine.

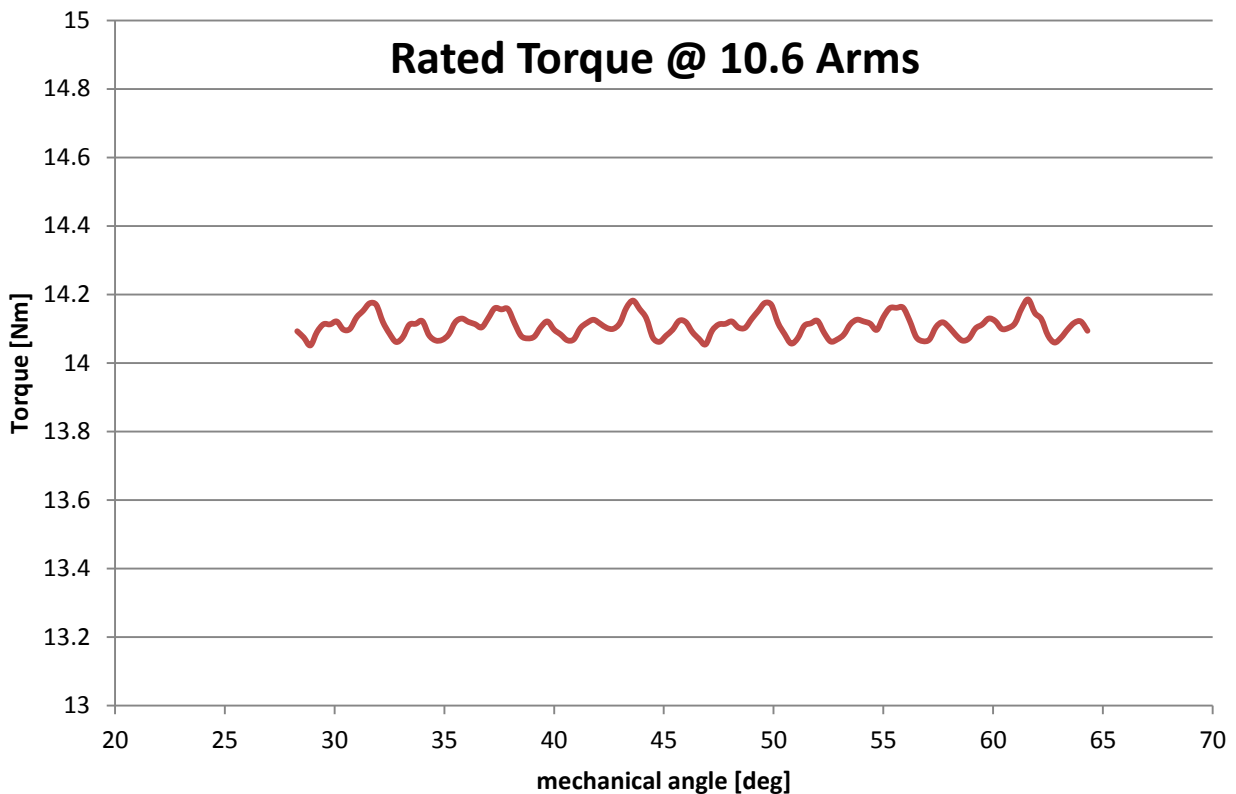


Figure 2-5 - Torque waveforms @ I=10.6Arms

The torque waveform for one condition is evaluated and illustrated in Figure 2-5. It is possible to see a small torque ripple, about 0.2Nm. Figure 2-6 present the flux density distribution obtained with the 2D Model in FEMM.

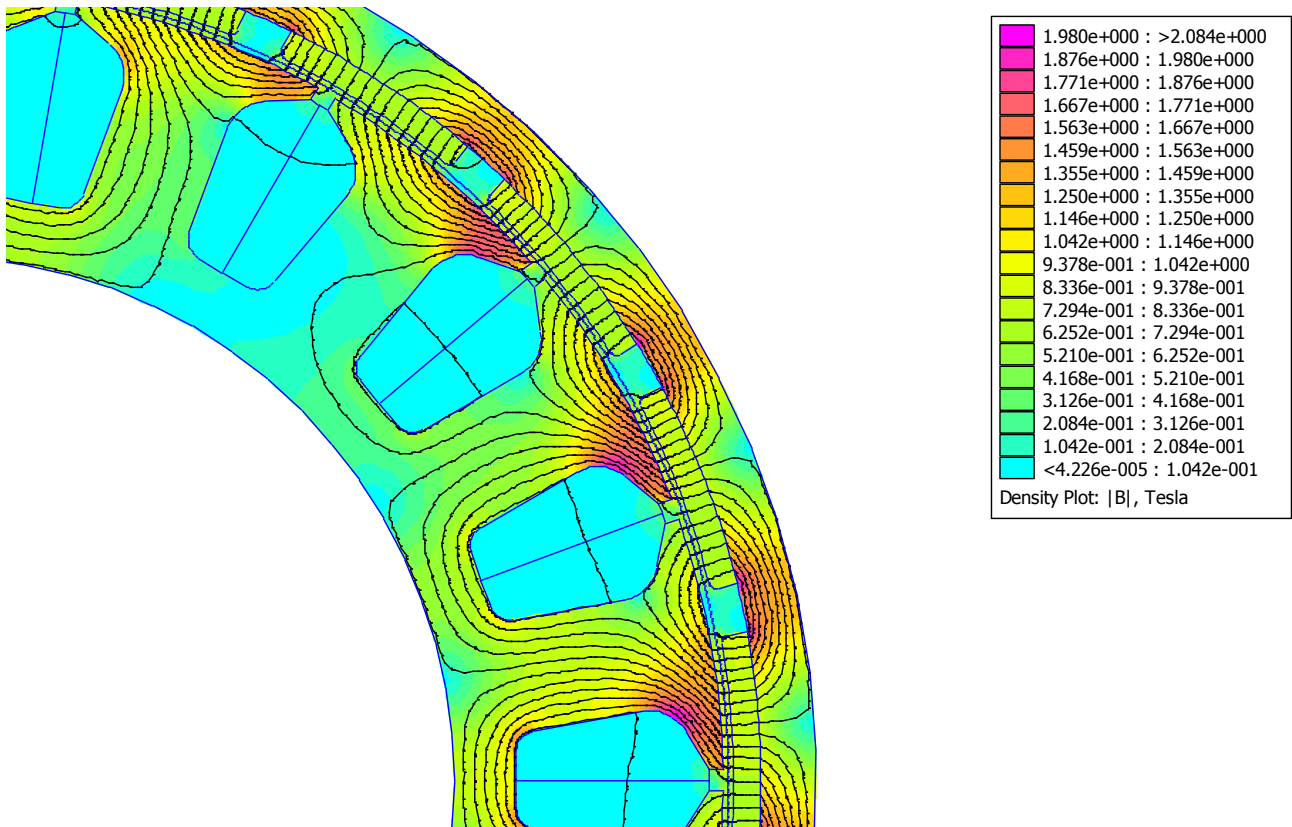
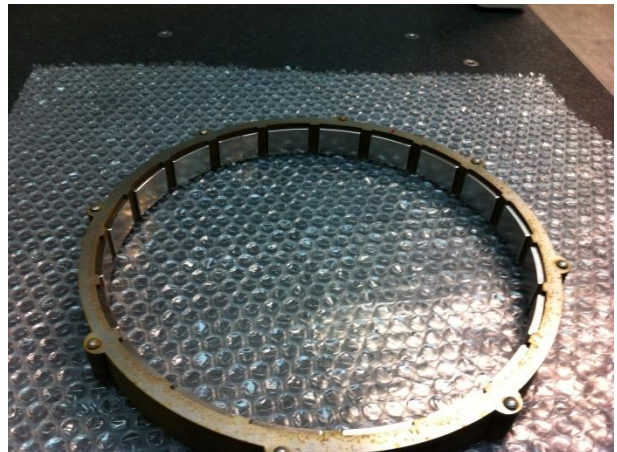


Figure 2-6 - |B| shaded plot for load condition simulation @ I=10.6Arms



a)



b)

Figure 2-7 - Prototype

A prototype machine (Figure 2-7) was built in partnership with TEM Electric Motors.

2.2 EXPERIMENTAL RESULT

A short summary of the experimental tests carried out on the PMSM with external rotor are observable in the following table.

Data	Torque	Speed	Mot. Power	Function	Vdc	Idc	Pdc	VLL	Imot	Rend. motor
	Nm	rpm	W					Vrms	Arms	W
27/05/2013	15.3	704	1128	Motor	104.8	11.6	1218	37.31	11.5	0.972
27/05/2013	24.4	418	1068	Motor	104.7	12.3	1283	25.54	19.9	0.875

Table 2-2 - Experimental Result

We can observe that the efficiency (0.97) of the motor is very high in its rated condition.

From a thermal point of view, according to tests carried out, it can be noted that the motor never exceed the maximum permissible temperature by the windings in the nominal conditions. In fact, the temperature is around 40°C.

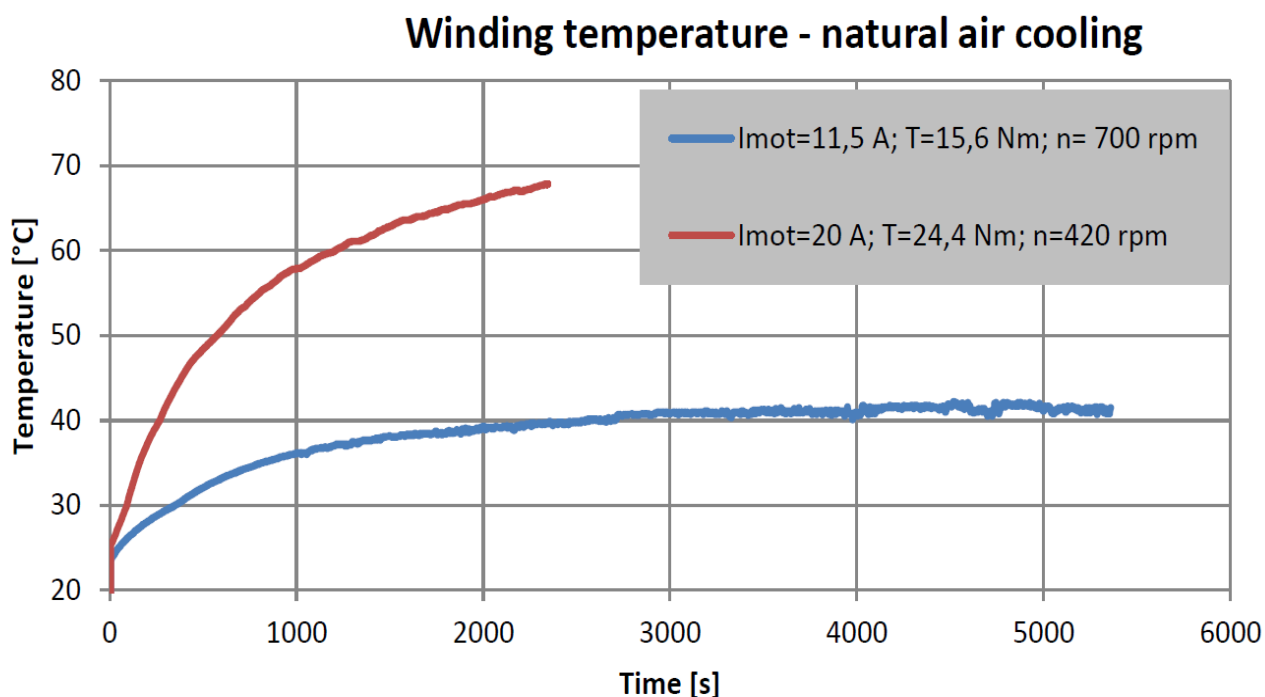


Figure 2-8 - Winding Temperature with natural air cooling

Chapter 3

DEVELOPMENTS ABOUT MORE ELECTRIC

AIRCRAFT

3.1 INTRODUCTION

Since 1960, the air traffic, both passenger and freight, has increased and is expected until 2017, a steady increase in average of 5% and 7% respectively [1]. As a result of this growth affects a highly competitive market for all participants in the sector: from the producer of the smallest components of an aircraft, to travellers who expect continued improvements of features and services offered accompanied by continuous reductions in costs and environmental impact. With regard to the latter aspect, we can say that the carbon dioxide emissions from aviation account for 2% of global emissions. The aircraft engines, in fact, produce carbon dioxide (CO₂), nitrogen oxide (NO_x), hydrocarbons (HC), carbon monoxide (CO), the effects of which include:

- Climate change at high altitude;
- Air quality at low altitude.

Although the technological advances in the field have improved the efficiency of aircraft and reduced transport costs, there are still a lot of pressure on manufacturers to improve the performance of future vehicles in terms of safety and air pollution. In order to meet these expectations, the entire aviation industry is planning to radically re-evaluate the whole system aircraft. It is in fact necessary to revisit the whole architecture of an aircraft, with the introduction of new technologies for the performance of key functions on the aircraft.

Nowadays conventional civil aircraft are characterized by four different secondary power distribution systems: mechanical, hydraulic, pneumatic and electrical systems. This implies a complex power distribution network on board and, given the structure of the means of transport, the need for adequate redundancy of each of them. Since the 80s, the US Air Force and NASA have found a solution for the progressive reduction, or even elimination, of such centralized power systems on board. To improve the reliability of the system, maintenance, operating

costs and the weight of the aircraft have been proposed new electric technologies that have recently made a major change in the design. In this sense, the concept of greatest impact on the architecture of the aircraft is concentrated in the expression **More Electric Aircraft** (MEA), which indicates the growing adoption of electric systems to replace conventional hydraulic, pneumatic and mechanical systems. As a result, the electrical system of the aircraft will be radically changed, so that's next to the MEA concept, has strengthened the concept **More Electric Engines** (MEE), where the electrical machines are integrated into the main turbine to generate electricity, start the engine and ensure safety in the event of failure during the flight.

In recent years, many projects have been developed to explore the concepts MEA / MEE for both military and civil applications, trying to achieve what will be the concept of the **All Electrical Aircraft** (EEA).

In 2000, he launched the project **Magnetostrictive Equipment and Systems for More Electric Aircraft** (MESA), which aims to reduce power consumption and weight of onboard systems through the development of magnetostrictive actuators and motors.

In 2002 it was the turn of the **Power Optimized Aircraft** (POA) aimed at finding alternative equipment to reduce weight, fuel consumption and maintenance costs of the aircraft.

In 2004, the project **Magnetoelastic Energy Systems for Even More Electric Aircraft** (MESEMA) has been dedicated to the development, production and testing of innovative transducer systems based on active materials aiming for a drive with high torque density, reduced vibration and noise generation of electricity and structural integrity monitoring.

In 2006, the project **More Open Electrical Technologies** (MOET), aimed to establish a new industry standard for the design of commercial aircraft, in conjunction with the reduction of emissions and improvement of operational capacity, as an evolution of the concept of "fly-by-wire" to that of "power-by-wire".

All of these projects, which are now the ultimate expression of MEA concept, have contributed to the development of many electrical devices that are currently in use on modern vehicles. For example, the electrification of the actuators of the flight surfaces, Airbus A380 leads to less consumption, while reducing costs, or the electrification of the cabin pressurization and air conditioning, adopted by the Boeing 787, saves energy of 3-7%.

The most important technology that allows to use the MEA concept, without a doubt, is the power electronics associated with electrical machines and electric actuators. However, aeronautical applications have some demanding conditions and there are still a number of areas of use in which they must be made of the

improvements in terms of weight, cost and reliability of the systems.

3.2 MORE ELECTRIC AIRCRAFT (MEA)

For a typical medium-sized aircraft, the only sources from which to draw power, the engines are gas turbines, as shown in Figure 3-1. These turbines, as well as providing mainly the reliability necessary for flight, they also provide food for all other loads on the plane.

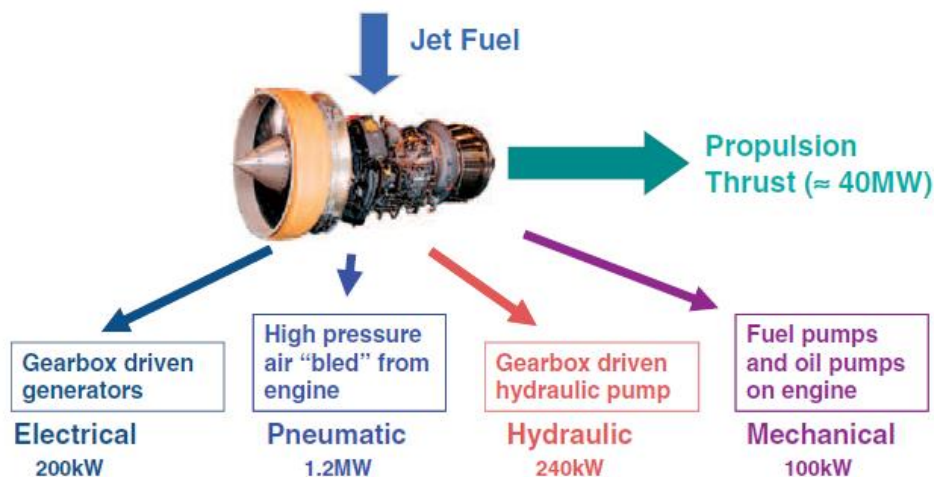


Figure 3-1 - Energy distribution in a conventional aircraft

In a conventional civil aircraft there are four types of renewable energy derived from motor: electric, pneumatic, hydraulic and mechanical.

The electrical system is used for power loads and for avionics systems, lighting equipment and in-flight entertainment.

The pneumatic system, powered by the extraction of air from the engine, shall govern the environmental control system (pressurization and air conditioning) and wing protection against the ice.

That mechanical, operated by a system of transmissions by the engine, is used for pumping fuel and oil.

Finally, the hydraulic system is used for all the actuation systems of the aircraft.

The assumption on which the MEA concept is based on, is that only one single power source is available from the main motor. For this purpose, the choice falls on a single electrical system, as it has a series of advantages in terms of flexibility and range of applications. A possible system designed for the MEA is shown in Fig. 1.2, where all loads are powered by the on-board electrical system.

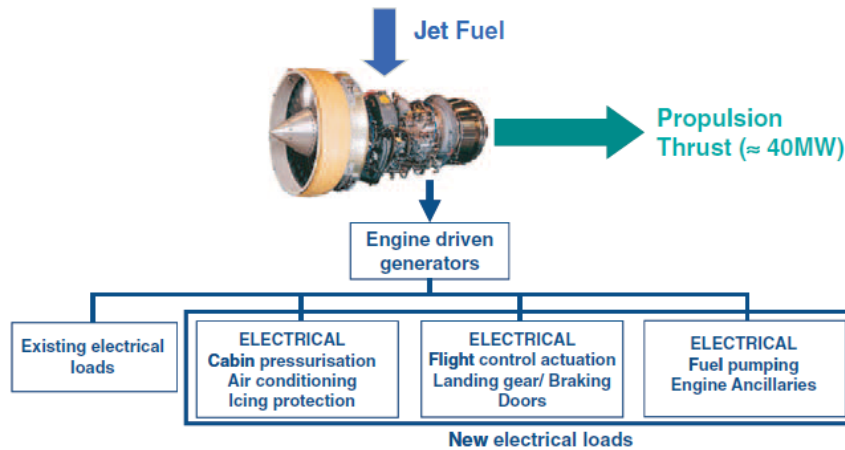


Figure 3-2 - Energy distribution in MEA concept

As already mentioned above, the general objective of this radical change in technology is to reduce operating costs, fuel consumption and environmental impact of air transport. The removal of the pneumatic system, for example, carries away with it the air bleeding system on the gas turbine greatly improving its efficiency. Once the entire technology has been realized, the removal of mechanical and hydraulic systems may also lead to some reduction of weight at the system level. More importantly, is that electrical systems offer many more management options such as advanced diagnostics and maintenance options. The Figure 3-3 compare a conventional system of an aircraft with an equivalent MEA; you can see the elimination of certain equipment and the simplification of the connections between engine and fuselage.

A study conducted by NASA has shown that the use of these technologies could result, for a typical aircraft seating 200, a reduction of 10% by weight and a reduction of 9% of the fuel.

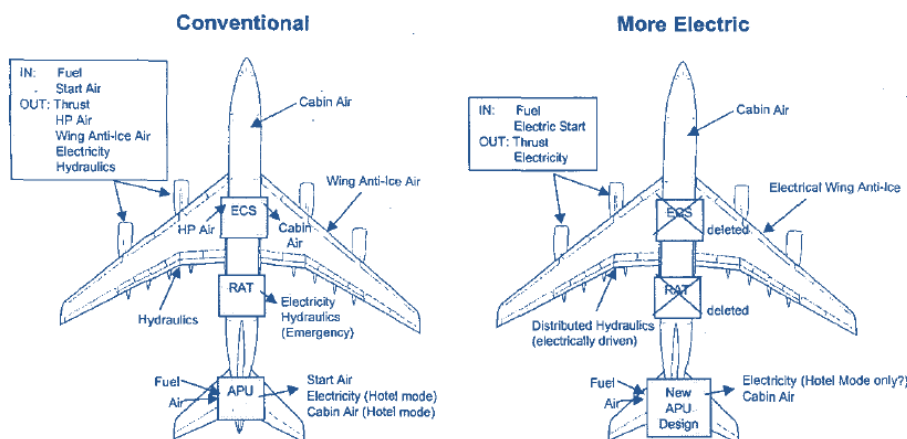


Figure 3-3 - Comparison between conventional and More Electric Aircraft

In order to optimize the whole aircraft, the architecture of the electrical system should be chosen with care.

Currently, the most civil aircraft utilize a combination of:

- a system of high power, three-phase, 115 V, 400 Hz dedicated to great loads;
- a system of low-power, 28 VDC for avionics and control services batteries.

The larger loads are then fed from the systems AC or DC high voltage.

Unmanned aerial vehicles (UAVs) tend to use a lower voltage as the power levels are generally lower and the efficiency becomes an important factor in the design.

The MEA provides a much greater load on the electrical system. For comparison, the typical power existing in aircraft, such as a Boeing 737, lies in the range of 100 kW and 787 for the figure rises to more than 1 MW.

The following table, according to the requirements MEA, shows some typical value of power to some of the larger loads on civil aircraft:

Table 3-1 - typical values of power required by the MEA

Application	Comments	Typical power level
Air conditioning	Environmental control system	4 x 70 [kW]
Flight controls	Primary and secondary - often short duration at high loads	2-35 [kW]
Fuel pumps		10 [kW]
Wing ice protection	Thermal mats or similar	250 [kW]
Landing gear	Retraction, steering and braking - short duration of operation	5-70 [kW]
Engine Starting	May be used for additional applications - short duration	200 [kW]

The first MEA, such as the Boeing 787, uses a combination of electrical systems, as shown in Figure 3-4.

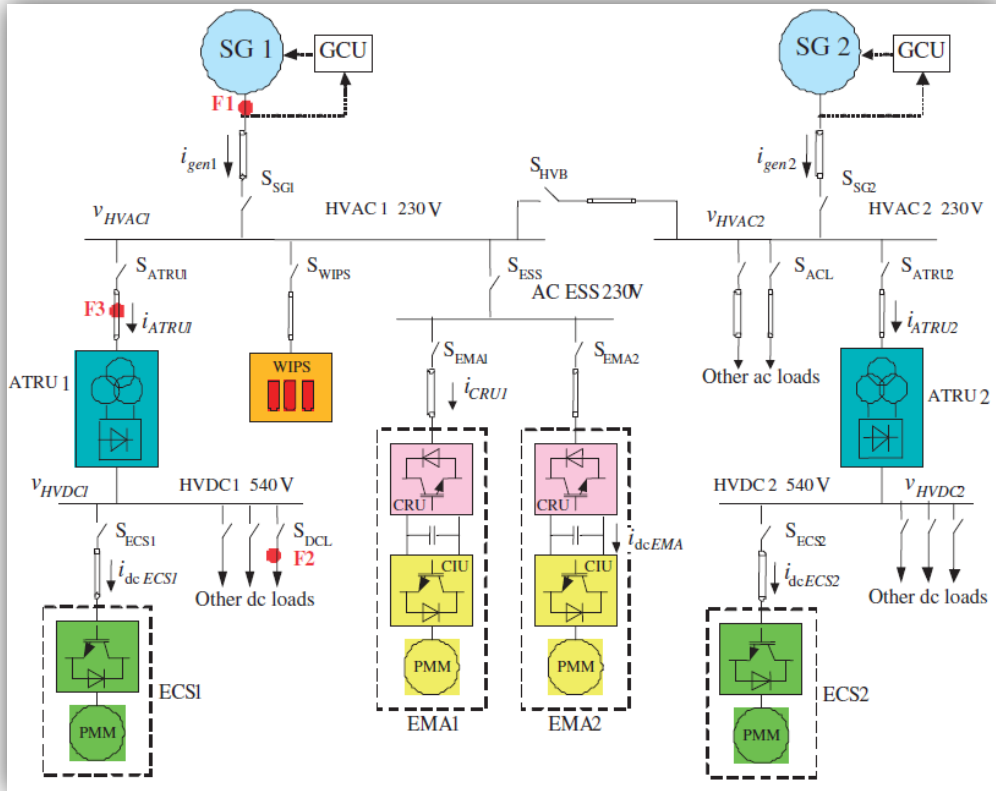


Figure 3-4 - Electrical System on Boeing 787

The industry is considering the AC systems and variable frequency in order to replace the Integrated Drive Generators (IDGs) on current engines, which require complex hydraulic systems for generating alternating voltage with a constant frequency from a variable speed shaft engine, with generators simpler and lighter.

Since the removal of IDG is mandatory, the trend in the industry seems to be directed towards a generation system with variable frequency AC with a DC connection of high voltage distribution. The strategy variable frequency (sometimes called a "frequency wild") does not require the IDG and consequently it is possible to a higher power density.

Considering that the generators are driven by shafts with different rotation speeds, it is reasonable to convert all the power generated in a single output of high voltage on the distribution system. This system allows to reduce the weight of the cables as paths to lower current; in the DC systems, in fact, there is no reactive power flow and there is the skin effect due to high frequency. In addition to the high voltage DC systems, the systems will remain low voltage to power the apparatus dedicated to the avionics. The Fig.1.5 shows a conceptual layout of the electrical system on MEE four engines and two auxiliary power unit (APU).

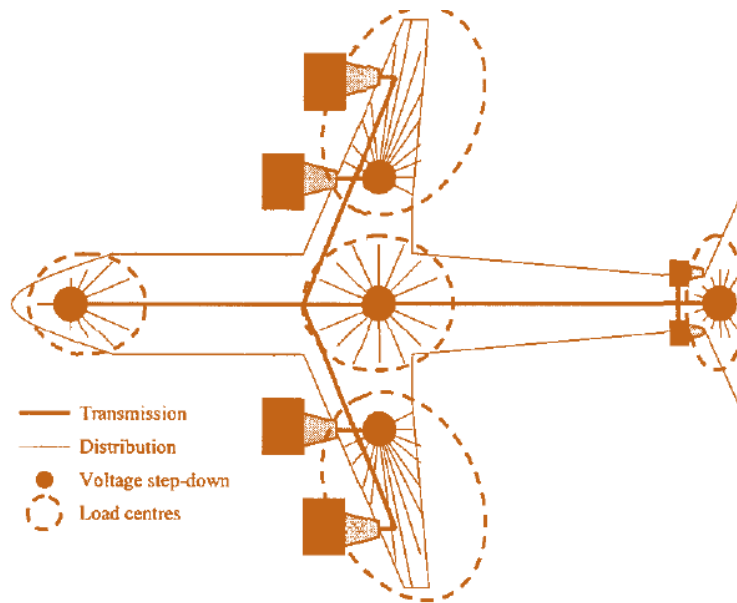


Figure 3-5 - Layout of the electrical system with MEA concept

The use of a transmission system require a high voltage DC step-down voltage between the transmission system and the loads. The step-down converter between the distribution system in the high voltage DC and the loads can be carried out in a centralized way for each load center.

The reason for choosing such a system can be summarized as follows:

- In order to reduce the weight, the electric power must be transmitted at high voltage (with consequent decrease of the current);
- Higher voltages also reduces the power losses during transmission, because, to a cable, the losses are proportional to the square of the current;
- Using the same voltages for generation and transmission would eliminate some type of converters;
- Alternating current systems require cables larger than the DC systems, because of the reactive power flows and the skin effect at high frequency;
- Historically, the AC systems were preferred because the voltage variations could be made by means of transformers. Today, the power electronics may be used to cope with variations in voltage regardless of the frequency.

3.3 POWER GENERATOR

The transition to the MEA technology significantly increases the amount of the electrical power used by an aircraft, typically

between 100-200 kW to over 1 MW for a large civil aircraft; this increases the demand on the generating system. In order that the MEA can be competitive in terms of weight and reliability of the system, there has been a number of fundamental developments in the generation of electricity on board. Below we will see some examples of the generation of electricity.

3.3.1 GENERATING POWER AT CONSTANT FREQUENCY

Many of the civil aircraft using a transmission system in order to give the shaft a constant speed from a variable speed of the gas turbine. This shaft at a constant speed drives the electric generator to give a constant frequency, 400Hz (Figure 3-6). The voltage of the generator is controlled using a control loop with an exciter. The mechanical transmission used in this system can be expensive to purchase and maintain because of its complexity. An alternative technique for generating a constant supply frequency is to connect the generator directly to the motor, as shown in Figure 3-7. The output of the generator will then have a variable frequency depending on the speed of the turbine engine. This frequency, which will change during the flight the airplane subsequently to the requests of the pilot, can be processed by a power converter (usually cyclo-converter and matrix converter) and filtered to produce a fixed frequency and supply voltage. The disadvantage of this system is that this power converter must process all the power generated and, therefore, must be reliable in order to obtain the level of security required by the aircraft. Unfortunately, the power electronics is not yet reliable enough to make this viable and remains a rare choice of configuration.

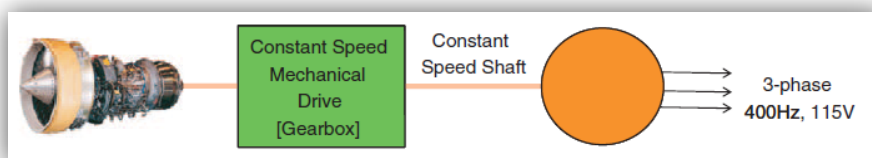


Figure 3-6 - Electrical power generation at constant frequency with Mechanical Drive

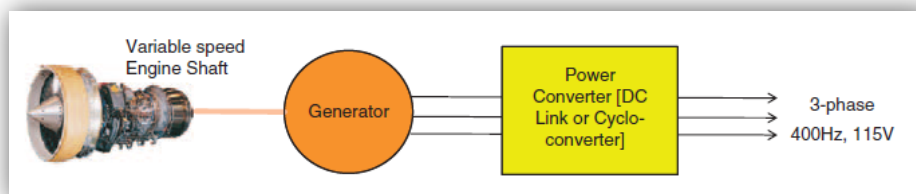


Figure 3-7 - Electrical power generation at constant frequency with power electronics

3.3.2 GENERATING POWER AT VARIABLE FREQUENCY

If we decide the need to have a fixed frequency electrical power, it is possible to directly connect a generator to the motor, as shown in Figure 3-8. The output of this generator provides a power supply with a voltage-controlled variable frequency, typically in the range 320-800 Hz. In this type of system, there is a direct connection between the generator and the power bus, creating a build configuration simple and reliable. The disadvantage of this system is that almost all loads require power converters for the control, since the variable frequency power supply cannot be applied directly to most applications.

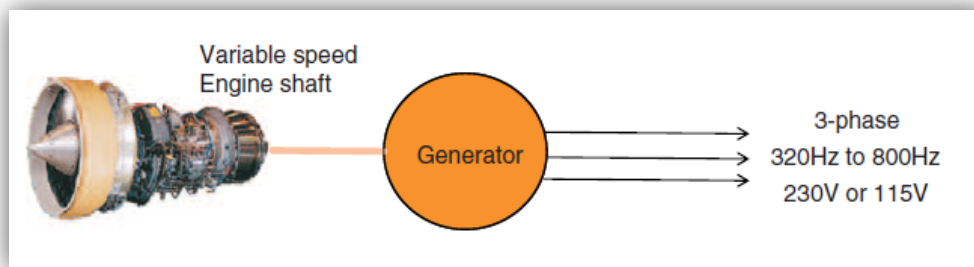


Figure 3-8 - Power Generating at variable frequency

3.4 MORE ELECTRIC ENGINE (MEE)

The technology behind the MEE concept can be described in the following way:

- Using a motor / generator lightweight high power, high efficiency, connected to each of the main shafts of an engine, to provide electric energy to the system and remove the hydraulic pump from the engine, thus simplifying the interface engine / cabin.

It can be mounted outside of the turbine and connected to the main shaft through reduction gears (option '**external**'), or mounted directly to the inside coaxially to the shaft (option '**internal**'). There are several studies, dedicated to the integration of electric motor/generators directly into the main gas turbine, acts to reduce the overall complexity of the system, the fault tolerance and with the objective of increasing the overall efficiency of the system.

In this way, the transmission system at a constant speed (CVG), or Integrated Drive Generators (IDG), may be partly or totally eliminated. Consequently the frequency generated covers a wide range depending on the change of engine speed.

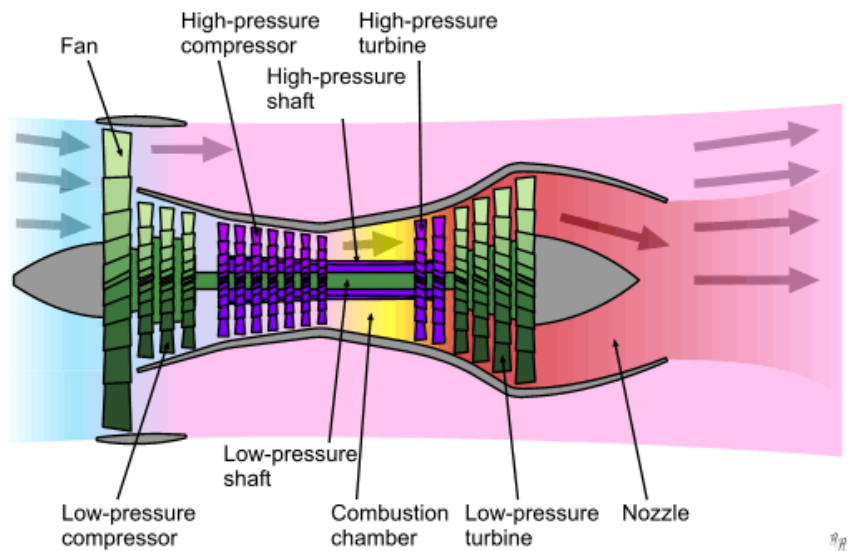


Figure 3-9 - A Turbofan system

With reference to the structure of a turbofan engine (Figure 3-9) it is possible to integrate the generator inside the main motor in different positions. In particular, the generator can be operated both by the **low pressure** (LP) and **high pressure** (HP). These two possibilities involve different advantages and disadvantages, mainly regarding the size, speed and environmental conditions of work.

In integration HP shaft, the electric machine is characterized by a lower weight, occupies a smaller room, and has a higher speed of rotation of the shaft. Furthermore, this solution allows to use the electric machine as a starter motor, avoiding in this way the auxiliary system dedicated. However, because of the high inertia of the turbine, is also required a high torque to the engine when it is stationary.

The main disadvantage of integration onto HP is the tough environmental conditions of exercise, due to the high temperature.

Using active magnetic bearings, which would replace the current sphere system. These offer the possibility to remove the oil from the engine system, which would lead to a drastic reduction of a scheduled maintenance, a better control of engine vibrations, since the trees would rotate around their centres of mass rather than their geometrical centres, and a best engine diagnostics, since the variations of signals in the feedback from the bearings are used to control the movement dynamic shaft.

Using compressors and units of cooling/heating electrically operated to pressurize and condition the air in the aircraft cabin. These units may be powered by motors; the need to provide air conditioning in the cabin in every situation (for example when the main propulsion engines are stopped) would lead to prepare one or more auxiliary power units (APU). The result is an improvement

of the environment in the cabin for the crew and passengers as well as to a reduction of the emission of fuel.

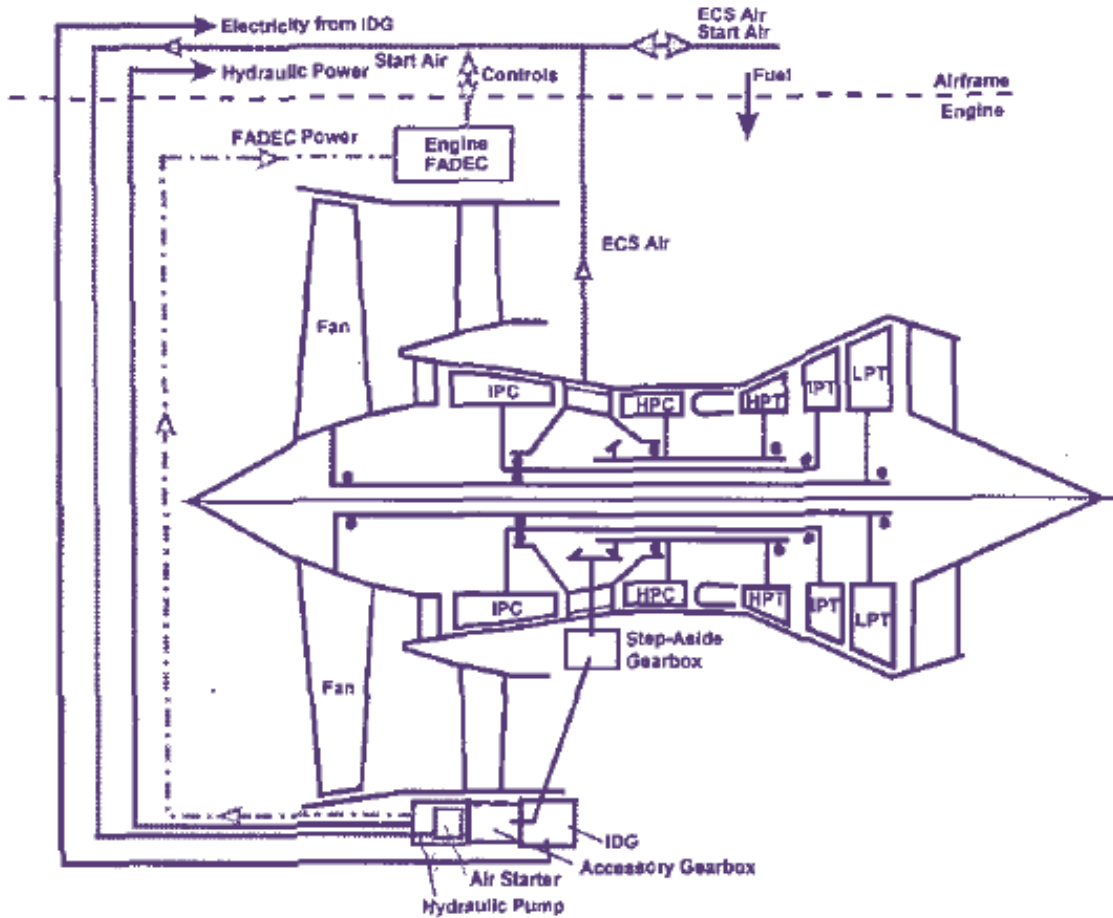


Figure 3-10 - Conventional engine

Figure 3-10 and Figure 3-11 comparing two types of engines; the first is a conventional engine, while the second is a MEE. You can see how changing the connection between the engine and the cabin. The interface between the engine and the aircraft is considerably simplified, having been reduced to only control signals of electricity and fuel. The result would be an aircraft lighter and less expensive.

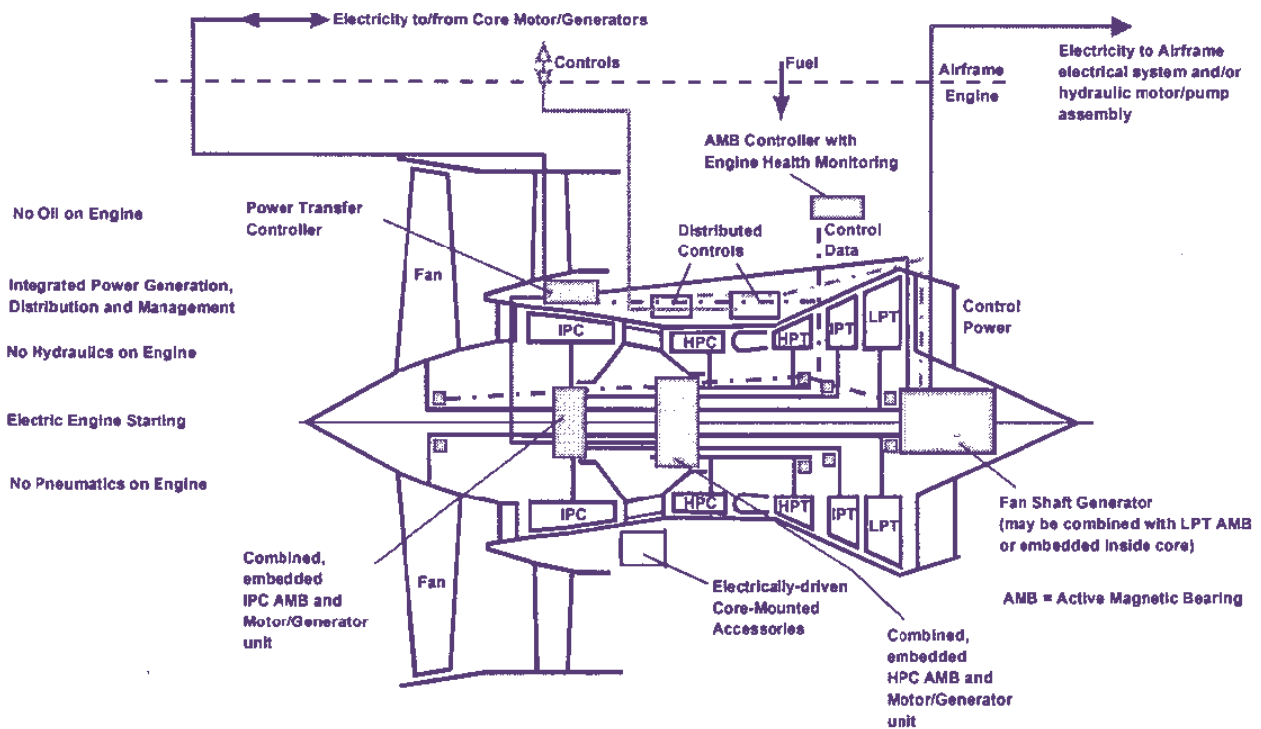


Figure 3-11 - Engine with More Electric Engine Structure

3.5 SYSTEM SECURITY

It is of fundamental importance to the reliability of some electrical drives in applications MEA and in particular for the three main units:

1. electromechanical actuators for primary control of the flight surfaces;
2. electric fuel pump;
3. motor/generator integrated into the engine.

3.5.1 DRIVE FOR FLIGHT CONTROL APPLICATION

Modern aircrafts are used hydraulic actuators to move the surfaces to control the flight. There are three basic degrees of control of the aircraft for the flight (see Figure 3-12): roll, pitch and yaw. The critical surfaces for the control of the flight are respectively the ailerons, elevator and rudder which are then referred to as the primary actuators. Other control surfaces such as slats and flaps, are not critical to flight and, therefore, referred to as secondary actuators. Examples of these surfaces are shown in Figure 3-13. The number and type of actuators is very different compared to the aircraft considered. Furthermore, the load requirements are very different: starting from a few kilowatts to the lamellas of the edge, up to 50-60 kW for the stabilizer systems and vertical rudder. In addition, the dynamic load profile may be very different: there are few surface movements that have great size and short duration (typically during landing and take-off) or "small" superficial adjustment during flight. In addition, abnormal performance can be requested to the actuators in flight during some critical conditions. For example, if all the engines on the same wing fail, the actuator of the rudder must be able to keep the drawbar in a fixed position, with a high yaw angle, during the flight. In this situation, it is very high the torque required to the electric motor.

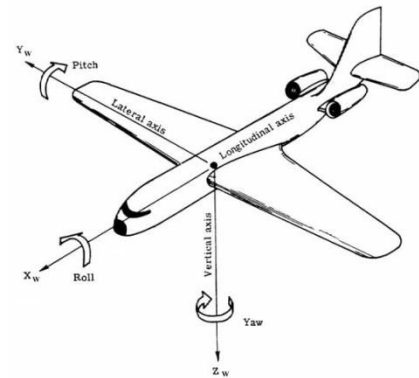


Figure 3-12 - Roll, pitch and yaw are used to describe the objects orientation around each of its axis

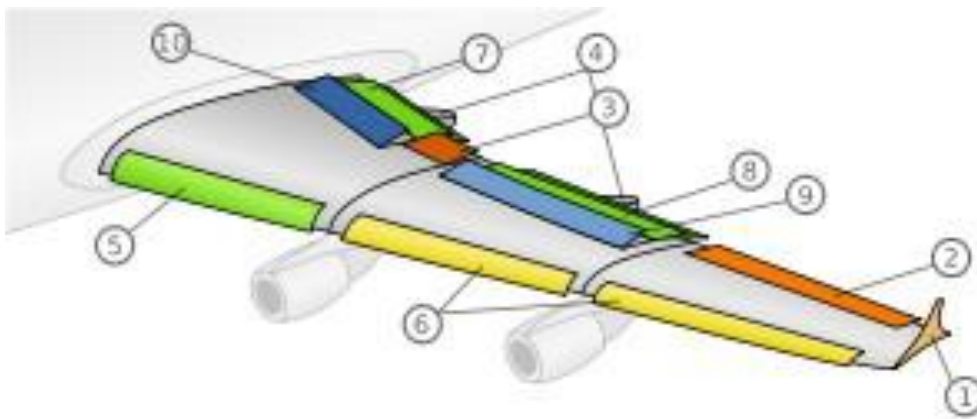


Figure 3-13 - Wing control surfaces of a fixed-wing aircraft: 1. wingtip, 2. Low speed aileron, 3. high speed aileron, 4. flap track fairing, 5. Krüger flaps, 6. slats, 7. three slotted inner flaps, 8. three slotted outer flaps, 9. spoilers, 10. spoiler air-brakes

It is important to emphasize that the actuators have to work in very harsh environmental conditions: temperature between -60°C and $+70^{\circ}\text{C}$ and atmospheric pressure variable between 0 and 1 bar. Due to the low thermal conductivity of the fuselage (composite materials, sheet materials, etc.), the thermal exchanges between the actuators and the environment must be carefully evaluated.

In a conventional fuselage, the drive system of the flight surfaces is made by a centralized hydraulic system, consisting of a hydraulic pump and a motor positioned in the fuselage as well as to different pipelines of fluids and hydraulic actuators positioned in the wings and in the tail. The control of hydraulic actuators is realized with the consolidated technology of "fly-by-wire" where there is no mechanical connection between the control surfaces and the cockpit. Moving towards a scenario all electric aircraft (AEA), the idea is to control each area with its own electromechanical actuator directly coupled. This concept is defined as "power-by-wire".

3.5.2 ELECTROMECHANICAL ACTUATORS (EMA)

When replacing hydraulic actuators with electric system, the obvious choice is to use an electromechanical actuator (EMA), as shown in Figure 3-14. In a system EMA, the surface is moved by rotating a motor. At the same time, moves a system of ball screw through a gear reducer. For each revolution of the motor moves the actuator to a fixed quantity as there is a direct connection between the motor and the arm. The problem in the distribution of EMA MEA is that it is very difficult to ensure that the ball screw can never problem. For this reason, aircraft manufacturers still have some doubts in using the EMA preferring the more reliable electro-hydraulic actuators (EHA).

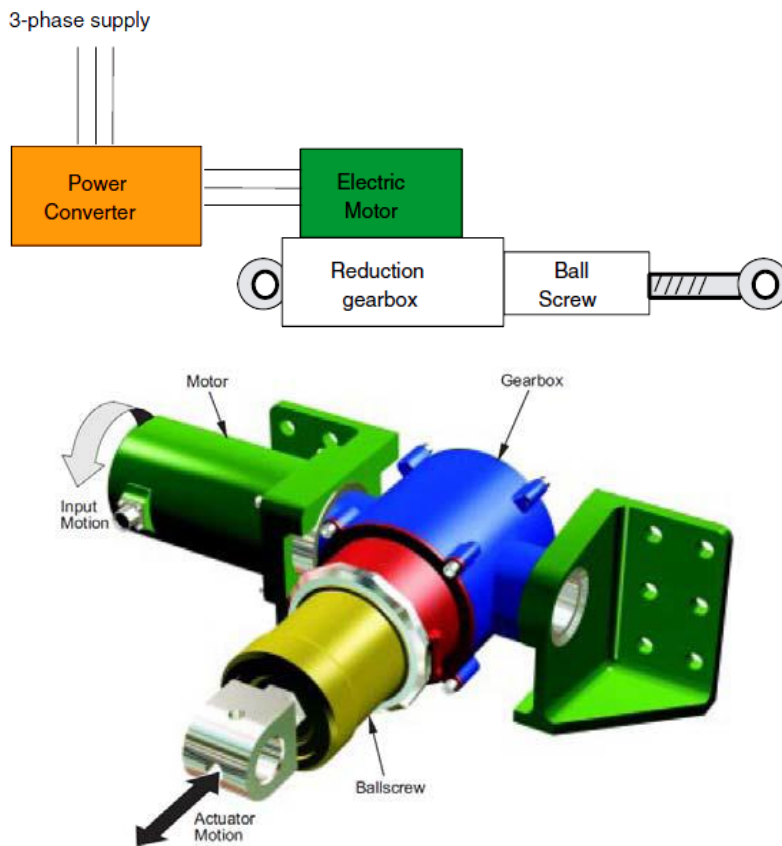


Figure 3-14 - Electromechanical actuator

3.5.3 ELECTRIC-HYDRAULIC ACTUATOR (EHA)

An electro-hydrostatic actuator (EHA), reported in Figure 3-15, is driven by a local system and controlled with a hydraulic pump driven by a positioning motor. The position of the actuator moves a fixed increment for each motor revolution. There is no a direct connection between the motor and the mechanical arm and therefore the EHA has failure modes lighter, giving an advantage over the EMA for the control of primary applications. Another advantage is that the actuator can be controlled like a conventional hydraulic system, resulting in the traditional operations active/standby or active/active.

There is also the possibility of an Integrated Actuator Package (IAP TM). This device is an EHA that, thanks to an advanced dual hydraulic circuit, allows to use a constant speed, unidirectional electric motor [2]. When some, but not all, of the traditional hydraulic circuits are removed and substituted by EMAs and/or EHAs, it is common to speak of "more electric aircraft" (MEA). The first application of EHAs to primary flight surfaces was in the delta-wing Vulcan bomber in the 1950s [3]. Its redundant design, achieved using the EHAs, allowed to get an impressive safety

record. More recent example of commercial MEAs are the Boeing 787 and the Airbus A380.

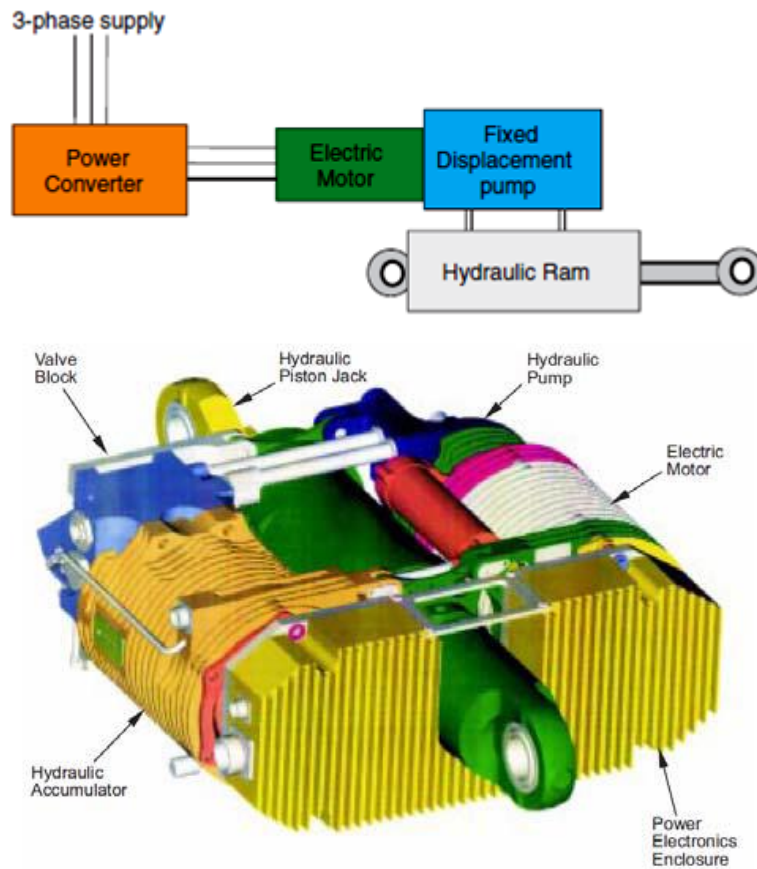


**Figure 3-15 - Example of large Electric-Hydraulic Actuator (EHA).
Source [2]**

In the Boeing 787, a mid-sized wide-body aircraft, spoilers and horizontal stabilizer flight controls are operated by electric motors in order to guarantee the control functionality also in the case of a total hydraulics failure. The super-jumbo A380 represent the state-of-art with respect to the flight control system.

Both EHAs and EMAs use an electric motor and a power converter and a control system. [4]. With respect to the electric motor, a Brushless DC (BLDC) and the switched Reluctance (SR) motors are the more promising ones due to their lightweight, reliability characteristics. It is commonly reported that a fault-tolerant electric motor for EMA applications has to be guarantee

- High torque/weight ratio;
- High torque/ampere ratio;
- High efficiency in the full speed range;
- Electrical, thermal, magnetic and mechanical insulation between the phases;
- Safe operation in faulty conditions (one phase loss).

Also the power converter topology is discussed and analysed in literature. The proposed solutions regards the conventional Voltage Source Inverters (VSIs) and a matrix converters. The converter topology influence several aspects, such as the request DC-Link capacitor in the VSIs (with weight problems [5] and power quality management [6]) and the power quality issues for the matrix converters [7].

3.6 ELECTRIC FUEL PUMP

The fuel pumps can be subdivided in two categories:

- The low pressure boost/transfer pump;
- The high pressure FCU (Fuel Control Unit) fuel pump.

The low pressure pump normally is electrically operated, while, in traditional systems, the high pressure fuel pump is directly driven through the mechanical gearbox and the fuel flux is controlled by means of the fuel valve. As a consequence, the focus is on the high pressure fuel pump because it is another aircraft apparatus that could be electrically driven, introducing the concept of "smart electric fuel pump". The main advantage of the electric solution for the fuel pump is in the possibility to drive the pump at variable speed. In this way the pump can deliver a variable fuel flux to the combustion chamber, in accordance to the engine control requirements, eliminating the fuel valve in the fuel metering system. The application of this new technology leads to several advantages, such as weight saving, lower maintenance costs and improved in-service reliability.

3.7 ON BOARD POWER GENERATION

On conventional civil aircraft, the electrical power is usually generated by wound field synchronous generator with a permanent magnet exciter stage. A generator control unit (GCU) performs a field control in order to regulate the terminal voltage. The generator is mechanically driven by the main engine shaft by of a Constant Velocity Gearbox (CVG). In this way the CVG allowing to maintain constant the frequency at 400Hz. If the CVG is integrate inside the generator, it is called Integrated Drive Generator (IDG).

In addition at the previous described energy generation system, Auxiliary Power Units (APU) are presents on the aircraft. They are small fuel burner jet engines connected to dedicated electrical generators, aimed to supply vital loads in case of main engines or generators failure. The APU also employed to provide electric

power in the pre-flight conditions, when the main aircraft engine are still turned-off.

As back-up energy generation system, in addition at the APUs, there are also the Ram Air Turbine (RATs) which are propellers spanned by the high speed of the air flows near the airframe body (Figure 3-16). They are extracted by airplane body only in emergency conditions.



Figure 3-16 - An example of Ram Air Turbine (RAT) in on F-104S Starfighter (Source: Wikipedia Commons) [8]

3.8 REGENERATION ENERGY ONTO THE ELECTRICAL POWER BUS

An interesting system power could affect the ability to recover energy from the electric actuators. This is possible when the energy from the load circuit to the DC bus. Obviously, the amount of energy depends on the profile of load and the duty cycle of the actuator. Today this energy is dissipated on banks of resistors connected on the intermediate stage of the converter, with inevitable problems of weight and heat dissipation. Regeneration may occur in an actuator when the surface is moved with an aiding load or from the inertial energy when a motor is decelerated rapidly.

A number of options have been identified that could allow the power quality (voltage regulation) to be maintained whilst allowing loads to regenerate power when required [9]:

1. *Centralized energy storage* - allow regeneration onto the aircraft bus and have energy storage on the power bus for when other loads are not present.
2. *Centralized energy dissipation* - allow regeneration onto the aircraft bus and have energy dissipation on the power bus for when other loads are not present.
3. *Local voltage control* - allow regeneration onto the aircraft bus, but only if the voltage at the point of common coupling is within defined limits.
4. *Return energy to source* - allow regeneration onto the aircraft bus and use the generator as a motor if required, the regenerative power would be returned to the engine inertia.
5. *Separate bus for regenerative energy* - do not allow regeneration onto the main aircraft bus, but add an additional, relatively unregulated bus to distribute regenerated power.
6. *Local energy dissipation* - do not allow regeneration onto the aircraft bus and ensure that each item of equipment has energy dissipation if required.
7. *Local energy storage* - do not allow regeneration onto the aircraft bus and have energy storage within each piece of equipment.

3.8.1 LOCAL ENERGY DISSIPATION

The solution used today, shown in Figure 3-17, is not to allow any of electrical loads to regenerate energy onto the bus. If the load has regenerative operations, this energy must be dissipated within the power converters. This is usually achieved using a braking resistor and chopper circuit. Whilst this system works well, the resistor and associated cooling must be sized to cope with the worst case operating condition. For this reason, the dissipative elements add significant volume and weight to the power converter. The advantages of this approach are that the generator and bus will never see regeneration and, therefore, the risk of uncontrolled voltage rise on the bus due to the loads is eliminated.

3.8.2 CENTRALIZED ENERGY STORAGE

It is possible to arrange for each power bus to have an energy storage facility in order to store the regenerated energy for use later, as shown in Figure 3-18. This energy storage would have to be controlled centrally in conjunction with the control of the generator in order to maintain good control of the bus voltage. This energy storage could be provided in the form of rechargeable batteries or regenerative fuel cells. This energy can then be used later in the flight to power the loads when they are in a motoring operating condition.

It is not clear whether or not the extra infrastructure and control required for this solution would be justified in terms of the savings in weight and volume of equipment which could be achieved by allowing regeneration. However, there may be additional benefits for the operation of the aircraft of having this source of energy storage on the bus.

3.8.3 RETURN ENERGY TO THE SOURCE

A more radical, but logical, solution to the problem could be to allow regeneration onto the aircraft bus and then to make it the responsibility of the generator to control the bus voltage, even under regeneration, as shown in Figure 3-19. Many generators can also be used as motors, so it will be possible for the generator to return the regenerative energy to the engine inertia. It should be noted that for a civil aircraft operating under very extreme conditions, it has been shown using real flight data on a rough landing that the maximum regenerated energy from an Aileron EMA is just 40 J. This is not a significant amount of energy in terms of the capacity of the electrical power system.

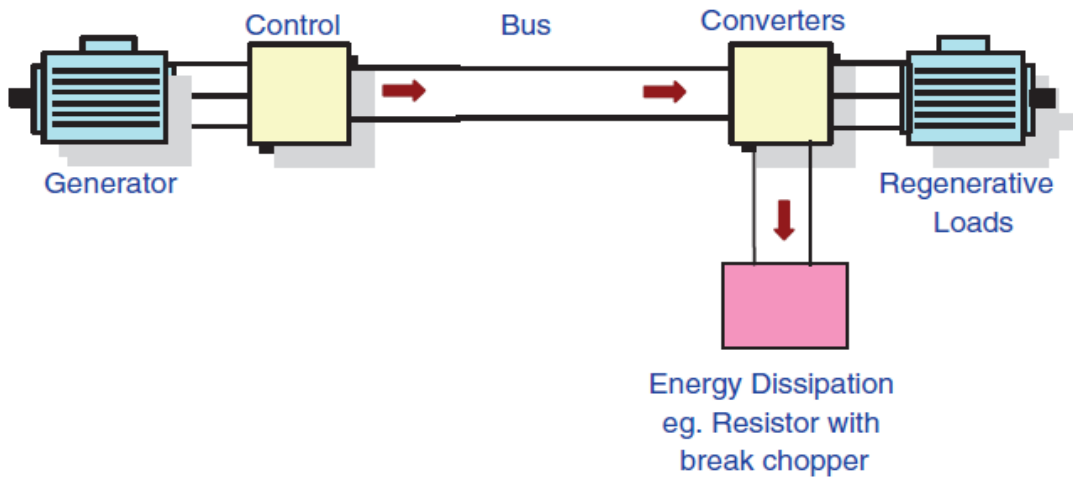


Figure 3-17 – Local energy dissipation

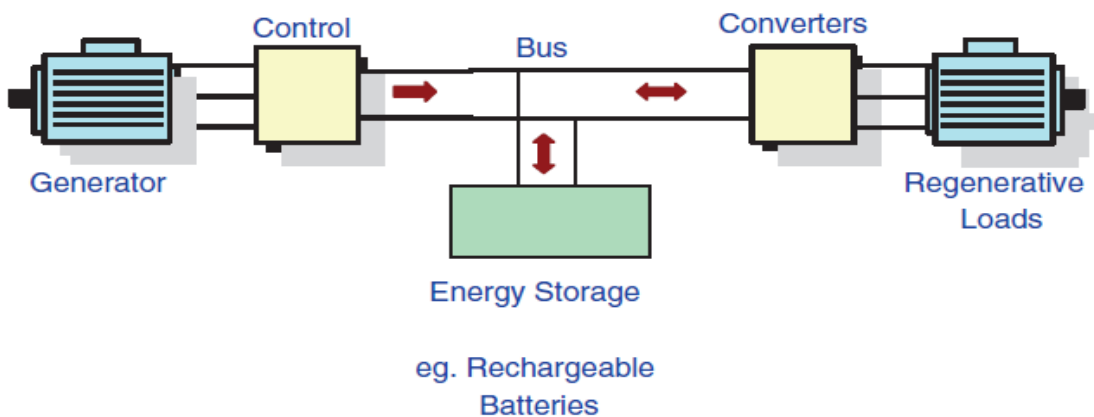


Figure 3-18 – Centralized energy storage

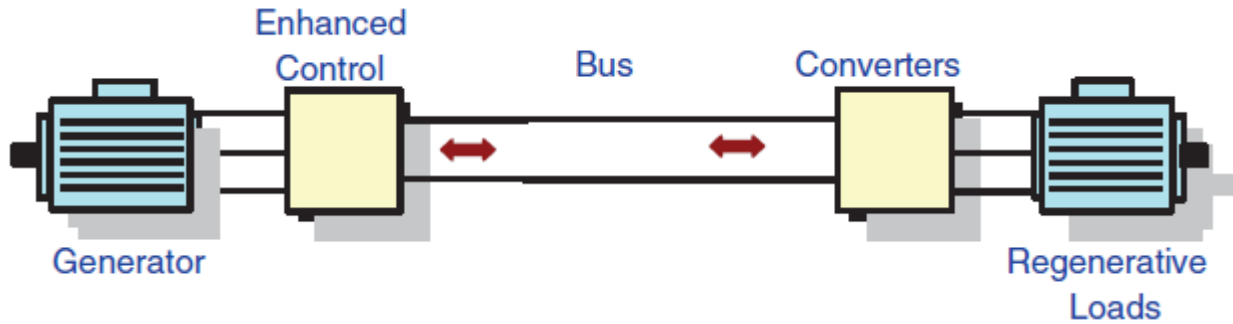


Figure 3-19 - Return energy to the source

3.9 MULTI-PHASE DRIVERS AND MACHINE

As mentioned above, applications MEA/MEE involving different aspects such as fault tolerance and redundancy, power density and torque, temperature range, cooling, performance and others. It is significant importance the aspect of reliability, in particular for drives to safety such as generators, the actuators of the flight surfaces and fuel pumps. A significant improvement can be obtained with the adoption of multi-phase drives and electrical machine.

A converter must be able to satisfy the demands of the electrical machine and loads. However, the performance of the drive may not exceed a certain range due to limitations of semiconductor devices. A solution to this problem is to use a multilevel converters because it is possible to develop high-power converters while using a small semiconductor device.

However, the advent the inverters that supply the motors and new modulation strategy, has removed the methodological bases that limit the number of phases of a motor. This fact has led to the design of electrical machine with more than three phases and this fact led to increased investigation of drives with multi-engine applications. The multi-phase machines can be used as an alternative to multi-level converters. Depending on the final application is definitely better to use an electric multi-phase machine rather than a multilevel converter.

With the employment of these new machines is possible, while making reference to converters of limited power, to obtain high power levels by dividing the power demand on multiple phases.

Chapter 4

DESIGN OF A MULTIPHASE INDUCTION

MACHINE FOR AN OPEN ROTOR

AERO-ENGINE SHAFT LINE EMBEDDED

STARTER/GENERATOR

4.1 ABSTRACT

The aerospace world has found in electrification the way to improve the efficiency, reliability and maintainability of an aircraft. This idea leads to the aircraft a new management and distribution of electrical services. On the other hand the fuel saving targets is drawing the attention toward new architectures. This chapter presents an method to design of a four-three-phase fault tolerant induction machine to be installed on the high pressure shaft of an open rotor jet engine. The integration of the generator on shaft of this kind of engine challenges the electric machine designer in facing, at the same time, the harsh environment and high reliability requirements. The paper presents the design of multi-phase fault tolerant induction machine to be installed on the high pressure shaft of an open rotor jet engine. In particular, the proposed solution is a four-three-phase induction machine.

4.2 INTRODUCTION

In the transport sector the "more electric" solutions are gaining attention with the aims at increasing energy efficiency and reliability leading to reduce emissions and maintenance costs. Many examples can be found: from road transport, where hybrid electric vehicles are gaining popularity [10] to the sea transport.

In this general frame, aerospace applications have found that the progressive electrification of on-board services is a way to reduce or to remove the dependence on hydraulic, mechanical and the bleed air/pneumatic system. The resulting step change in aircraft electrical loads has far reaching implication for electrical generation system.

The MEA approach has been widely discussed in the technical literature and the topic has been included in many of the most important international conferences and Journals [11]. One of the dominant themes is that of fault tolerance. The fault tolerance, together with the fault prevention, removal and forecasting, is one of the means to achieve dependability [12]. The fault tolerance is traditionally achieved by a complete parallel actuation; transportation applications, where the size and weight are important, demand optimized architectures including active redundancies. In motor drives the fault tolerance can be enhanced by phase modular redundancies; hence the interest toward multiphase machines.

Next to the idea of electrification of the aircraft, the worldwide aerospace research has been focus on new jet aero-engines architectures with the aim of minimizing fuel consumption and emissions: one of these architecture is the Open Rotor.

The goal of the idea is the optimal design a multi-phase fault tolerant starter/generator suitable for the installation on the high pressure shaft of a non-conventional jet aero-engine, with Open Rotor (OR) architecture (Figure 4-1). In particular, it is a four-three-phase induction machine designed for its integration to the high pressure shaft in the rear part of the engine.

4.3 OPEN ROTOR JET ENGINES

During the last several decades worldwide aerospace research has studied new aero-engines with the final aims if minimizing aviation impact, reducing CO₂ and NO_x emissions [13] [14]. Some project focus on the most advanced technologies to optimize existing engines while others aim at the design of radical new architectures [15]. In this scenario it has been extensively shown

energy vector requires improving the reliability of the generators.

There is growing acceptance that conventional drive systems will not be able to meet the reliability requirements and hence a level of redundancy is essential [18]. The more recent studies on the reliability of electromechanical actuators for MEA [19] have demonstrated that the multi-phase drive topology gives more advantages in terms of fault tolerant operation respect to the 3-phase counterpart. Moreover some of these studies discuss that a single multi-phase converter that supplies a multi-phase machine using star connection does not fulfil the fault tolerant operation required by the MEA applications [19]. To achieve true fault tolerant operations, the most promising multi-phase electrical machine configurations that can be used for the MEA applications are:

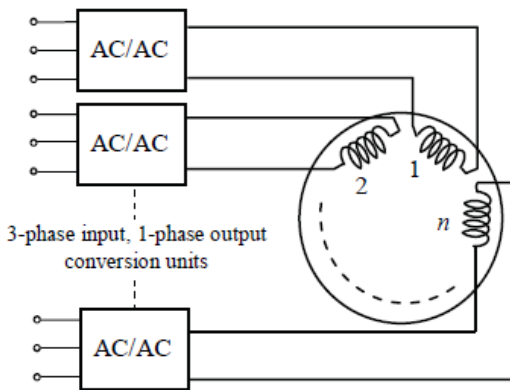


Figure 4-2 - Fault tolerant drive with multiple single-phase units

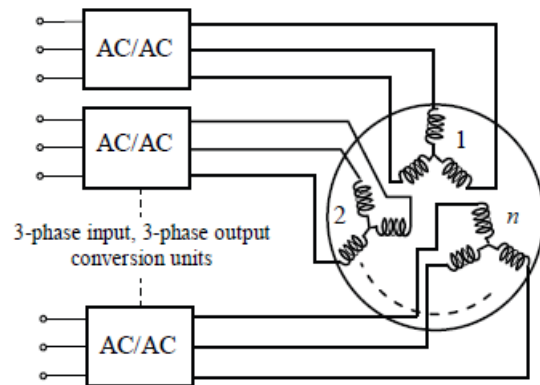


Figure 4-3 - Fault tolerant drive with multiple 3-phase units

- Multiple of independent single-phase units (Figure 4-2)
- Multiple of independent 3-phase units (Figure 4-3)

Current power-supply systems in civil aircraft usually are 3-phase voltage sources of 115V AC and the frequency can be constant or can vary between 300Hz and 800Hz. In some applications the voltage is now increased at 230V AC. Other solutions are DC voltage supply at 350V or 540V, while the 270V DC is used in military aircraft [20].

The candidate machines for the embedded starter/generator application are Induction Machines (IMs), Switched Reluctance Machines (SRMs) and Permanent Magnet Synchronous Machines (PMSMs). It is accepted that PMSMs provide higher torque density than SRMs and IMs, but they are less intrinsically fault tolerant [26]. The not-eliminable presence of the back emf induced by the rotating magnets poses severe problems in the faults management.

Furthermore the mechanical and thermal limits of the magnets could be not compatible with the temperature constrains (including demagnetization issues) of the application. On the other hand the high speed and relatively low torque demanded by the application make acceptable the lower torque density of the magnet less solutions that show also a "natural" flux weakening capability, required by the constant power generation profile.

4.5 MACHINE DESIGN CRITERIA

When approaching the design of a high speed Induction Machine (IM), the main constraints are the required output power, both as motor and generator, the maximum rotational speed of the rotor and furthermore the mechanical requirements, which are the dynamic stiffness and the vibration limits [21]. Further constraints are the torque overload capability at start-up and the power overload capability as generator at high speed. Therefore, a compromise must be found between electromagnetic and mechanical constraints.

Furthermore, the maximum operating frequency is limited by the thermal stresses of the power electronic components and by the machine iron losses, taking the air-gap flux density and the number of poles into account.

On the basis of the previous considerations, the following constraints have been adopted for the optimized design.

Air-gap mean diameter lower than	150 mm
Inner rotor diameter greater than	70 mm
Stator slot pitch greater than	8 mm
Air-gap width greater than	0.8 mm

4.6 DESIGN PROCEDURE

As is known, the main dimensions of the IM are related to the apparent power A and torque T by the following relationships [28]

$$\frac{A}{f L D^2} = \frac{\pi}{\sqrt{2}} K_a B_M \Delta \frac{1}{p} \quad (4-1)$$

$$\frac{T}{L D^2} = \frac{\pi}{2\sqrt{2}} K_a B_M \Delta \eta \cos(\varphi) \quad (4-2)$$

where f is the operating frequency, L and D represent the axial length and the air-gap mean diameter, B_M and Δ are the peak value

of the air-gap flux density and linear current density, p is the pole pairs number and K_a, η and $\cos(\varphi)$ are the winding factor, the efficiency and the power factor, respectively.

As is possible to see from (4-1) and (4-2), for given value of the required performance, the main dimensions L and D depend on the basic design parameters B_M and Δ .

The number of stator slots must be a multiple of the number of phases. In order to produce a sinusoidal distribution of the magnetomotive force at the air-gap, a distributed winding with an integer number q of slot per pole per phase should be chosen. The greater the number of stator slots the lower the value of the slot pitch. Due to the presence of the slot opening, increasing the number of slots the air-gap permeance will decrease, due to the increasing influence of the Carter's coefficient.

For a given number of stator slots, the number of the rotor slots must be chosen taking care of the magnetic interaction between stator and rotor teeth [22]. The number of conductors per slot n is given by

$$n = \frac{\sqrt{2} V_f}{K_a 2\pi f q B_M L D} \quad (4-3)$$

where V_f represents the rms value of the voltage applied to one of the phase winding.

By assuming a high value of the iron permeability, the constitutive relationships of the IM allows the calculation of the outer diameter of the stator once the surface current density J and the flux density B_{fe} in the teeth and in the yoke are selected.

These relationships equate the flux in a tooth to the flux in the slot pitch where the mean air-gap flux density is B_M . Particular attention should be given in cases where a very high value of the flux density may be chosen. In these cases a non-negligible magnetic flux will flow also through the slot and it must be considered. Further relationships equate the flux in the yoke to the half of the flux per pole $\Phi_M = B_M L D / p$. The radial dimension of the slot is calculated on the basis of the teeth dimensions taking the current in a slot $n I_f$, the value of J and the slot fill factor into consideration. The last one must be conservative, in respect of the reliability of the application.

The same considerations apply for the calculation of the inner diameter of the rotor. In this case, the rotor bar currents are calculated by using the power factor of the machine.

Once the overall dimensions are calculated, the equivalent circuit of the machine may be built, allowing the determination of

the characteristic curves of the machine, both in motor as well as in generator operation. The resulting performance may match, or not, the target design and constraints. In the positive case the design is a candidate for the optimization. In the negative case the design is discarded and new values of the design choices must be adopted.

Obviously, when performing the above described procedure, the final design must be consistent with the assumptions made in (4-1) and (4-2).

The characteristics of the optimized machine will strongly depend on the adopted active material stress. This, in turn, depends on the properties of the magnetic material. With reference to the target application, the Fe-Co alloys represent an optimal choice for the realization of the magnetic circuit [30]. In particular, reference is made to VACOFLUX 50, strip 0.2 mm, supplied by VACUUMSCHMELZE GmbH & Co. KG. The B-H curve adopted here for the design optimization is shown in Figure 4-4.

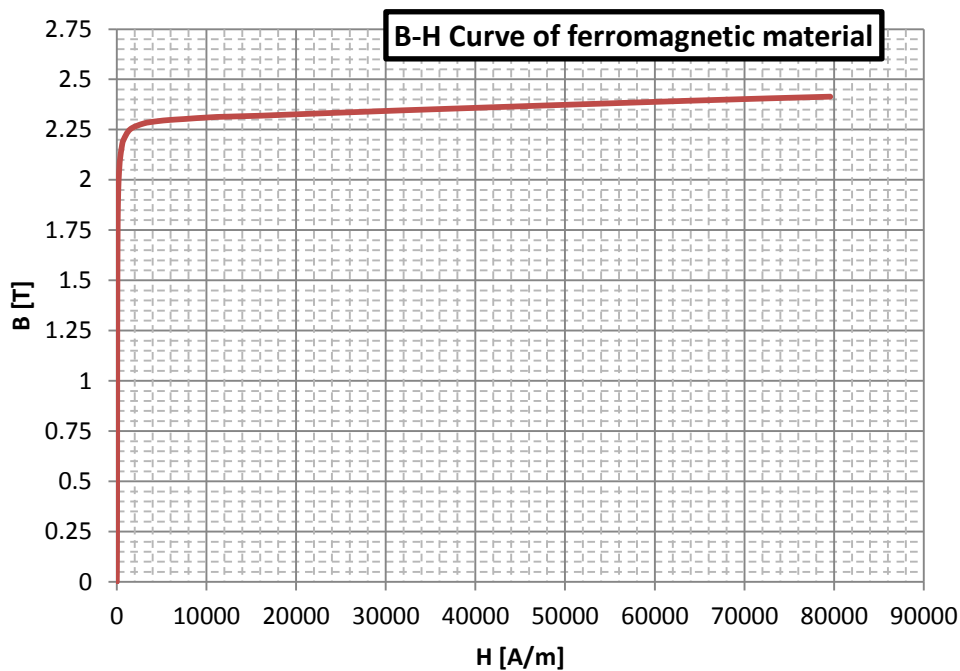


Figure 4-4 - B-H Curve of the magnetic alloy used for stator and rotor lamination

From Figure 4-4 it is possible to see that, using this alloy, the allowable flux density in the magnetic circuit can reach values up to 2 T and more, with very high relative values of the permeability, so avoiding iron saturation.

The specific losses p_{fe} of the magnetic material are calculated as a function of the local maximum value of the flux density B. On the basis of the properties of the chosen material, the iron

losses have been calculated with reference to Figure 4-5, were a suitable coefficient has been included, considering the effects of annealing and of the hardening of the sheet due to the punching operation.

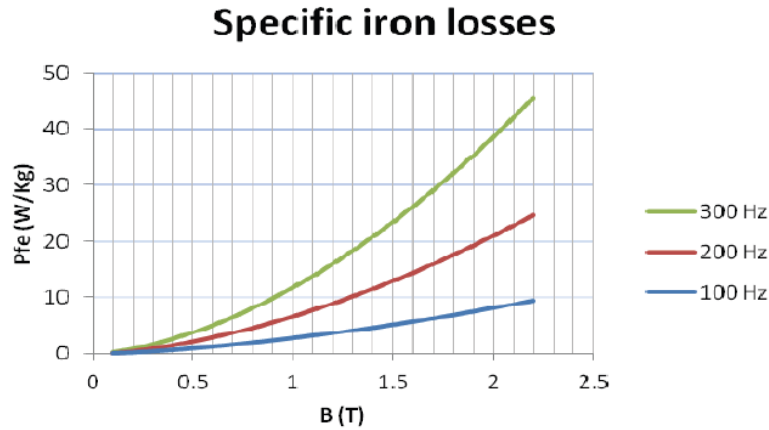


Figure 4-5 - Specific iron losses as a function of the maximum value of the flux density, including annealing conditions and the punching effects

The copper losses can be easily calculated at low frequency while at high frequency the skin effect strongly influence these losses. To reduce the skin effect, the thickness of a conductor in slot must be limited to proper thin level, which requires increasing the number of conductors in the slot height direction [23]

4.7 TARGET DESIGN AD PROTOTYPE

The candidate machines for the embedded starter/generator application are Induction Machines (IMs), Switched Reluctance Machines (SRMs) and Permanent Magnet Synchronous Machines (PMSMs). It is accepted that PMSMs provide higher torque density than SRMs and IMs, but they are less intrinsically fault tolerant. The not-eliminable presence of the back emf induced by the rotating magnets poses severe problems in the faults management. Furthermore the mechanical and thermal limits of the magnets (including demagnetization issues) could be not compatible with the temperature constrains of the application (including the thermal soak-back phenomenon at engine stop). On the other hand the high speed and relatively low torque demanded by the application make acceptable the lower torque density of the magnetless solutions that show also a "natural" flux weakening capability, required by the constant power generation profile.

A suitable machine model of the quadruple three-phase IM was derived in [24] by exploiting the potentialities of a specific

space vector transformation. The inherent degrees of freedom of the multiphase drive have been emphasized defining a technique for current sharing management among the four three-phase stator windings. The total machine electric power can be split among the four DC sources in a flexible way, with the usage of several degrees of freedom.

In [24] the authors investigate potentialities of the four-three-phase squirrel cage 100kVA induction machine characterized by the specifications listed in Table I. The high flux density of the Fe-Co alloys let to design lighter magnetic cores with different optimal trade-offs between copper and iron. For this reason Fe-Co laminations are rather common in the electric machine production for aerospace applications. The high speed of the motor-generator implies fundamental frequencies that bring the specific iron losses in the range of 50-100 W/kg. To cope with this issue together with the high cost and high specific weight of the material, can be convenient the reduction of the flux density in the stator core. This fact prevents the utter exploitation of the high flux density capability of the material, making viable the use of conventional Fe-Si lamination for the stator core; on the contrary, it is out of discussion the use of the Fe-Co alloy in the rotor, where the frequencies are low, letting the full exploitation of the material and more room for the copper or aluminum conductors

To investigate the potential improvement of the use of the Fe-Co lamination in the rotor core, in comparison with a total Fe-Si machine two scaled prototypes have been designed and realized. The used Fe-Co material is the VACOFLUX 50, supplied by VACUUMSCHMELZE GmbH & Co, while the Fe-Si lamination is the NO 20 supplied by Cogent Power Ltd. Both laminations have a thickness of 0.2 mm. In order to reduce the manufacturing costs of the prototypes, and to simplify the comparison, the same active length (80 mm), the same inner (110 mm) and outer (200 mm) diameter of the stator were adopted. The numbers of stator (48) and rotor (40) slots have been also assumed equal, as well as the slot fill factor.

For both the scaled-size prototypes the targets for the wanted performances are listed in Table II.

The performed design process allowed to find solutions with high efficiencies with acceptable power factors and thermal compatibility. The main differences of the two final designs are shown in Table III. For display purposes, Figure 4-6 allows to compare the two rotor laminations. As it is possible to see in Table III, the higher magnetic saturation level of the Cobalt Iron alloy led to thinner width of the stator and rotor teeth of the FeCo prototype even if it was designed with a lower number of conductors per slot which means a higher value of flux per pole. As a result of the design process, the expected rated performances of the two machines, for generator and motor operations, are as reported in Table IV and Table V, respectively. The manufacturing

process was performed by Electrical Discharge Machining (EMD) of the stator and rotor laminations. Then, the die cast rotors and the twelve phase wounded stators have been locked in the housing having shields equipped with ball bearings designed for the required high rotational speed. Also included were the temperature probes and the incremental encoders.

Table 4-1 - Characteristics of the Scaled Prototypes

Starter/Generator	
Number of phases	12 (4x3-phase, star connected)
Rated voltage of each 3-ph system	186 Vrms
Constant V/Hz operation up to	267 Hz
Generating mode	
Continuous output power	10 kVA
Constant power range	6000 to 15000 rpm
Overload	150% 5 min., 200% 5 sec
Cooling system	air, forced ventilation.

Table 4-2 - Differences in the Design-Result of the two Prototypes

	<i>Fe-Si rotor</i>	<i>Fe-Co rotor</i>
Stator tooth width	3.8 mm	3.6 mm
Stator yoke width	18 mm	20 mm
Conductor per slot	19	17
Rotor tooth width	3.8 mm	3.0 mm
Rotor yoke width	14 mm	16 mm

Table 4-3 - Generating-Mode, 10kVA electric output, rated voltage

	<i>Fe-Si Prototype</i>	<i>Fe-Co Prototype</i>
Rated speed	6079 rpm at 200 Hz	6055 rpm at 200 Hz
Rated current	10.3 A	10.3 A
Current density	4.1×10^6 A/m ²	4.0×10^6 A/m ²
Efficiency	94.8 %	94.9 %
Power factor	0.75	0.68

Table 4-4 - Motoring-Mode, 10kW Shaft power, rated voltage

	<i>Fe-Si Prototype</i>	<i>Fe-Co Prototype</i>
Rated speed	5914 rpm at 200 Hz	5941 rpm at 200 Hz
Rated current	10.6 A	11.5 A
Current density	4.3×10^6 A/m ²	4.4×10^6 A/m ²
Efficiency	93.0 %	93.2 %
Power factor	0.79	0.73



Figure 4-6 - Picture of the rotor laminations of the two prototypes FeSi (Left) and FeCo (right) External diameter is about 110mm

4.8 EQUIVALENT CIRCUIT PARAMETERS

MEASUREMENTS

For both the investigated prototypes the parameters of the electric equivalent circuits have been experimentally determined by the well-known no-load and locked rotor test [25]. The prototypes have been tested connecting the stator windings in three-phase mode, star connection, and using a programmable sinusoidal power supply (rated 40 kVA, 0-520 V, 50-300 Hz, voltage THD < 0.1%). Then, the machine parameters have been referred to the 12-phases connection.

4.8.1 NO LOAD TESTS

Six no-load tests have been performed changing the frequency from 50 Hz up to 300 Hz, with steps of 50 Hz. Due to the voltage limitation of the available power source, for frequency higher than 150 Hz it was not possible to get the rated flux conditions, and the maximum available supply voltage was used as reference voltage for the test elaborations.

Table 4-5 - No-Load test result for the Fe-Si 12 Phase Prototype

Frequency, (Hz)	50	100	150	200	250	300
12-phases ref. voltage, (V)	46.5	93	130	130	130	130
No-load current, (A)	5.54	5.59	5.06	3.54	2.77	2.29
Iron losses, (W)	30.5	85.3	105	103	97.4	91.6
Mechanic. losses, (W)	20.4	45.1	65.5	105	161	256

Table 4-6 - No-Load test result for the Fe-Co 12 Phase Prototype

Frequency, (Hz)	50	100	150	200	250	300
12-phases ref. voltage, (V)	46.5	93	130	130	130	130
No-load current, (A)	5.54	5.59	5.06	3.54	2.77	2.29
Iron losses, (W)	30.5	85.3	105	103	97.4	91.6
Mechanic. losses, (W)	20.4	45.1	65.5	105	161	256

For the Fe-Si and Fe-Co prototype, the no-load current, iron losses and mechanical losses estimated at the reference voltage are reported in Table 4-5 and Table 4-6. For a better understanding of these results, the iron and mechanical losses are shown in Figure 4-7 and Figure 4-8, respectively. It is possible to observe that in the whole frequency range the Fe-Co prototype has higher iron losses with respect to the Fe-Si counterpart. In flux weakening conditions (frequency higher than 150 Hz), the iron losses decrease for both the machines. The performed variable frequency no-load tests show that the two machines practically have the same mechanical losses (see Figure 4-8). This results was expected because the two prototypes are equipped with the same bearings.

Additional examples of no-load test results are reported in Figure 4-9 and Figure 4-10. The former figure shows the no-load current trends for two different frequencies where it is possible to reach the rated flux in the machine (stator Emf / frequency ratio equal to 0.93 V/Hz). The latter reports the iron losses still as function of the Emf/frequency ratio. Also in this case, it is possible to observe that the Fe-Co prototype is characterized by higher values of the no-load currents and iron losses.

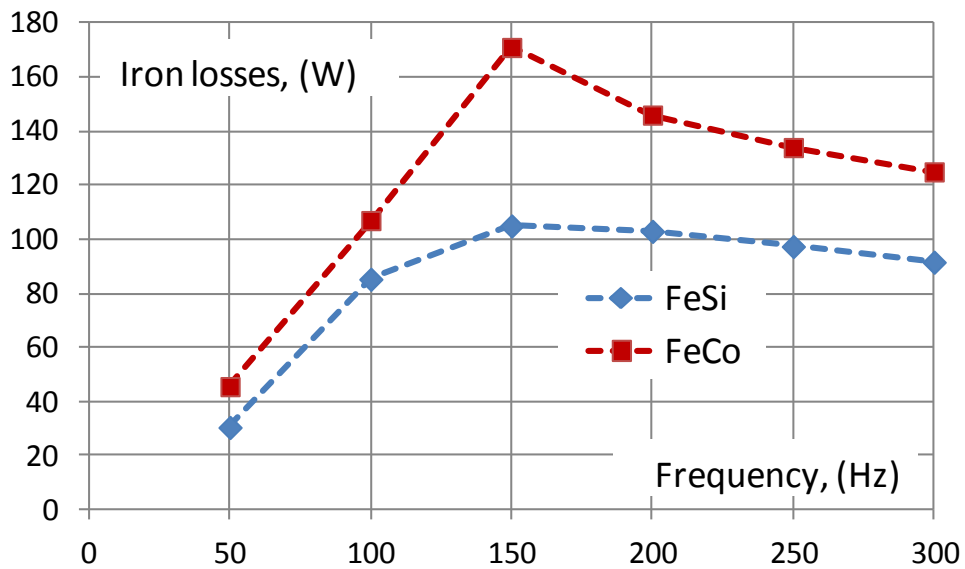


Figure 4-7 - No-load tests results: iron losses at the reference voltages as function of the supply frequency.

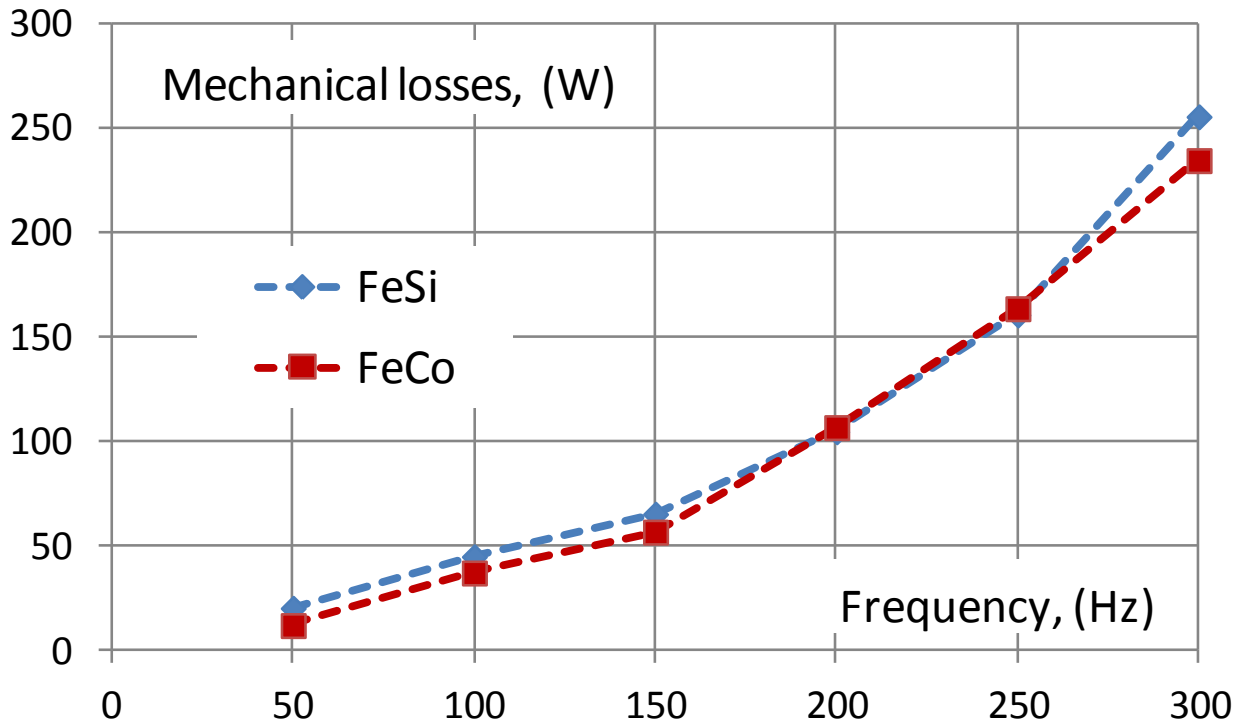


Figure 4-8 - No-load tests results: mechanical losses as function of the supply frequency

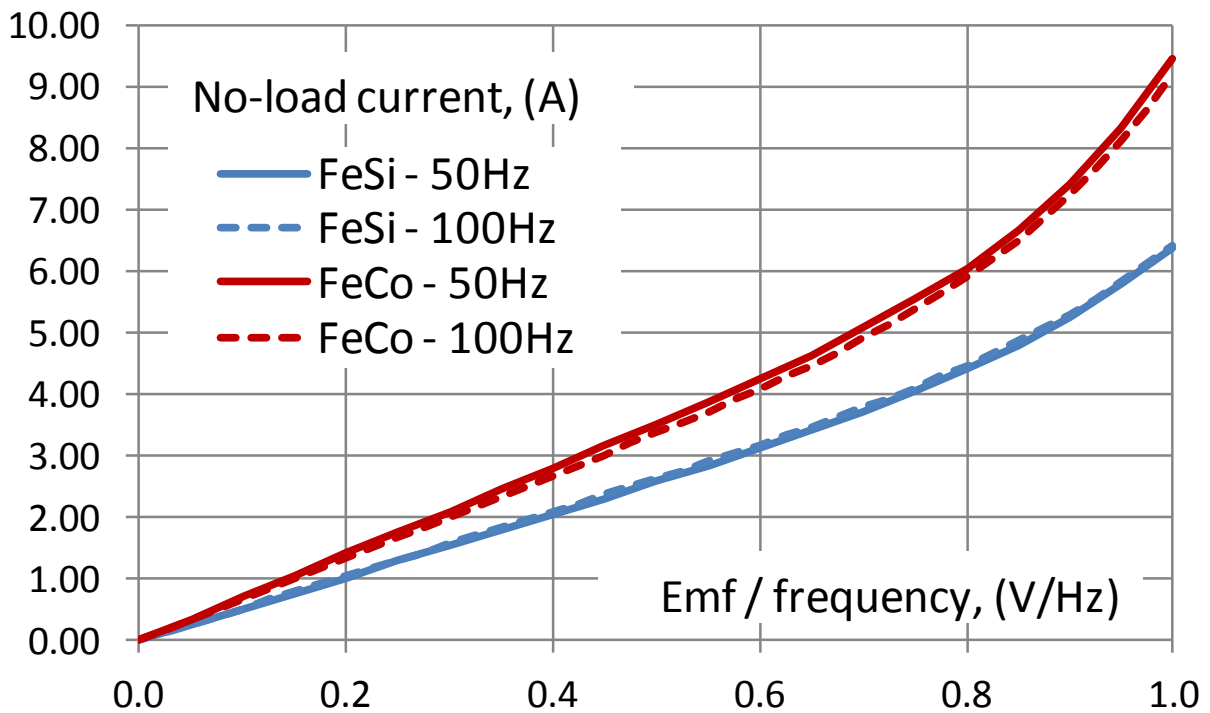


Figure 4-9 - No-load tests results: no-load current as function of the stator back Emf / f ratio for 50 Hz and 100 Hz

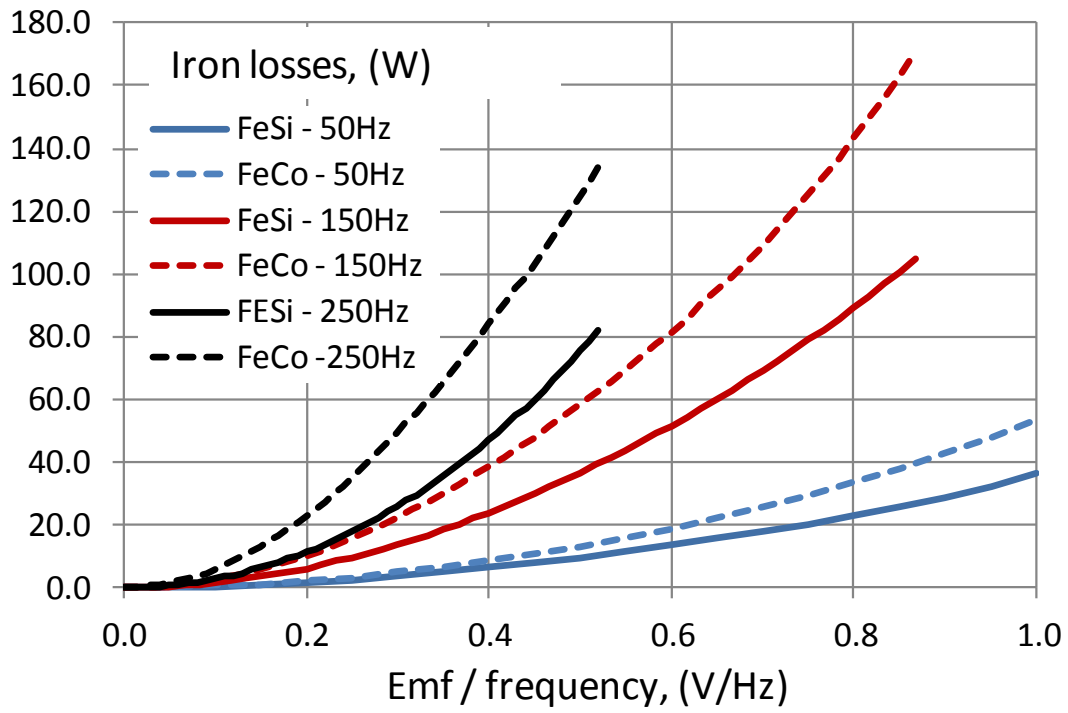


Figure 4-10 - No-load tests results: iron losses as function of the stator back Emf / f ratio for 50 Hz, 150 Hz, and 250 Hz

4.8.2 LOCKED ROTOR TESTS

The prototypes have been tested in locked rotor condition at the same frequency values adopted during the no-load tests. The computed locked rotor parameters for the two 12-phases prototypes are listed in and Table 4-8 for a reference phase current of 10 A and a reference temperature equal to 160 °C. These results put in evidence that the two machines have quite different values of locked rotor resistance and locked rotor reactance. It is important to remark that, for each test elaboration, the total locked rotor reactance has been split in the stator and rotor contributions in accordance to the adopted standard. Anyway, using all the performed locked rotor tests a different elaboration could be done in order to take into account, for example, the skin effect for the rotor parameters [26].

Table 4-7 - Locked Rotor Test Result for the Fe-Si 12 Phase prototype (Reference Current 10A, Reference Temperature 160°C)

Frequency, (Hz)	50	100	150	200	250	300
L.R. voltage, (V)	13.4	22.5	31.5	40	48.5	57
L.R. losses, (W)	564	699	828	946	1063	1170
Stator resistance, (Ω)	0.218	0.218	0.218	0.218	0.218	0.218
Rotor resistance, (Ω)	0.252	0.365	0.472	0.570	0.667	0.757
Stator reactance, (Ω)	0.308	0.581	0.838	1.089	1.334	1.571
Rotor reactance, (Ω)	0.308	0.581	0.838	1.089	1.334	1.571

Table 4-8 - Locked Rotor Test Result for the Fe-Co 12 Phase prototype (Reference Current 10A, Reference Temperature 160°C)

Frequency, (Hz)	50	100	150	200	250	300
L.R. voltage, (V)	9.2	15.6	21.8	28	33.7	40
L.R. losses, (W)	407	503	602	691	771	845
Stator resistance, (Ω)	0.188	0.188	0.188	0.188	0.188	0.188
Rotor resistance, (Ω)	0.156	0.236	0.319	0.392	0.460	0.521
Stator reactance, (Ω)	0.205	0.398	0.579	0.752	0.923	1.091
Rotor reactance, (Ω)	0.205	0.398	0.579	0.752	0.923	1.091

4.9 LOAD TEST AND VALIDATION OF THE

SIMULATIONS

At the moment, it is not yet possible to fix the Fe-Co prototype (feet mounting) on the test bench available in the laboratory. For this reason, the load tests have been performed on the Fe-Si prototype (flange mounting) only. The Fe-Si prototype has been positioned on the test bench (see Figure 4-11) and tested in load conditions connecting the 12 phases winding in three-phase mode. Again, due to the voltage limitation of the available three-phase power supply, the load tests were performed for a supply frequency of 50Hz and 100Hz, where it was possible to provide the rated flux to the machine. During the load tests the adsorbed electrical quantities, the shaft torque and speed have been recorded, together the stator winding temperature (by means of the stator resistance measure at the beginning and the end of test).

Aims of the performed load tests were the validation of the machine performances computed by means of the equivalent circuit. Since the machine parameters have been directly measured on machine, and the non-linearity due to the magnetic saturation (on the iron losses and magnetizing current), such as the skin effect (for the rotor resistance and the rotor leakage) are taken into account in the equivalent circuit, a good accuracy of the simulation results is expected. Anyway, it is an authors' opinion that an experimental validation is mandatory in order to be confident on the Fe-Si and Fe-Co motor performance comparisons presented in next section. Referring the motor parameters to the working temperature measured during the 50Hz and 100 Hz load tests, the agreement between measurements and simulations has been found to be very good, both for the electrical and mechanical quantities. Due page limitation reasons, only few examples of the results for the load test at 100 Hz can be presented here. In particular, from Figure 4-12 up to Figure 4-14 the torque, stator current and power factor characteristic versus the speed are shown.

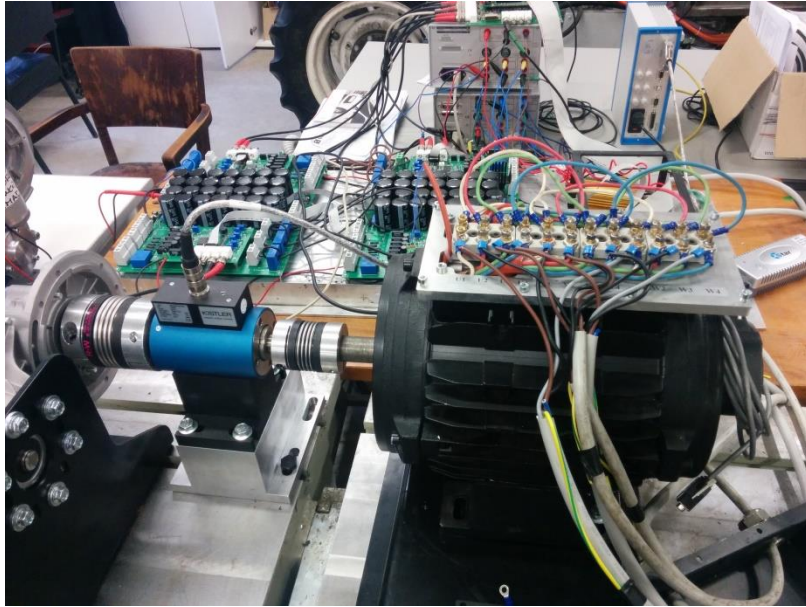


Figure 4-11 - Fe-Co prototype mounted on the test bench

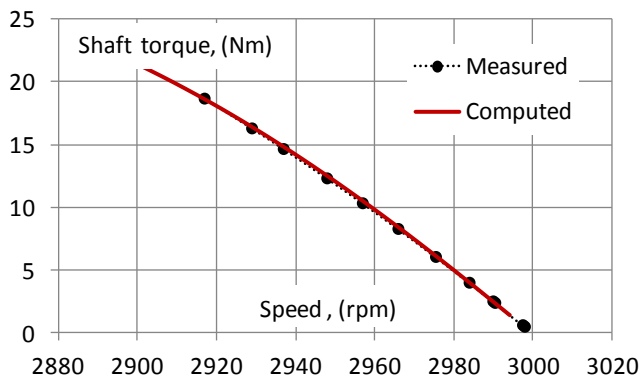


Figure 4-12 - Torque-speed characteristic of the Fe-Si prototype ($f=100$ Hz, reference temperature 46°C)

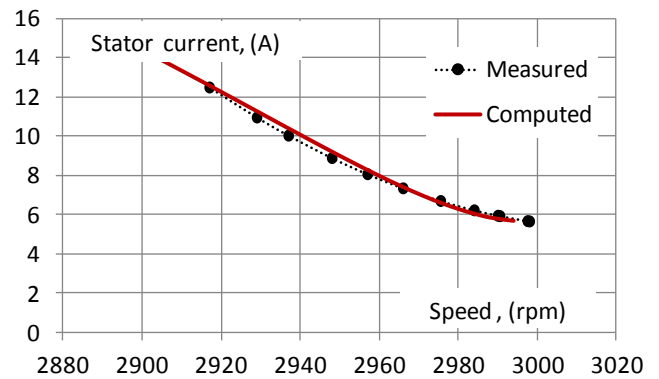


Figure 4-13 - Stator Current vs speed of the Fe-Si Prototype ($f=100\text{Hz}$, reference temperature 46°C)

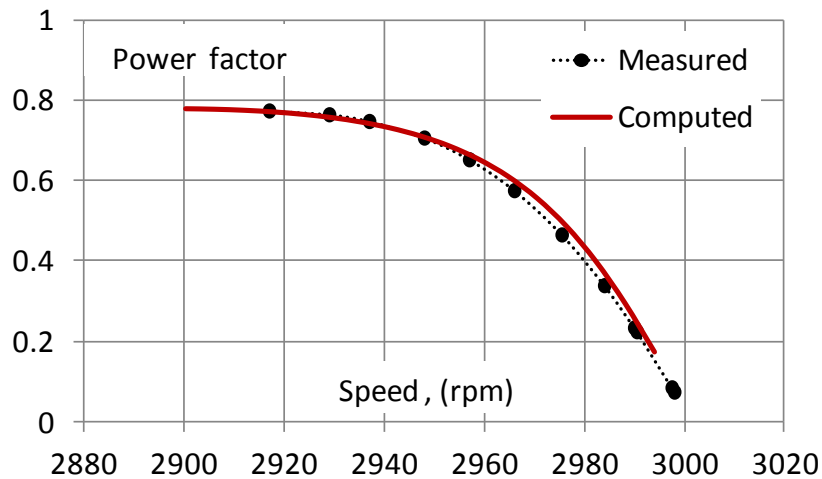


Figure 4-14 - Power Factor vs speed of the Fe-Si prototype (f=100 Hz, reference temperature 46°C)

4.10 PROTOTYPE PERFORMANCE COMPARISONS

Operations at the rated supply of 200 Hz have been initially simulated for both the prototypes. The measured equivalent circuit parameters have been referred to the rated voltage (186 V for the 12-phases connection) and the temperature of 160 °C. The computed performances are reported in the following figures. In particular, the torque-speed characteristics are reported in Figure 4-15 and Figure 4-16, where it is possible observing that, with respect to the Fe-Si prototype, the Fe-Co one is able to provide a higher maximum torque and a steeper trend of the stable region. A good overload capacity for the Fe-Co prototype is very welcome because in the considered starter-generator application a wide constant power speed range regulation is required. On the other hand, for a definite speed, the adsorbed current will be higher for the Fe-Co machine, as shown in Figure 4-17, resulting in bigger Joule losses (see Figure 4-18). From the power factor point of view, there are not so significant differences between the two machines, at least for torque values lower than 20 Nm (or speed higher than 5900 rpm), as proven by Figure 4-14. With respect to the efficiency, the Fe-Co prototype results to be better of the Fe-Si counterpart. Looking at Figure 4-20, in the speed range 5900-5950 rpm (that correspond to a torque range of 20-10 Nm) the efficiency improvements can be estimated in 1-2 percentage points.

Finally, the same simulations have been also done for a supply frequency equal to 50 and 100 Hz. The main motor performances for the three considered frequencies and rated powers (50Hz-2.5kW, 100Hz-5kW, and 200Hz-10kW) are listed in Table 4-9. Without enter again in the details, also the simulations at the new frequencies confirm all the previously reported considerations derived for the 200Hz case.

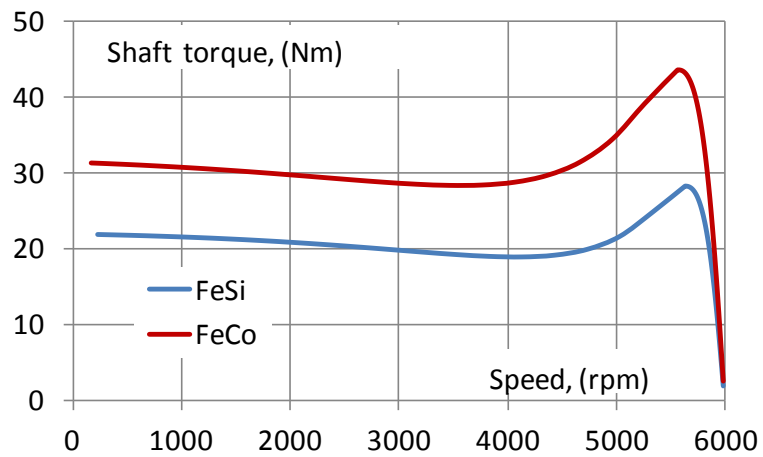


Figure 4-15 - Torque speed characteristics

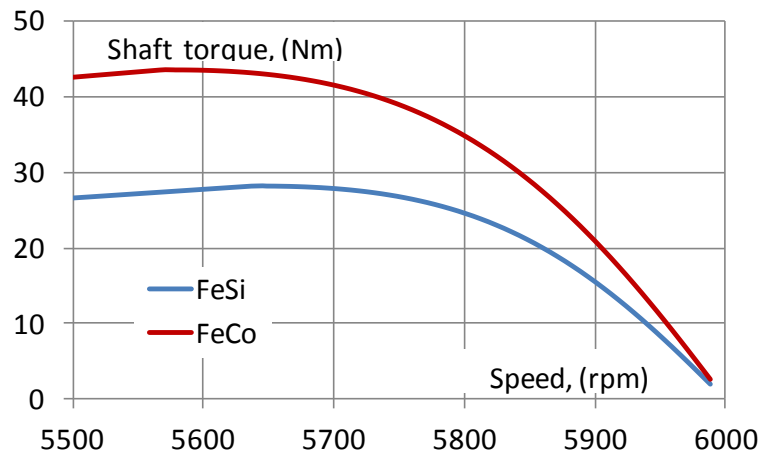


Figure 4-16 - Torque-Speed characteristics detail of the stable region

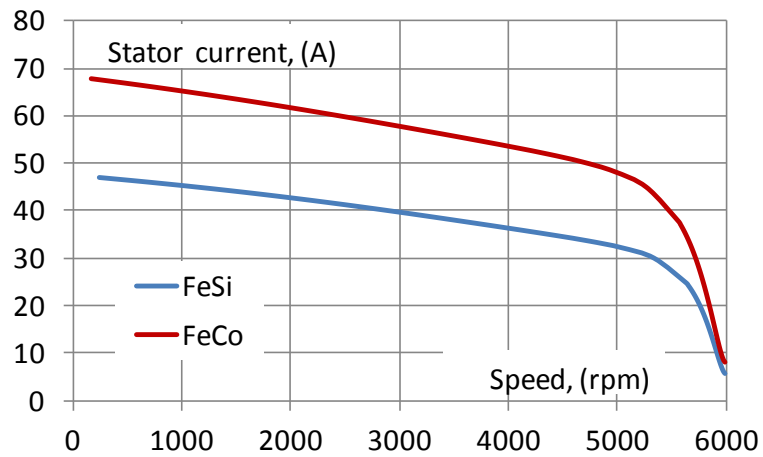


Figure 4-17 - Stator current vs speed characteristics

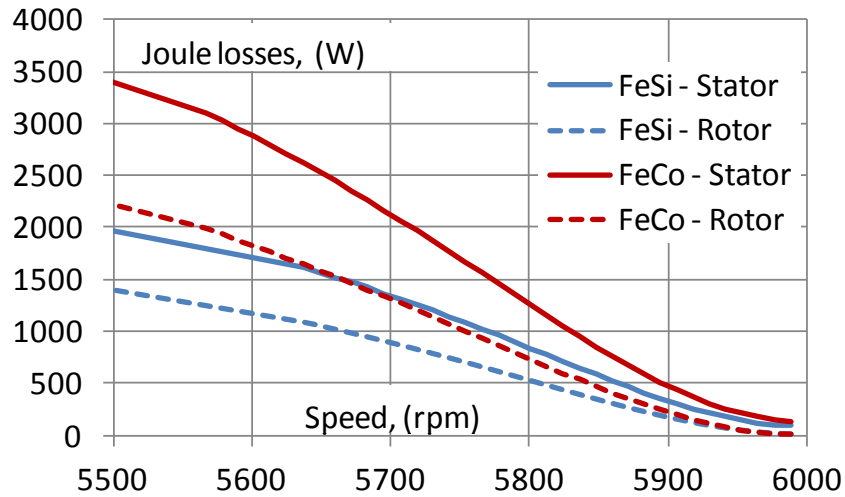


Figure 4-18 - Stator and rotor Joule losses vs speed characteristics

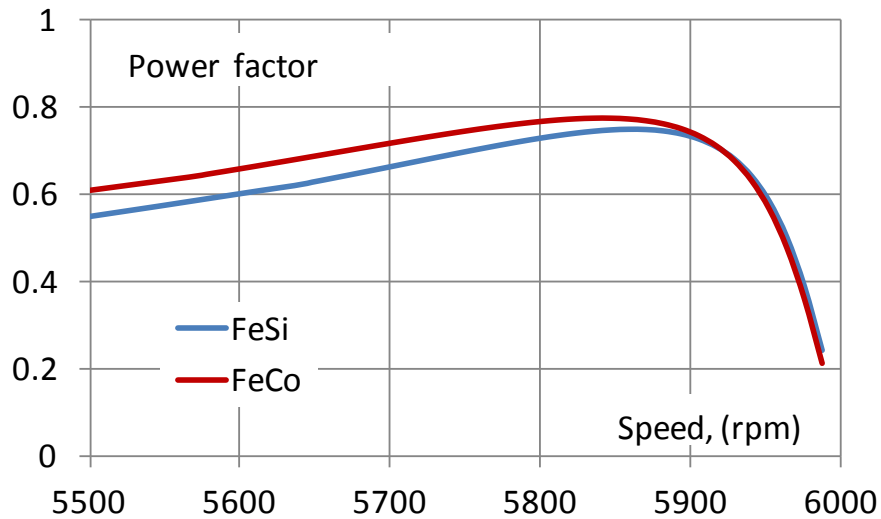


Figure 4-19 - Power factor vs speed characteristics

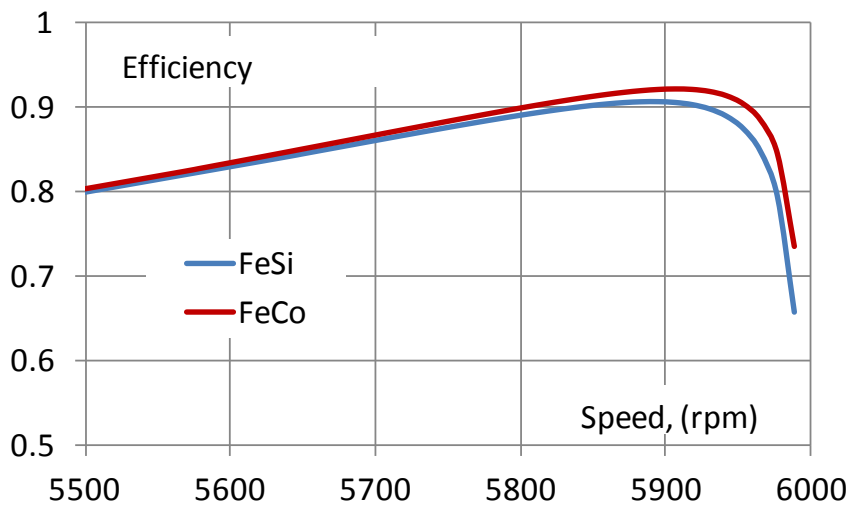


Figure 4-20 - efficiency-speed characteristics

Table 4-9 - Simulation result for the Fe-Si and Fe-Co 12 Phase Prototypes (Reference temperature 160°C)

	FeSi	FeCo	FeSi	FeCo	FeSi	FeCo
Frequency, (Hz)	50		100		200	
Shaft power, (W)	2500		5000		10000	
Supply voltage, (V)	46.5		92.7		186	
Speed, (rpm)	1411	1427	2897	2930	5895	5925
Slip %	5.91	4.89	3.43	2.33	1.76	1.25
Stator current, (A)	11.9	12.2	11.4	12.0	11.5	12.2
Adsorbed power, (kW)	3.08	3.01	5.64	5.57	11.0	10.9
Shaft torque, (Nm)	16.9	16.7	16.5	16.3	16.2	16.1
Efficiency	0.81	0.83	0.88	0.90	0.91	0.92
Power factor	0.80	0.76	0.77	0.72	0.74	0.69

4.11 CONCLUSIONS

By comparing the calculated results shown in Table 4-9 with the expected performance of the two prototypes reported in Table V, it appears that the slip, at rated power and frequency, is larger than expected. This situation usually happens when the rotor resistance is larger than expected. In our case, the increased resistance could be due to the presence of an anomalous level of impurities during the mold of the die casting of prototypes. Another difference appears in the values of the currents at rated load which are larger in the realized prototypes than expected. This could be due to an inadequate representation of the B-H characteristics of the magnetic materials and/or to a degradation of the magnetic properties of the stator and rotor surfaces facing the air-gap. As a consequence, the higher values of the currents determine lower values of power factors.

Both the higher slip values and the higher stator currents lead to the lower values of the efficiency compared to the expected ones. The calculated results confirm that the use of the cobalt-iron lamination allows for overall better performances of the Fe-Co prototype in terms of lower rated slip and higher efficiency. These better performances have been obtained at the expense of the lower value of the power factor of the Fe-Co

prototype. Finally, it must be noted that, as it is shown in Figure 4-15 and Figure 4-16, the maximum torque and the peak value of the output power of the Fe-Co prototype are greatly better than that of Fe-Si prototype, ensuring an improved reliability during overload operations.

The next step will be the development of the third scaled machine with both the stator and the rotor cores made of Fe-Co laminations, to assess the advantages and the drawbacks of the different choices.

Chapter 5

DYNAMIC STATOR CURRENT SHARING IN

QUADRUPLE THREE-PHASE INDUCTION

MOTOR DRIVE

5.1 ABSTRACT

In this chapter, a Field Oriented Control scheme for torque and rotor flux regulation of a quadruple three-phase induction machine is presented. Each three-phase stator winding is independently supplied by a conventional three-phase inverter. The presented motor drive can be utilized in medium and high power systems. Furthermore, owing to the intrinsic redundant structure, it can be employed for applications requiring a high degree of reliability, such as More Electric Aircraft. A specific machine model is achieved by introducing a proper multiple space vector transformation, suitable for the particular stator winding arrangement of the machine. Furthermore, exploiting the degrees of freedom of the system, a current sharing management technique among the four three-phase stator windings is presented. In this way, a flexible power flow control can be employed. The modulation strategy of the four three-phase inverters is based on the principle of three-phase decomposition. The effectiveness of the presented control scheme is verified by means of numerical simulations

5.2 INTRODUCTION

Multi-phase motor drives have many advantages with respect to their three-phase counterparts. In particular, the load power can be split into multiple phases, leading to Voltage Source Inverters (VSIs) having switching devices with limited power and current rating. Furthermore, the additional degrees of freedom related to a higher number of phases of the drive can be successfully exploited in different ways, such as increasing the electrical machine torque density, developing multi-motor drives, and improving the fault tolerant capability [27], [28]. Nowadays, multiphase drives are recognized as a viable approach for high-power applications and can be employed in systems in which a high degree of reliability is required.

Among the multiphase drives, the multiple three-phase ones are particularly attractive, since they exploit the well-known three-phase technology for the conversion structure. Dual, triple and quadruple three-phase machines have been employed in several applications [29], [30], [31], [32]. Owing to their redundant structure, multiple three-phase drives ensure a high degree of fault tolerant capability, which is appreciated in some critical applications, such as More Electric Aircraft (MEA). The MEA technology is based on the idea of replacing hydraulic and pneumatic actuators with their corresponding electromagnetic counterparts [33]. In particular, the aeronautic propulsion system can be improved, according to the More Electric Engine (MEE) philosophy, adopting an electric multiphase starter-generator embedded within the main aircraft engine [34]. This multiphase machine can be used as a motor for the starting and as generator during the flight. The key advantages of MEE are the removal of the hydraulic pumps and of pneumatic starting system, and the optimization of the operation of the aircraft motor.

In this chapter, a quadruple three-phase induction motor drive is presented. In the machine, four three-phase stator windings with isolated neutral points, supplied independently by four two-level three-phase VSIs with separated dc sources, are arranged in the stator slots with a spatial shift of 15° electrical degrees. A schematic draw of the induction motor drive is illustrated in Fig. 1. Note that, the four VSIs can be supplied also by only one dc source. The description of the quadruple three-phase machine is not trivial, due to the magnetic coupling among the four three-phase windings. Therefore, a suitable machine model is derived by exploiting the potentialities of an opportune multiple space vector transformation. The proposed transformation can be considered a generalization of the one presented in [35] for a dual three-phase machine.

A conventional Field Oriented Control (FOC) scheme is adopted for torque and rotor flux regulation, whereas the additional

degrees of freedom of the multiphase drive are utilized for the management of the stator current sharing among the four three-phase stator windings. This feature allows a flexible power flow control to be obtained. A similar approach has been used in [36] for a dual three-phase induction machine. Note that, the fault operating conditions due to the stop of one or more inverters, can be simply accomplished with a particular choice of the stator current sharing coefficients. The definition of the modulation strategy for the four three-phase VSIs is not so straightforward. Some solutions, based on Vector Space Decomposition, have been proposed in [37], but they are valid for dual three-phase machines, only in particular operating conditions, and cannot be easily generalized. In this paper, the principle of the three-phase decomposition of multiphase systems [38] is adopted. In this way, the well-known modulation strategies available for three-phase VSIs can be utilized.

The effectiveness of the proposed quadruple three-phase induction motor drive, with stator current sharing capability, is verified by means of simulation results. A system prototype is under development.

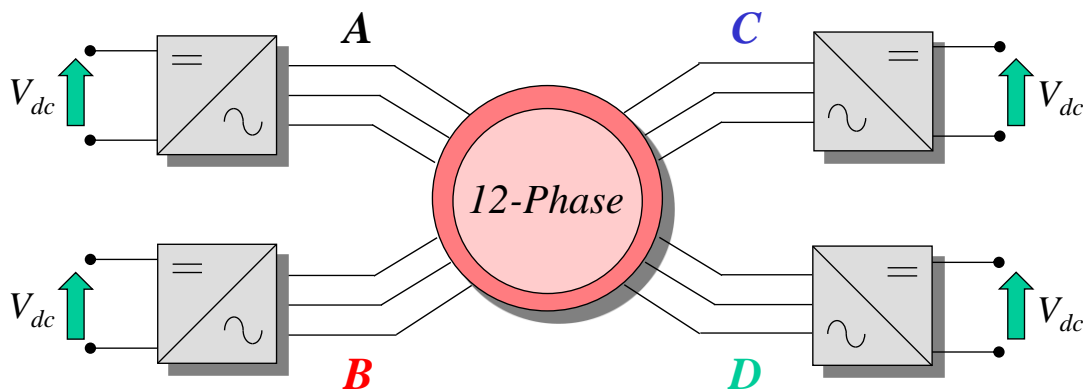


Figure 5-1 - Structure of the quadruple three-phase induction motor drive

5.3 QUADRUPLE THREE-PHASE INDUCTION MACHINE

The quadruple three-phase induction machine is equipped with a squirrel cage rotor. Four three-phase windings, named A, B, C, and D, spatially shifted of 15° electrical degrees, are arranged in the stator slots. Each three-phase winding is separately star-connected. The positions of the magnetic axes of the twelve stator windings are illustrated in Figure 5-2.

5.3.1 MACHINE MODEL

The machine model can be developed by starting from the analysis of the air gap magnetic field produced by the stator currents. Under the assumptions usually adopted for the analysis of ac machines, the stator magnetic field can be expressed, in a stator reference frame, in terms of three-phase stator current space vectors in the following compact form:

$$\begin{aligned}
 h_s(\vartheta_s, t) = & \frac{3N_s K_{ws1}}{2\pi\delta p} \Re[(\bar{i}_{sA} + \bar{\alpha} \bar{i}_{sB} + \bar{\alpha}^2 \bar{i}_{sC} + \bar{\alpha}^3 \bar{i}_{sD})] e^{-j\vartheta_s} \\
 & - \frac{3N_s K_{ws5}}{10\pi\delta p} \Re[(\bar{i}_{sA}^* + \bar{\alpha}^5 \bar{i}_{sB}^* + \bar{\alpha}^{10} \bar{i}_{sC}^* + \bar{\alpha}^{15} \bar{i}_{sD}^*)] e^{-j5\vartheta_s} \\
 & - \frac{3N_s K_{ws7}}{10\pi\delta p} \Re[(\bar{i}_{sA} + \bar{\alpha}^7 \bar{i}_{sB} + \bar{\alpha}^{14} \bar{i}_{sC} + \bar{\alpha}^{21} \bar{i}_{sD})] e^{-j7\vartheta_s} \\
 & - \frac{3N_s K_{ws5}}{10\pi\delta p} \Re[(\bar{i}_{sA}^* + \bar{\alpha}^{11} \bar{i}_{sB}^* + \bar{\alpha}^{22} \bar{i}_{sC}^* + \bar{\alpha}^9 \bar{i}_{sD}^*)] e^{-j11\vartheta_s}
 \end{aligned} \tag{5-1}$$

where, N_s is the number of series-connected conductors per phase, δ is the air gap length, p the number of pairs of poles, \Re the real part operator, $K_{ws\rho}$ the ρ -th winding coefficient, θ_s a stationary angular coordinate in electrical radians whose origin is aligned with the magnetic axis of phase A_1 , whereas \bar{i}_{sA} , \bar{i}_{sB} , \bar{i}_{sC} , and \bar{i}_{sD} are the three-phase stator current space vectors (see Appendix). The symbol "*" identifies the complex conjugate quantities.

Besides the fundamental component, (5-1) takes into account the fifth, the seventh and the eleventh spatial harmonic, and is expressed in terms of the instantaneous values of the stator currents. Note that the third and the ninth spatial harmonic are null, since they can be generated only by the zero-sequence components of the stator currents, which are zero owing to the star connection of the windings.

The analysis of (5-1) suggests the definition of four new space vectors (multiple space vectors), whose direct and inverse transformations are illustrated in Appendix. The adopted multiple space vectors, specifically defined for quadruple three-phase machines, allow (5-1) to be rewritten as

$$\begin{aligned}
 h_s(\vartheta_s, t) = & \frac{6N_s K_{ws1}}{\pi\delta p} \Re[\bar{i}_{s1} e^{-j\vartheta_s}] + \frac{6N_s K_{ws5}}{5\pi\delta p} \Re[\bar{i}_{s5} e^{-j5\vartheta_s}] \\
 & - \frac{6N_s K_{ws5}}{7\pi\delta p} \Re[\bar{i}_{s7} e^{-j7\vartheta_s}] - \frac{6N_s K_{ws5}}{11\pi\delta p} \Re[\bar{i}_{s11} e^{-j11\vartheta_s}] -
 \end{aligned} \tag{5-2}$$

As can be seen, the stator current space vectors \bar{i}_{S1} , \bar{i}_{S5} , \bar{i}_{S7} , and \bar{i}_{S11} independently generate the first, the fifth, the seventh and the eleventh spatial harmonic components of the magnetic field in the air gap, respectively. In the following, sinusoidal distributed stator windings are assumed ($K_{wS5}=K_{wS7}=K_{wS11}=0$), and then, only the space vector \bar{i}_{S1} produces air gap magnetic field.

It can be demonstrated that the mathematical model of the quadruple three-phase induction machine, expressed in terms of multiple space vectors in a stationary reference frame, can be written as follows:

$$\bar{V}_{S1} = R_S \bar{i}_{S1} + \frac{d\bar{\varphi}_{S1}}{dt} \quad (5-3)$$

$$\bar{\varphi}_{S1} = L_{S1} \bar{i}_{S1} + M_1 \bar{i}_{R1} \quad (5-4)$$

$$0 = R_R \bar{i}_{R1} - j p \omega_m \bar{\varphi}_{R1} - \frac{d\bar{\varphi}_{R1}}{dt} \quad (5-5)$$

$$\bar{\varphi}_{R1} = M_1 \bar{i}_{S1} + L_{R1} \bar{i}_{R1} \quad (5-6)$$

$$T = 6p M_1 \bar{i}_{S1} \cdot j \bar{i}_{R1}, \quad (5-7)$$

$$\bar{v}_{S5} = R_S \bar{i}_{S5} + L_{S\ell 5} \frac{d\bar{i}_{S5}}{dt} \quad (5-8)$$

$$\bar{v}_{S7} = R_S \bar{i}_{S7} + L_{S\ell 7} \frac{d\bar{i}_{S7}}{dt} \quad (5-9)$$

$$\bar{v}_{S11} = R_S \bar{i}_{S11} + L_{S\ell 11} \frac{d\bar{i}_{S11}}{dt} \quad (5-10)$$

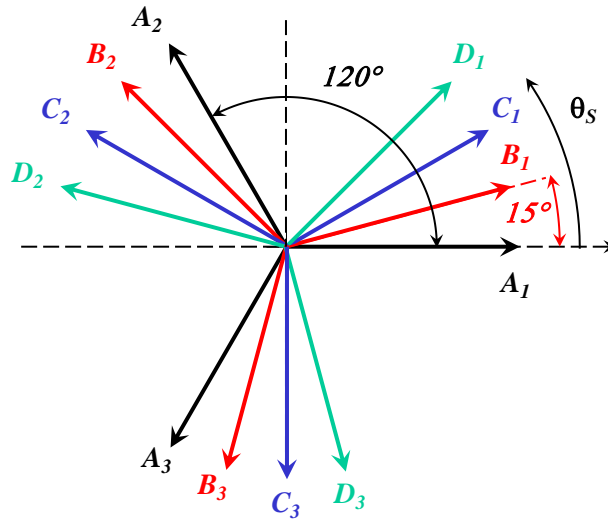


Figure 5-2 - Spatial position of the magnetic axes of the twelve stator windings

where L_{S1} , L_{R1} , and M_1 are respectively the stator, the rotor, and the mutual inductances of α_1 - β_1 plane, whereas L_{S5} , L_{S7} , and L_{S11} are the stator leakage inductances of α_5 - β_5 , α_7 - β_7 , and α_{11} - β_{11} planes.

Four decoupled sets of equations can be recognized. The first one, i.e., (5-3) - (5-7), concerns the variables of the α_1 - β_1 plane, namely the variables involved in the electromagnetic conversion process and then in torque and air-gap flux generation. The second one, the third one, and the fourth one, represented by (5-8), (5-9) and (5-10), are related to the variables of α_5 - β_5 , α_7 - β_7 , and α_{11} - β_{11} planes (auxiliary variables), respectively.

As can be seen, the control of torque and flux is achieved by acting on the space vector \bar{v}_{S1} in the α_1 - β_1 plane. However, also the space vectors \bar{v}_{S5} , \bar{v}_{S7} , and \bar{v}_{S11} , in the other α - β planes, must be taken contemporarily under control, since they define the current sharing among the four three-phase stator windings, as demonstrated in follow section.

5.3.2 THREE-PHASE SPACE VECTOR

The behaviour of the quadruple three-phase induction machine can be described in terms of four three-phase space vectors, one for each three-phase stator winding. The well-known linear transformations are

$$\bar{x}_A = \frac{2}{3} [x_{A1} + x_{A2} \bar{\alpha}^8 + x_{A3} \bar{\alpha}^{16}] \quad (5-11)$$

$$\bar{x}_B = \frac{2}{3} [x_{B1} + x_{B2} \bar{\alpha}^8 + x_{B3} \bar{\alpha}^{16}] \quad (5-12)$$

$$\bar{x}_C = \frac{2}{3} [x_{C1} + x_{C2} \bar{\alpha}^8 + x_{C3} \bar{\alpha}^{16}] \quad (5-13)$$

$$\bar{x}_D = \frac{2}{3} [x_{D1} + x_{D2} \bar{\alpha}^8 + x_{D3} \bar{\alpha}^{16}] \quad (5-14)$$

Note that, $\alpha = \exp(j\pi/12)$. The zero-sequence components are null due to the four isolated neutral points

5.3.3 MULTIPLE SPACE VECTORS

A more useful model of the quadruple three-phase induction machine can be achieved by introducing four specific space vectors (multiple space vectors), which are defined according to the

arrangement of the stator windings in the slots. The linear transformations are the following

$$\bar{y}_1 = \frac{1}{4} \left[\bar{x}_A + \bar{x}_B \bar{\alpha} + \bar{x}_C \bar{\alpha}^2 + \bar{x}_D \bar{\alpha}^3 \right] \quad (5-15)$$

$$\bar{y}_5 = \frac{1}{4} \left[\bar{x}_A^* + \bar{x}_B^* \bar{\alpha}^5 + \bar{x}_C^* \bar{\alpha}^{10} + \bar{x}_D^* \bar{\alpha}^{15} \right] \quad (5-16)$$

$$\bar{y}_7 = \frac{1}{4} \left[\bar{x}_A + \bar{x}_B \bar{\alpha}^7 + \bar{x}_C \bar{\alpha}^{14} + \bar{x}_D \bar{\alpha}^{21} \right] \quad (5-17)$$

$$\bar{y}_{11} = \frac{1}{4} \left[\bar{x}_A^* + \bar{x}_B^* \bar{\alpha}^{11} + \bar{x}_C^* \bar{\alpha}^{22} + \bar{x}_D^* \bar{\alpha}^9 \right] \quad (5-18)$$

where the symbol "*" identifies the complex conjugate operator. The corresponding inverse transformations are

$$\bar{x}_A = \bar{y}_1 + \bar{y}_5^* + \bar{y}_7 + \bar{y}_{11}^* \quad (5-19)$$

$$\bar{x}_B = \bar{y}_1 \bar{\alpha}^{23} + \bar{y}_5^* \bar{\alpha}^5 + \bar{y}_7 \bar{\alpha}^{17} + \bar{y}_{11}^* \bar{\alpha}^{11} \quad (5-20)$$

$$\bar{x}_C = \bar{y}_1 \bar{\alpha}^{22} + \bar{y}_5^* \bar{\alpha}^{10} + \bar{y}_7 \bar{\alpha}^{10} + \bar{y}_{11}^* \bar{\alpha}^{22} \quad (5-21)$$

$$\bar{x}_D = \bar{y}_1 \bar{\alpha}^{21} + \bar{y}_5^* \bar{\alpha}^{15} + \bar{y}_7 \bar{\alpha}^3 + \bar{y}_{11}^* \bar{\alpha}^9 \quad (5-22)$$

5.4 STATOR AND CURRENT SHARING CONTROL

STRATEGY

In this Section, a control strategy able to control the stator current sharing is presented. Since machine equations (5-3) - (5-7) are similar to that of a three-phase induction machine, a conventional FOC scheme can be adopted to control torque and rotor flux. Therefore, the stator current vector \bar{i}_{s1} depends on the drive operating condition, i.e., torque reference, rotor flux reference, and rotor speed. On the contrary, the auxiliary stator current vectors \bar{i}_{s5} , \bar{i}_{s7} , and \bar{i}_{s11} can be considered as degrees of freedom, and can be exploited in order to manage the current sharing among the four three-phase stator windings.

According to (5-19), the space vector \bar{i}_{s1} of the stator current can be expressed as

$$\bar{i}_{S1} = \frac{1}{4} \left[\bar{i}_{SA} + \bar{i}_{SB} \bar{\alpha} + \bar{i}_{SC} \bar{\alpha}^2 + \bar{i}_{SD} \bar{\alpha}^3 \right] \quad (5-23)$$

In order to minimize the amplitude of the stator currents, the four contributions in the right hand of (5-23) must be in phase, leading to

$$\bar{i}_{SA} = 4 K_A \bar{i}_{S1} \quad (5-24)$$

$$\bar{i}_{SB} = 4 K_B \bar{i}_{S1} \bar{\alpha}^{-1} \quad (5-25)$$

$$\bar{i}_{SC} = 4 K_C \bar{i}_{S1} \bar{\alpha}^{-2} \quad (5-26)$$

$$\bar{i}_{SD} = 4 K_D \bar{i}_{S1} \bar{\alpha}^{-3} \quad (5-27)$$

where K_A , K_B , K_C and K_D are the current sharing coefficients, which must satisfy the following constraint:

$$K_A + K_B + K_C + K_D = 1 \quad (5-28)$$

Taking the transformations (5-20) - (5-22), and (5-24) - (5-27) into account, leads to the following relationships:

$$\bar{i}_{S5} = (K_A + jK_B - K_C - jK_D) \bar{i}_{S1}^* \quad (5-29)$$

$$\bar{i}_{S7} = (K_A + jK_B - K_C - jK_D) \bar{i}_{S1} \quad (5-30)$$

$$\bar{i}_{S11} = (K_A - K_B + K_C - K_D) \bar{i}_{S1}^* \quad (5-31)$$

The relationships (5-29) - (5-31), valid in the stationary reference frame, give the instantaneous values of the auxiliary stator current vectors, according to the required current sharing. It should be noted that, in the particular case of $K_A=K_B=K_C=K_D=1/4$, i.e., balanced stator current sharing, all the auxiliary stator current vectors are null. It can be demonstrated that, when the degree of unbalance is small, the current sharing coefficients can be considered as instantaneous power sharing coefficients, with good accuracy.

5.5 CONTROL SCHEME

The block diagram of the control scheme ensuring a decoupled regulation of torque, rotor flux and stator current sharing is emphasized in Figure 5-3.

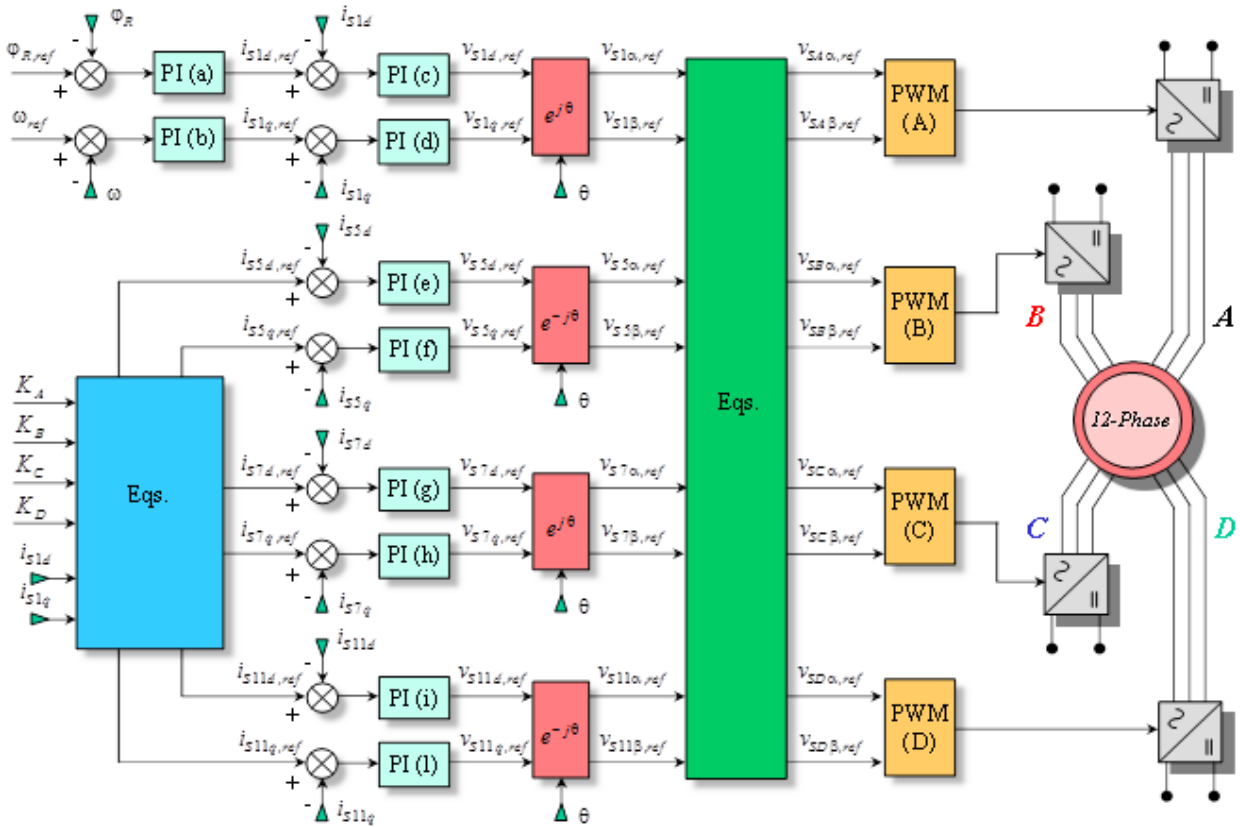


Figure 5-3 - Block diagram of the control scheme

5.5.1 TORQUE AND ROTOR FLUX CONTROL

According to the well-known FOC principle, torque and rotor flux control is achieved by acting on the q and d components of the stator current, in a synchronous reference frame S^+ having the d axis aligned with the rotor flux $\bar{\varphi}_{R1}$. The angle θ is the argument of the estimated rotor flux. The PI current regulators PI(c) and PI(d), which are adopted for the current tracking, calculate the d and q components of the reference voltage vector $\bar{v}_{S1,ref}$, respectively. The corresponding α - β components $v_{S1\alpha,ref}$ and $v_{S1\beta,ref}$ are obtained through an opportune rotation.

5.5.2 AUXILIARY STATOR CURRENT CONTROL

In order to achieve a zero steady-state tracking error, the control of the auxiliary stator current vectors must be

implemented in two different synchronous reference frames, as explained in the following.

Equation (5-30) shows that the current vector \bar{i}_{S7} is proportional to \bar{i}_{S1} , and then, in steady-state conditions, rotates synchronously with $\bar{\varphi}_{R1}$. On the contrary, (5-29) and (5-31) emphasize that the current vectors \bar{i}_{S5} and \bar{i}_{S11} are proportional to \bar{i}_{S1}^* , and then rotate synchronously with $\bar{\varphi}_{R1}^*$. As a consequence, the PI current regulators for \bar{i}_{S7} , PI(g) and PI(h), are implemented in the reference frame S^+ synchronous with $\bar{\varphi}_{R1}$, whereas the PI current regulators for \bar{i}_{S5} and \bar{i}_{S11} , PI(e), PI(f), PI(i) and PI(l), are implemented in the reference frame S^- , which is synchronous with $\bar{\varphi}_{R1}^*$ (see Figure 5-3 - Block diagram of the control scheme). A diagram illustrating the three reference frames involved in the control strategy is shown in Figure 5-3.

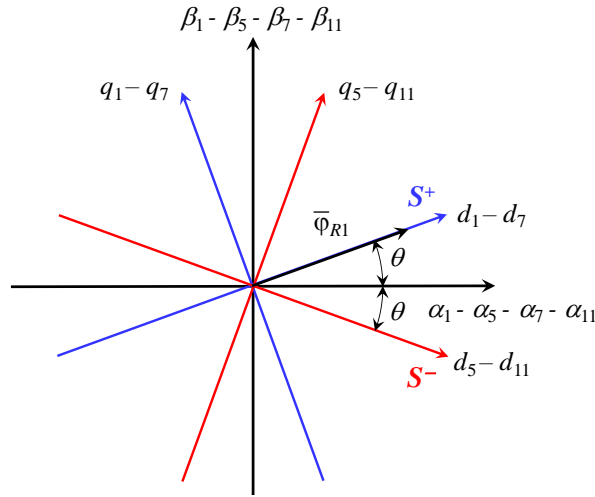


Figure 5-4 - Diagram of the three reference frames involved in the control strategy

Equations (5-29) - (5-31) can be rewritten in the opportune synchronous reference frames, in terms of d-q components, as follows:

$$i_{S5d} = (K_A - K_C) i_{S1d} + (K_B - K_D) i_{S1q} \quad (5-32)$$

$$i_{S5q} = (K_B - K_D) i_{S1d} + (K_C - K_A) i_{S1q} \quad (5-33)$$

$$i_{S7d} = (K_A - K_C) i_{S1d} + (K_D - K_B) i_{S1q} \quad (5-34)$$

$$i_{S7q} = (K_B - K_D) i_{S1d} + (K_A - K_C) i_{S1q} \quad (5-35)$$

$$i_{S11d} = (K_A - K_B + K_C - K_D) i_{S1d} \quad (5-36)$$

$$i_{S11q} = (-K_A + K_B - K_C + K_D) i_{S1q} \quad (5-37)$$

The relationships (5-32) - (5-37) allow determining the reference values of the d-q components of the auxiliary stator current vectors in the block diagram of Figure 5-3. The PI current regulators PI(e)-PI(l), calculate the d and q components of the reference voltage vector $\bar{v}_{S5,ref}$, $\bar{v}_{S7,ref}$, and $\bar{v}_{S11,ref}$. The corresponding α - β components are obtained through an opportune rotation.

5.5.3 MODULATION STRATEGY OF THE FOUR THREE-PHASE

INVERTERS

The modulation strategy of the three-phase VSIs is based on the concept of three-phase decomposition. In other words, the control principle of the quadruple three-phase machine is based on the multiple space vector representation of all the twelve-phase quantities of the stator windings, whereas, on the contrary, the control principle of the inverters exploits the three-phase space vector representation of the three-phase quantities of each three-phase stator winding.

The reference values of the three-phase stator voltage vectors, according with the inverse transformations (5-19) - (5-22), can be obtained as follows

$$\bar{v}_{SA} = \bar{v}_{S1} + \bar{v}_{S5}^* + \bar{v}_{S7} + \bar{v}_{S11}^* \quad (5-38)$$

$$\bar{v}_{SB} = \bar{v}_{S1} \bar{\alpha}^{23} + \bar{v}_{S5}^* \bar{\alpha}^5 + \bar{v}_{S7} \bar{\alpha}^{17} + \bar{v}_{S11}^* \bar{\alpha}^{11} \quad (5-39)$$

$$\bar{v}_{SC} = \bar{v}_{S1} \bar{\alpha}^{22} + \bar{v}_{S5}^* \bar{\alpha}^{10} + \bar{v}_{S7} \bar{\alpha}^{10} + \bar{v}_{S11}^* \bar{\alpha}^{22} \quad (5-40)$$

$$\bar{v}_{SD} = \bar{v}_{S1} \bar{\alpha}^{21} + \bar{v}_{S5}^* \bar{\alpha}^{15} + \bar{v}_{S7} \bar{\alpha}^3 + \bar{v}_{S11}^* \bar{\alpha}^9 \quad (5-41)$$

The well-known modulation strategies for three-phase VSIs (SVM or carrier-based PWM) can be adopted.

5.6 SIMULATION RESULTS

To emphasize the effectiveness of the presented control scheme, some numerical simulations have been carried out using Matlab Simulink™. The parameters of the simulated induction machine are shown in Tab. I. The input DC voltage of the four three-phase VSIs is 215 V, whereas the switching period is 100 μ s. The Space Vector PWM technique is implemented for the control of each three-phase VSI.

The simulated operating condition is described in the following. The induction machine operates at constant speed (3000 rpm) and the rotor flux reference is maintained constant at the rated value (0.092 Wb). The torque reference has a staircase waveform, with the following values: 160 Nm (rated value) from 0.4s to 0.5s, 80Nm from 0.5s to 0.9s, and 120Nm from 0.9s to 1.1s. The values of the current sharing coefficients are $K_A=K_B=K_C=K_D=1/4$ (balanced current sharing) from 0.4 s to 0.7 s, whereas, from 0.7s to 1.1s, they are $K_A=0.325$, $K_B=0.275$, $K_C=0.225$, and $K_D=0.175$.

The simulation results are shown in Figs. 5-10.

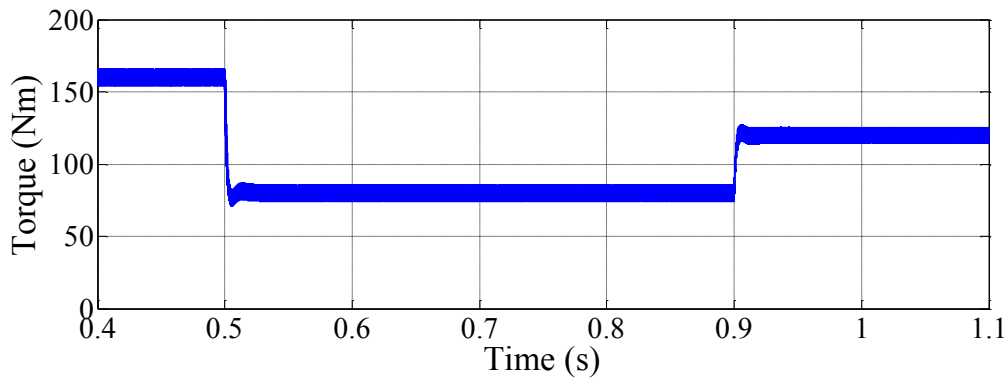


Figure 5-5 - Waveform of the electromagnetic torque

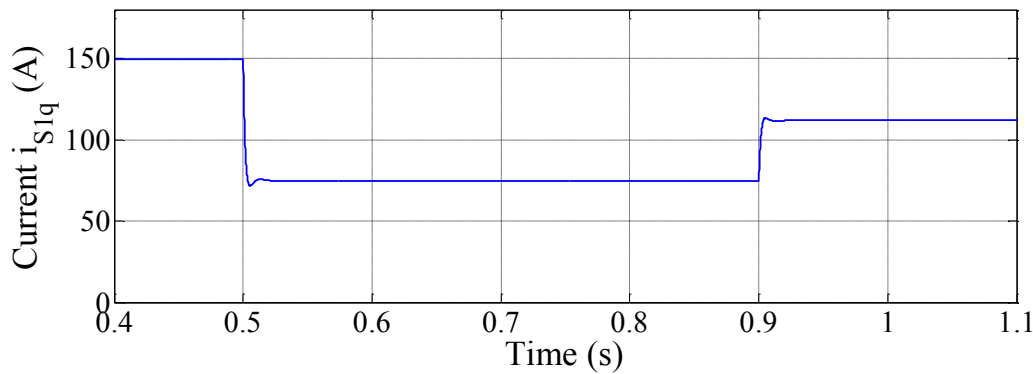


Figure 5-6 - Waveform of the q component of the stator current vector

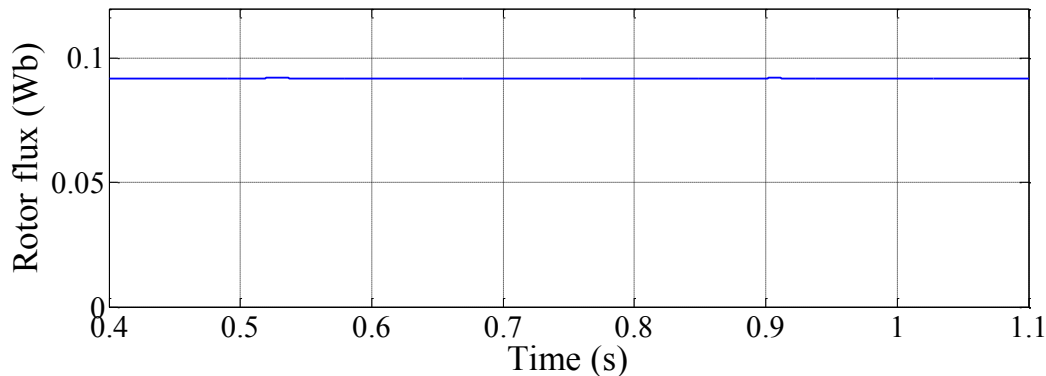


Figure 5-7 - Waveform of the rotor flux magnitude

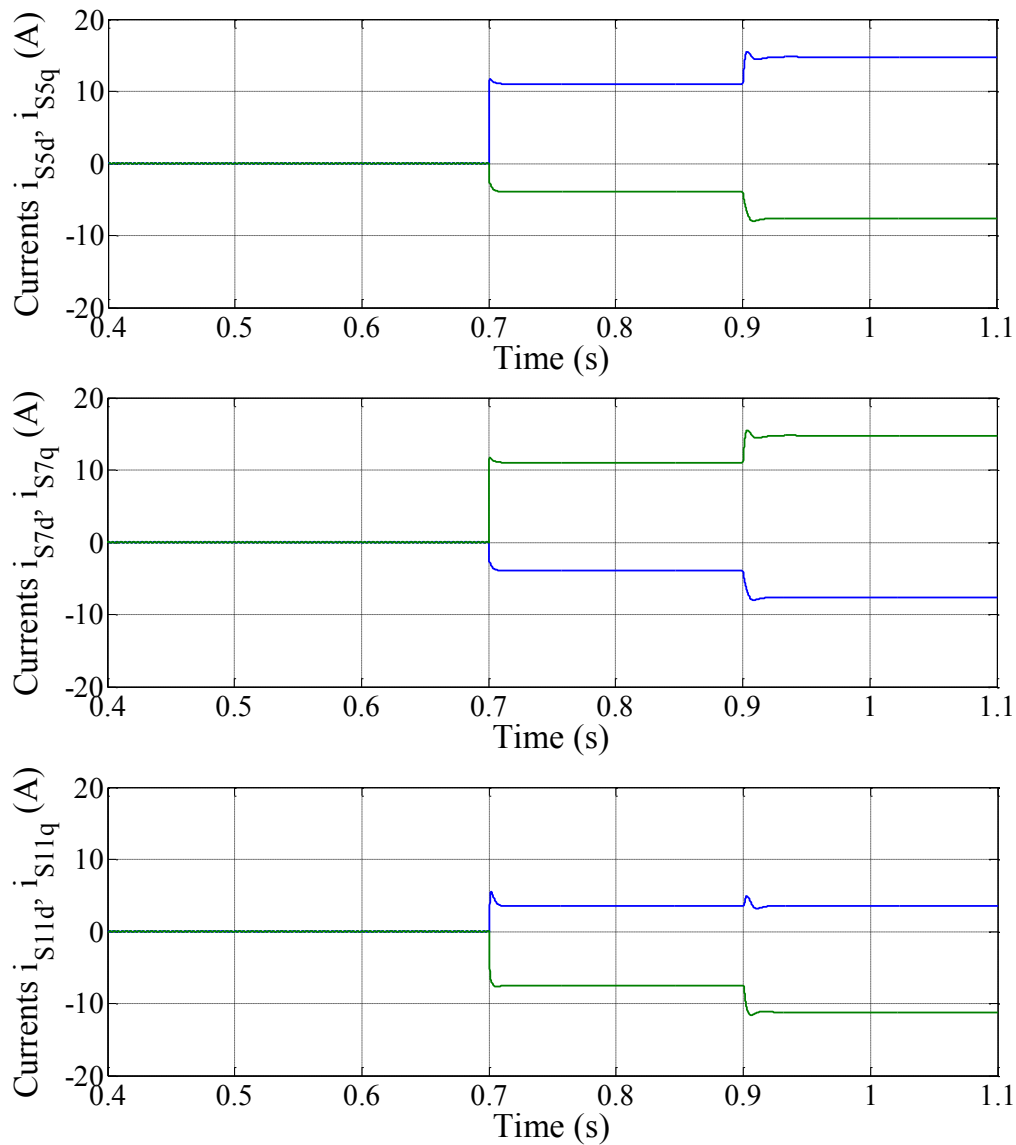


Figure 5-8 - Waveforms of the d-q components of the auxiliary stator currents

The waveform of the torque is illustrated in Figure 5-5, whereas the behaviour of the current i_{s1q} is emphasized in Figure 5-6. They confirm the good behaviour of the torque control in balanced

($t < 0.7s$) as well as unbalanced ($t > 0.7s$) stator current sharing conditions. The high frequency torque ripple is due to the switching effects of the VSIs. As can be seen in Figure 5-7, the rotor flux magnitude matches the reference value. The waveforms of the d-q components of the auxiliary stator currents are shown in Figure 5-8. As expected, in balanced sharing condition all the auxiliary currents are zero. On the contrary, in unbalanced sharing condition, the auxiliary currents assume non-zero values, which depend on i_{s1d} and i_{s1q} , according to eqs. (5-32) - (5-37). The waveforms of the stator currents i_{sA1} , i_{sB1} , i_{sC1} and i_{sD1} (one for each three-phase stator winding) are shown in Figure 5-9. They emphasize the stator current sharing capability of the proposed motor drive. In fact, in balanced sharing condition, the

amplitudes of the currents are the same, whereas, in unbalanced sharing condition, the amplitudes are different, in agreement with the values of the sharing coefficients. The filtered values (time constant $\tau = 500 \mu\text{s}$) of the instantaneous stator power of the four three-phase windings are illustrated in Figure 5-10. These waveforms confirm that the current sharing coefficients can be regarded as power sharing coefficients.

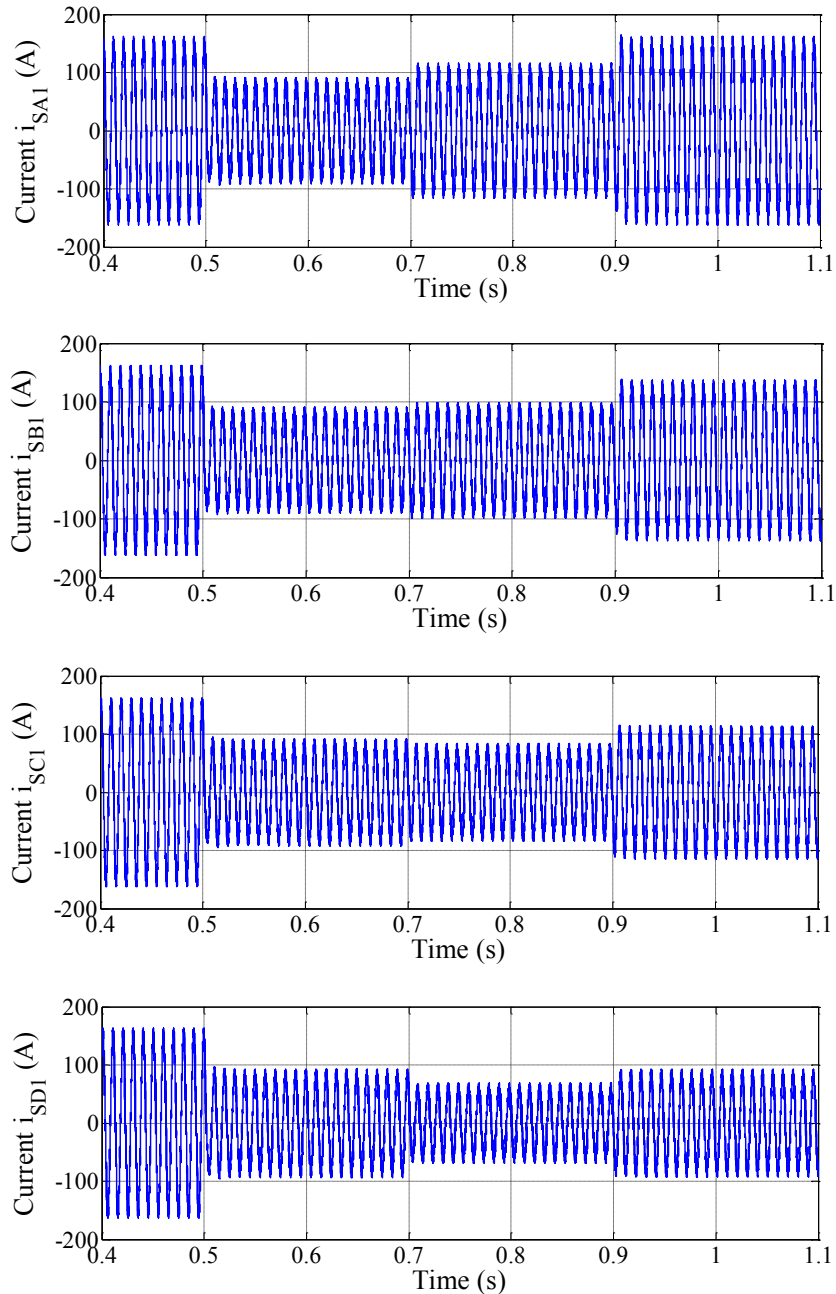


Figure 5-9 - Waveforms of some stator currents. a) Current i_{SA1} , b) current i_{SB1} , c) current i_{SC1} , and d) current i_{SD1} .

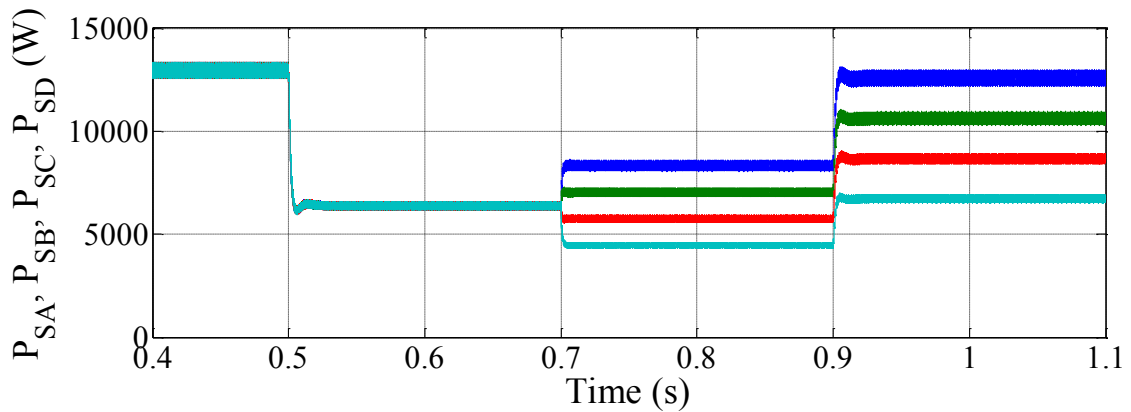


Figure 5-10 - Filtered values (time constant 500us) of the instantaneous stator powers of the four three-phase windings

5.7 CONCLUSION

In this chapter, a motor drive for medium and high power applications, based on a quadruple three-phase induction machine, has been presented. Four two-level VSIs independently supply the three-phase stator windings. The machine model has been achieved by introducing an opportune multiple space vector transformation, suitable for the particular stator winding arrangement. Exploiting the inherent degrees of freedom of the multiphase drive, a current sharing management technique among the four three-phase stator windings has been presented. Since, the current sharing coefficients can be regarded as power sharing coefficients, the proposed control algorithm allows total motor power to be split among the four dc sources, in a flexible way, with three degrees of freedom. The three-phase decomposition method has been employed in order to establish the modulation strategy of the four three-phase VSIs. The stator current sharing capability of the proposed quadruple three-phase induction motor drive has been emphasized by means of simulation results. A system prototype is under development, and some experimental results will be presented in a future work

Chapter 6

A MODULATION STRATEGY FOR MATRIX CONVERTER WITH EXTENDED CONTROL RANGE AND REDUCED SWITCHING POWER LOSSES

6.1 ABSTRACT

This paper is focused on the enhancement of the control range of matrix converters (MCs) operating with non-unity input power factor and, at the same time, on the reduction of the switching power losses. The analysis leads to the determination in closed form of a modulation strategy that features a control range, in terms of output voltage and input power factor, that is greater than that of the traditional strategies under the same operating conditions, and a reduction in the switching power losses. The idea behind the improvement of the modulation strategy is that the control system takes advantage of the information provided by the measurement of load currents, which are usually available in electric drives, and uses a quick algorithm to reduce the number of switch commutations. The feasibility of the proposed strategy is verified by computer simulations and experimental tests.

6.2 INTRODUCTION

The performance of MCs is strictly related to the adopted modulation strategy. Several modulation strategies, based on different mathematical approaches, have been presented in the past [39]. Each of them shows different features in terms of number of switch commutations in a switching period or degree of utilization of the input voltage. Alesina and Venturini proposed the

principles of MC modulation in the early 1980's [40]. The original theory limited the voltage transfer ratio to 0.5, but it was showed later that, by means of third harmonic injection techniques, the maximum voltage transfer ratio could be raised to 0.866, a value which is considered an intrinsic limitation of three-phase MC with balanced supply voltages [41].

Probably, the most used modulation strategy for MCs is the Space Vector Modulation (SVM), since it is particularly suitable for digital implementation, provides adequate exploitation of the input voltage and good load current quality. Basically, two methods for the implementation of SVM for MCs are used. The first one, presented in [42], is also defined "indirect method", because the MC is described as a virtual two stage system, namely a 3-phase rectifier and a 3-phase inverter connected together through a fictitious DC-link. The indirect approach was developed in such a way to allow the control of the input power factor, to fully utilize the input voltages and to improve the modulation performance [43], [44]. The indirect approach has the advantage of simplicity, since it applies the well-established SVM for Voltage Source Inverters (VSIs) to MCs.

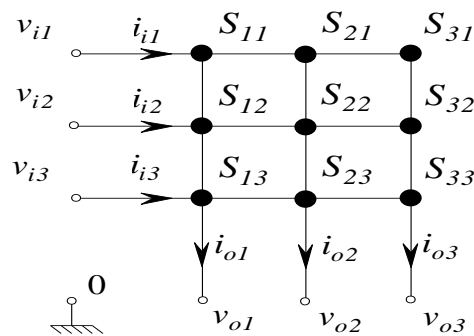


Figure 6-1 - Basic scheme of matrix converters

The second approach to SVM for MCs was presented in [45]. This algorithm is based on the instantaneous representation of input and output voltages and currents as space vectors. It analyses all the switching configurations that are available in three-phase MCs and does not need the concept of a virtual DC link.

For completeness, it is worth noting that in recent years many other control methods have been proposed, such as the carrier-based modulation [46], the modulation scheme based on a predictive quality function [47], and the one based on predictive control [48], which focuses directly on the improvement of quality indexes rather than on the modulation problem.

A general solution of the control problem of matrix converters is presented in [49]. This solution is based on the representation of the switch states by means of space vectors, originally referred to as Duty-Cycle Space Vectors (DCSVs). This method

results from a rigorous approach and can be extended to more complex cases, as shown in [50], which analyses the control of a four-leg matrix converter. In addition, it has the advantage to emphasize all the parameters that affect the performance of the modulation strategy and can be freely chosen. These degrees of freedom have been used to reduce the number of commutations in each switching period or the power losses [51] [52] [53] [54] [55] [56], to improve the voltage quality [57], or to extend the operating region [58] [59] [60] [61] [62] [63]. The reduction of the power losses and the improvement of the control range are both topics addressed by the present paper, which extends the results presented in [64].

A recent paper has analysed in details the modulation range of matrix converters by using an innovative approach based on the singular value decomposition (SVD) of the matrix of the switch duty-cycles [65]. It is shown that there exist two reference frames in which the analysis of the modulation range may be reasonably simplified provided that two different voltage transfer ratios, ρ_d and ρ_q , are introduced for the output voltage. Another interesting contribution is the one reported in [66], which focuses on extending the reactive power control range of all matrix converter topologies by adopting an indirect modulation referred to as hybrid modulation.

Nevertheless, as far as the authors are informed, no paper has already analyzed the possibility to extend the control range and minimize the converter losses at the same time. Some experimental results confirm the validity of the theoretical analysis.

6.3 A REVIEW OF THE MODULATION STRATEGY FOR MATRIX CONVERTERS

The input-output relationships of a matrix converter can be written in the following form [49]:

$$\bar{v}_o = \frac{3}{2} \bar{v}_i \bar{m}_i^* + \frac{3}{2} \bar{v}_i^* \bar{m}_d \quad (6-1)$$

$$\bar{v}_o = \frac{3}{2} \bar{v}_i \bar{m}_i^* + \frac{3}{2} \bar{v}_i^* \bar{m}_d \quad (6-2)$$

where \bar{v}_i and \bar{v}_o are the input and output voltage vectors, \bar{i}_i and \bar{i}_o are the input and output current vectors, the complex variables \bar{m}_d , \bar{m}_i are functions of the state of the switches, and "*" is the complex conjugate operator.

If the desired phase angle of the input current space vector is denoted by the unity vector $\bar{\psi}_{ref}$, and $\bar{v}_{o,ref}$ is the desired output voltage vector, it is possible to demonstrate that \bar{m}_d and \bar{m}_i have the following expressions:

$$\bar{m}_d = \frac{\bar{v}_{o,ref} \bar{\psi}_{ref}}{3(\bar{v}_i \cdot \bar{\psi}_{ref})} + \frac{\lambda}{\bar{v}_i^* \bar{i}_o^*} \quad (6-3)$$

$$\bar{m}_i = \frac{\bar{v}_{o,ref}^* \bar{\psi}_{ref}}{3(\bar{v}_i \cdot \bar{\psi}_{ref})} - \frac{\lambda}{\bar{v}_i^* \bar{i}_o^*} \quad (6-4)$$

where λ is a real number, and " \cdot " is the dot-product operator, defined as the real part of the product between the first operand and the complex conjugate of the second.

Once \bar{m}_d , \bar{m}_i are known, it possible to calculate the following variables, usually known in literature as "Duty-Cycle Space Vectors":

$$\bar{m}_k = \bar{m}_d e^{-\frac{2\pi}{3}(k-1)} + \bar{m}_i e^{\frac{2\pi}{3}(k-1)} + \bar{m}_0 \quad (k=1, 2, 3) \quad (6-5)$$

where \bar{m}_0 is a complex variable, usually referred to as "zero sequence component", that can be freely chosen.

The importance of \bar{m}_1 , \bar{m}_2 and \bar{m}_3 is in that they allow an immediate calculation of the switch duty-cycles. In fact, the duty-cycle $m_{h,k}$ of the switch $S_{h,k}$ of the converter in Fig. 1 can be determined as follows:

$$m_{h,k} = \frac{1}{3} + \bar{m}_h \cdot e^{j\frac{2\pi}{3}(k-1)} \quad (h, k=1,2,3). \quad (6-6)$$

The quantities λ and \bar{m}_0 yield three degrees of freedom that can be used to define any modulation strategy. The general solution given in (3)-(6) includes all the known modulation strategies as particular cases.

Substituting (5) in (6) leads to a very compact expression of the duty-cycles,

$$m_{h,k} = m_{0,k} + A_{h,k} \quad (6-7)$$

where the quantities $m_{0,k}$ and $A_{h,k}$ are scalar quantities defined as follows:

$$m_{0,k} = \frac{1}{3} + \bar{m}_0 \cdot e^{j\frac{2\pi}{3}(k-1)} \quad (k=1,2,3) \quad (6-8)$$

$$A_{h,k} = \left(\bar{m}_d e^{-j\frac{2\pi}{3}(h-1)} + \bar{m}_i e^{j\frac{2\pi}{3}(h-1)} \right) \cdot e^{j\frac{2\pi}{3}(k-1)} \quad (h, k=1,2,3). \quad (6-9)$$

The quantities $m_{0,k}$ can be considered as the components of the space vector \bar{m}_0 and it can be easily verified that their sum is equal to 1:

$$\sum_{k=1}^3 m_{0,k} = 1 \quad (6-10)$$

The constraint (10) means that that the sum of the duty-cycles of the h th output phase, i.e., $m_{h,1}$, $m_{h,2}$, $m_{h,3}$, has to be one, according to the well-known requirement to avoid short circuits at the input side of the converter and switch over voltages due to sudden output current interruption.

The quantities $A_{h,k}$ depend only on the reference output voltage, on the desired angle of the input current vector and on the parameter λ , but do not depend on \bar{m}_0 .

In order to obtain a feasible modulation law, it is necessary that all the duty-cycles are bounded between 0 and 1. Taking (7) into account, one obtains the following constraints:

$$0 \leq m_{0,k} + A_{h,k} \leq 1 \quad (h, k=1,2,3). \quad (6-11)$$

An equivalent formulation of (11) is as follows:

$$-\min_{h=1,2,3} \{A_{h,k}\} \leq m_{0,k} \leq 1 - \max_{h=1,2,3} \{A_{h,k}\} \quad (k=1,2,3). \quad (6-12)$$

The inequalities (12) are very useful to define the operating range of matrix converters and will be used in the optimization of the switching losses.

6.4 EXTENSION OF THE OPERATING RANGE

The parameter λ in (3)-(4) can be utilized to improve the converter performance only if the phase angle of \bar{i}_o is known in each cycle period, otherwise it should be set equal to zero. Although in power converters the output currents are usually measured, the traditional modulation strategies for matrix converter do not use this information and assume $\lambda = 0$, thus obtaining the following expressions for \bar{m}_d and \bar{m}_i :

$$\bar{m}_d = \frac{\bar{v}_{o,ref}}{3\bar{v}_i^*} [1 - j \tan(\varphi_i)] \quad (6-13)$$

$$\bar{m}_i = \frac{\bar{v}_{o,ref}^*}{3\bar{v}_i^*} [1 - j \tan(\varphi_i)] \quad (6-14)$$

where φ_i is the phase lag of the input current.

The vast majority of the modulation strategies are referable to (13) and (14), but make different choices for \bar{m}_0 or differ from each other simply in the switching sequence. It is possible to demonstrate that adopting (13) and (14) leads to the well-known upper bound of the voltage transfer ratio ρ (defined as the ratio between the magnitudes of the desired output voltage vector and input voltage vector):

$$\rho \leq \frac{\sqrt{3}}{2} \cos \varphi_i \quad (6-15)$$

However, recently some papers have shown that the use of the parameter λ can be used to extend the control range.

Provided that the phase lag φ_0 of the load current vector is known (it can be calculated by measuring the load currents), a possible choice for λ is the following one:

$$\lambda = -\frac{1}{3} \tan \varphi_i \sin \varphi_o v_{o,ref} \bar{i}_o \quad (6-16)$$

so that the expressions of \bar{m}_d and \bar{m}_i become

$$\bar{m}_d = \frac{\bar{v}_{o,ref}}{3\bar{v}_i^*} [1 - j \tan(\varphi_i) \cos(\varphi_o) e^{-j\varphi_o}] \quad (6-17)$$

$$\bar{m}_i = \frac{\bar{v}_{o,ref}^*}{3\bar{v}_i^*} [1 - j \tan(\varphi_i) \cos(\varphi_o) e^{j\varphi_o}] \quad (6-18)$$

As a result, it is shown in [64] that an upper bound of the voltage transfer ratio less strict than (15) can be found

$$\rho \leq \min\{f_1(\varphi_i, \varphi_o), f_2(\varphi_i, \varphi_o)\} = \rho_{\max}(\varphi_i, \varphi_o) \quad (6-19)$$

where f_1 and f_2 are dimensionless functions of φ_i and φ_o defined as follows:

$$f_1(\varphi_i, \varphi_o) = \frac{\sqrt{3}}{2} \frac{\cos \varphi_i}{\sqrt{1 - \sin^2 \varphi_i \sin^2 \varphi_o}} \quad (6-20)$$

$$f_2(\varphi_i, \varphi_o) = \frac{1}{\sqrt{1 + (\tan \varphi_i \cos \varphi_o)^2 + |\tan \varphi_i \sin 2\varphi_o|}} \quad (6-21)$$

The behaviour of the functions f_1 and f_2 and of the resulting voltage transfer ratio is shown in Figs. 2 and 3 for φ_o equal to 30 and 60 degrees. As can be seen, when φ_o is small, f_1 leads to an upper bound that is very similar to the traditional one, expressed by (15). However, under the assumption that the input power factor is not unity, as long as the load phase angle increases, the improvement in the voltage transfer ratio becomes sensible. Finally, no improvement is possible when the input current is kept in phase with the input voltage, i.e., $\varphi_i=0$. In this case the limit value of 0.866 for the voltage transfer ratio is insuperable in linear operation.

6.5 OPTIMIZATION OF THE SWITCHING LOSSES

If the constraint (12) is satisfied, the matrix converter can operate in the linear modulation range and the modulation problem has feasible solutions, i.e., there is at least one value of the zero sequence component \bar{m}_0 for which all duty-cycles are in the interval $[0,1]$. However, the choice of \bar{m}_0 is not trivial, and is not unique. In this paper the choice of \bar{m}_0 is based on the optimization of the switching losses.

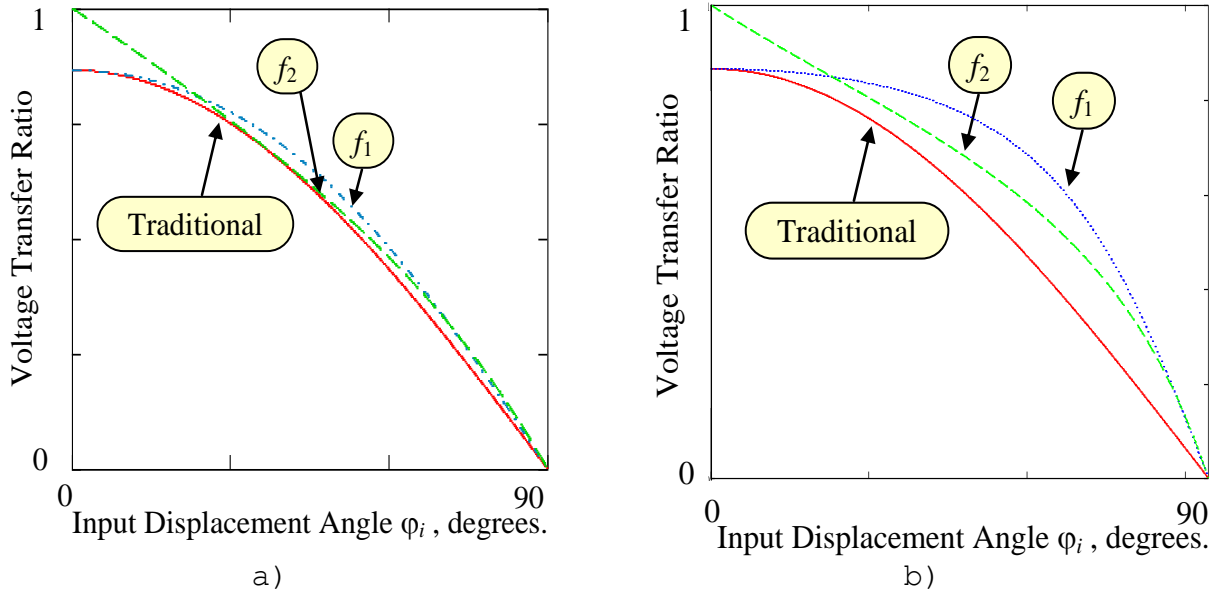


Figure 6-2 - Comparison between the traditional limit value of the voltage transfer ratio and the behaviour of the functions f_1 and f_2 . a) $\varphi_0 = 30deg$, b) $\varphi_0 = 60deg$

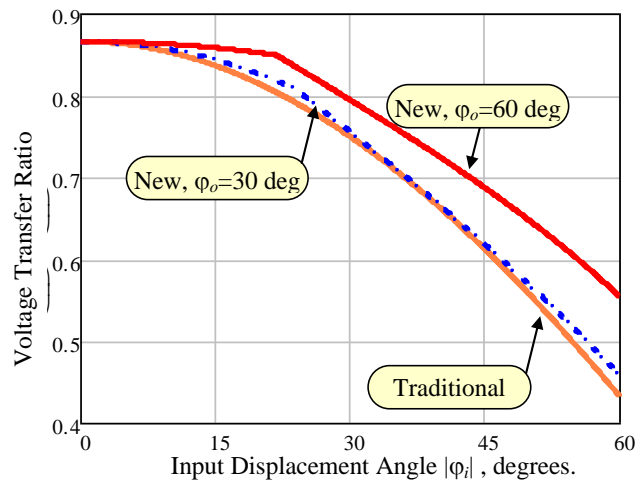


Figure 6-3 - Behaviour of the voltage transfer ratio when the load power factor is 0.86 ($\varphi_0 = 30deg$) and 0.5 ($\varphi_0 = 60deg$)

6.5.1 SWITCHING LOSSES

The switching losses of the matrix converter depend on the switching pattern, i.e., the turn-on and turn-off order of the switches in each phase. Let us suppose that, in a switching period, the h th output phase is respectively connected to the input phases with voltages v_{i,k_1} , v_{i,k_2} and v_{i,k_3} (in this order), and the indexes (k_1, k_2, k_3) are a permutation of $(1, 2, 3)$. If the switching pattern is symmetric, the sequence is repeated inversely in the second half of the period. The corresponding switching losses can be written as follows [53]:

$$P_{SW,h} = 2f_{sw}(\tau_{on} + \tau_{off} + \tau_{rec})|i_{o,h}|x(|v_{i,k_1} - v_{i,k_2}| + |v_{i,k_2} - v_{i,k_3}|) \quad (6-22)$$

where f_{sw} is the switching frequency, τ_{on} and τ_{off} are coefficients (with the dimension of time) related to the energy loss process in the IGBTs during turn-on and turn-off, τ_{rec} is a coefficient (with the dimension of time) related to the energy loss process in the diodes due to the reverse recovery currents during turn-off, $i_{o,h}$ is the output current of the h th phase.

The switching pattern that minimizes the switching losses is intuitively the one that connects the output phase to the input phases in descending order of voltage amplitude, i.e., during each switching period, the output phase is firstly connected to the input phase with the greatest voltage, than to the one with the intermediate voltage, and finally to the one with the lowest voltage (similarly, the ascending order can be used instead of the descending one).

$$v_{i,k_1} \geq v_{i,k_2} \geq v_{i,k_3} \quad (6-23)$$

Under (23), (22) becomes

$$P_{SW,h} = 2f_{sw}(\tau_{on} + \tau_{off} + \tau_{rec})|i_{o,h}||v_{i,k_1} - v_{i,k_3}| \quad (6-24)$$

Suitable values of $m_{0,k}$ may be chosen to reduce the switching losses by cancelling up to two commutations of the switching pattern. However, by analysing (24), one comes to the following conclusions:

a) cancelling the duty-cycle m_{h,k_1} reduces the voltage gap in (24) from $|v_{i,k_1} - v_{i,k_3}|$ to $|v_{i,k_2} - v_{i,k_3}|$ and consequently reduces the switching losses. Similarly, cancelling the duty-cycle m_{h,k_3} reduces the voltage gap from $|v_{i,k_1} - v_{i,k_3}|$ to $|v_{i,k_1} - v_{i,k_2}|$;

b) cancelling only the duty-cycle m_{h,k_2} does not affect the switching losses, because the total voltage gap $|v_{i,k_1} - v_{i,k_3}|$ does not change;

c) if a duty-cycle among m_{h,k_1} , m_{h,k_2} and m_{h,k_3} is set to 1, the remaining duty-cycles are necessarily zero. Then the switching losses of the h th phase becomes zero.

In conclusion, it is possible to rewrite (24) in the following form:

$$P_{SW,h} = 2f_{sw}(\tau_{on} + \tau_{off} + \tau_{rec})|i_{o,h}|(|v_{i,k_1} - v_{i,k_2}| \varepsilon(m_{h,k_1}) + |v_{i,k_2} - v_{i,k_3}| \varepsilon(m_{h,k_3})) \quad (6-25)$$

TABLE I - INSPECTED CONFIGURATIONS

Case	Zero-Sequence	Cancelled commutations	Avoided switching losses
1	$m_{0,k_1} = -A_{h'_m,k_1}$ $m_{0,k_3} = -A_{h''_m,k_3}$	$m_{h'_m,k_1} = 0$ $m_{h''_m,k_3} = 0$	$P_{saved} = W'_{h'_m} + W''_{h''_m}$
2	$m_{0,k_1} = 1 - A_{h'_M,k_1}$ $m_{0,k_3} = -A_{h'_M,k_3}$	$m_{h'_M,k_1} = 1$ $m_{h'_M,k_3} = 0$	$P_{saved} = W'_{h'_M} + W''_{h'_M}$
3	$m_{0,k_1} = -A_{h''_M,k_1}$ $m_{0,k_3} = 1 - A_{h''_M,k_3}$	$m_{h''_M,k_1} = 0$ $m_{h''_M,k_3} = 1$	$P_{saved} = W'_{h''_M} + W''_{h''_M}$

where

$$\varepsilon(m_{h,k}) = \begin{cases} 0 & \text{if } m_{h,k} = 0 \text{ or } m_{h,k} = 1 \\ 1 & \text{otherwise} \end{cases} \quad (6-26)$$

In general terms, if the switching order is the same for all the output phases, the switching losses of the whole converter in a switching period can be written as follows:

$$P_{SW,tot} = \sum_{h=1}^3 P_{SW,h} = \sum_{h=1}^3 [W'_h \varepsilon(m_{h,k_1}) + W''_h \varepsilon(m_{h,k_3})] \quad (6-27)$$

Where

$$W'_h = 2f_{sw} (\tau_{on} + \tau_{off} + \tau_{rec}) i_{o,h} (v_{i,k_1} - v_{i,k_2}) \quad (6-28)$$

$$W''_h = 2f_{sw} (\tau_{on} + \tau_{off} + \tau_{rec}) i_{o,h} (v_{i,k_2} - v_{i,k_3}) \quad (6-29)$$

Equation (27) shows that the switching losses of the converter can be written as a linear combination of the loss coefficients W'_h and W''_h . The 6 variables $\varepsilon(m_{h,k_1})$ and $\varepsilon(m_{h,k_3})$ ($h=1,2,3$) are normally set to 1. However, a suitable choice of \bar{m}_0 may drive two duty-cycles of the matrix converter to zero, and consequently two coefficients among $\varepsilon(m_{h,k_1})$ and $\varepsilon(m_{h,k_3})$ may potentially be cancelled.

A brute-force algorithm for the minimization of the switching losses should check 15 cases (combinations of 6 elements, 2 at a time). However, an algorithm that reduces to three the number of cases that should be inspected has been developed. The cases that have to be checked are those shown in Tab. I. Among them, the control algorithm should choose the one leading to the minimum switching losses. Before applying the algorithm, it is necessary to find the indexes h'_m, h'_M, h''_m, h''_M that identify the minimum and the maximum values among A_{h,k_1} and A_{h,k_3} ($h=1,2,3$), as shown hereafter:

$$A_{h'_M, k_1} = \max_{h=1,2,3} A_{h, k_1} \quad (6-30)$$

$$A_{h'_m, k_1} = \min_{h=1,2,3} A_{h, k_1} \quad (6-31)$$

$$A_{h'_M, k_3} = \max_{h=1,2,3} A_{h, k_3} \quad (6-32)$$

$$A_{h'_m, k_3} = \min_{h=1,2,3} A_{h, k_3} \quad (6-33)$$

The second column of Tab. I shows the value of the zero-sequence components m_{0, k_1} and m_{0, k_3} for each case. The remaining component m_{0, k_2} can be found from (10) as

$$m_{0, k_2} = 1 - m_{0, k_1} - m_{0, k_3} \quad (6-34)$$

The third column of Tab. I shows which duty-cycles are set to 0 or to 1 for each case. Finally the last column shows the amount of switching losses that can be avoided.

Once the zero-sequence signals $m_{0, k}$ ($k=1, 2, 3$) have been calculated from Tab. I and (34), it is possible to reconstruct the vector \bar{m}_0 as follows:

$$\bar{m}_0 = \frac{2}{3} \sum_{k=1}^3 m_{0, k} e^{j \frac{2\pi}{3} (k-1)} \quad (6-35)$$

and to calculate the duty-cycles of the converter by means of (5)-(6). However, there is no certainty that they result in the range $[0, 1]$. A necessary condition for this to happen is that (12) is verified. Then the output voltage is synthesizable and at least one of the three cases of Tab. I leads to admissible duty-cycles.

In essence, the three cases of Tab. I are as follows:

- a) two duty-cycles of switches in different output legs can be cancelled (case 1);
- b) two duty-cycles of the switches in the same output leg can be cancelled. Consequently the duty-cycle of the remaining switch of the same output leg is equal to 1 (case 2 and 3).

6.6 SIMULATION RESULT

Some simulations have been carried out to verify the feasibility of the proposed modulation strategy. With reference to the basic scheme of Figure 6-4, where the variables are expressed as space vectors, the parameters used for the computer simulations

are shown in Table II. The switching frequency is 8 kHz, corresponding to a period of the switching pattern of 125 μ s.

Figure 6-5 shows the behaviour of the matrix converter when the output delay angle is 60 degrees, the input delay angle is ± 30 degrees and the voltage transfer ratio is 0.79 (which cannot be achieved by the conventional modulation strategies). The bottom traces in both figures show the waveforms of the duty-cycles $m_{1,1}$, $m_{1,2}$ and $m_{1,3}$. As can be seen, the output and input currents are sinusoidal, although the duty-cycles are discontinuous in an unpredictable way. Each time one of the nine duty-cycles is zero, it means that the corresponding switch does not commutate. If it is one, the corresponding switch stays turned on during the entire switching period.

The comparison of the modulation strategies in terms of switching losses has been carried out by using PLECS. The evaluation of the power losses has been done under the assumption that the power module FM35R12KE3, produced by Infineon-Eupec, is used. Figure 6-6 shows the turn-on and turn-off energy loss of an IGBT and the recovery energy loss of a diode when the voltage applied to the switches is 600 V and the junction temperature is 125°C, whereas Figure 6-7 shows the output characteristic of an IGBT and a diode.

Figure 6-8 shows the power losses of all the modulation strategies, divided into switching and total losses when the voltage transfer ratio is the maximum according to (15). It turns out that the proposed modulation strategy shows losses which are considerable lower than the SVM with three zero vectors (SVM3z), the SVM with two zero vectors (SVM2z), and the SVM with one zero vector (SVM1z). SVM2z uses the zero vectors that are not in the middle of the double-sided switching pattern, whereas SVM1z uses the zero vectors at the beginning and at the end of the double-sided switching pattern.

In the examined operating conditions the reduction in the switching losses varies from 10% to 32% in comparison to those of SVM1z.

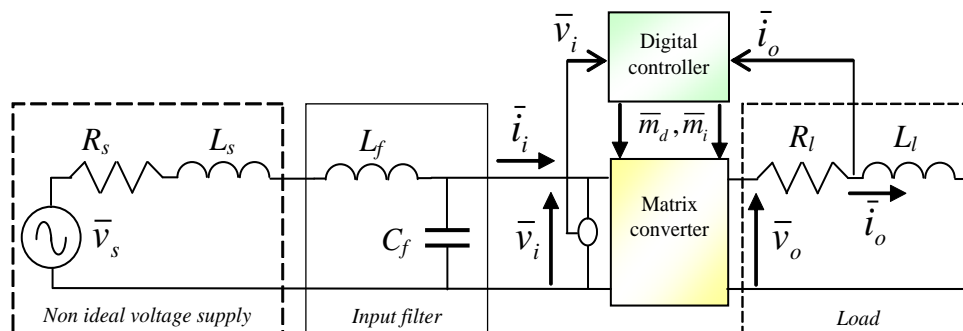


Figure 6-4 - Schematic diagram of the system based on matrix converter

TABLE II - SIMULATION PARAMETERS

Supply	Filter	Load
$V_i = 220 V_{LL,rms}$	$L_f = 1.1 \text{ mH}$	$R_l = 6.5 \Omega$
$\omega_s = 2\pi 50 \text{ rad/s}$	$C_f = 25 \mu\text{F (Y)}$	$L_l = 0.030 \text{ mH}$
$R_s = 0.2 \Omega$		$\omega_o = 2\pi 60 \text{ rad/s}$
$L_s = 0.80 \text{ mH}$		

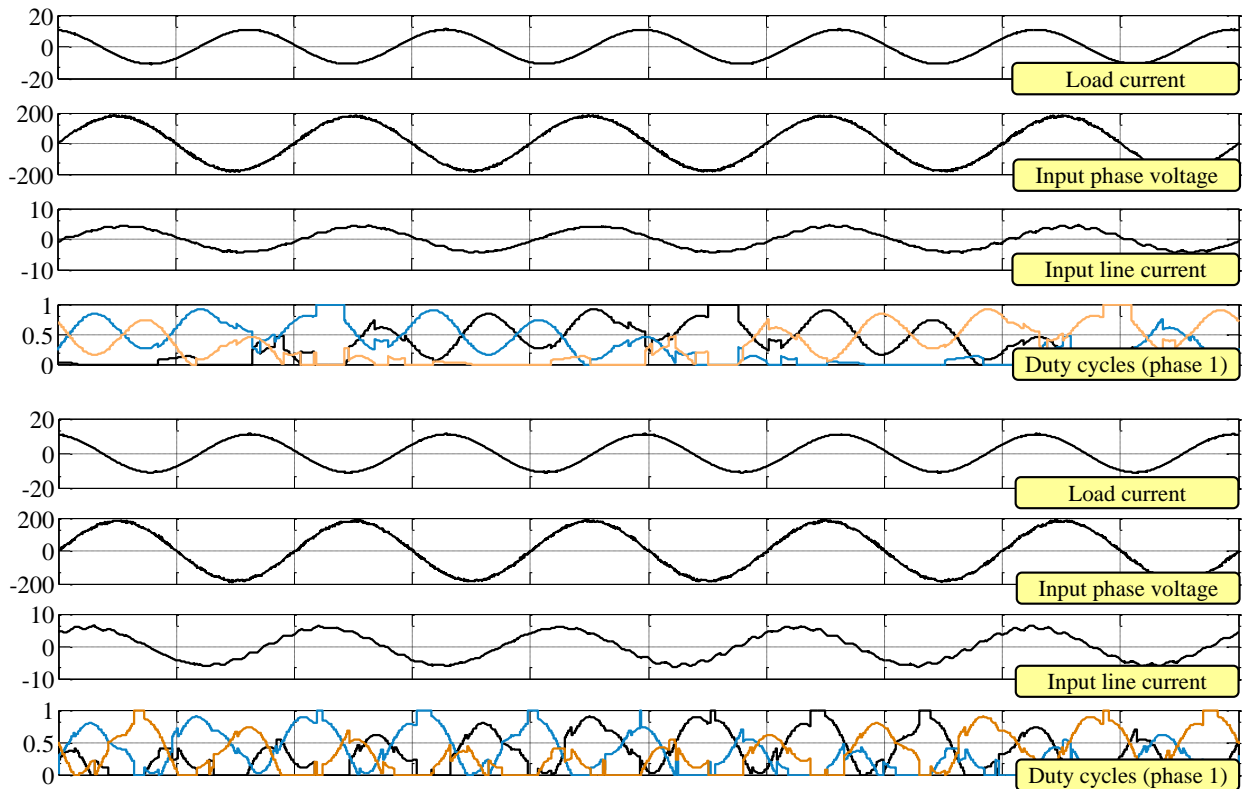


Figure 6-5 - Behavior of the matrix converter for $\phi_o=60 \text{ deg.}$ when $\phi = 0.79$. Time scale: 10 ms/div. a) $\phi_i=30 \text{ deg.}$ b) $\phi_i= -30 \text{ deg}$

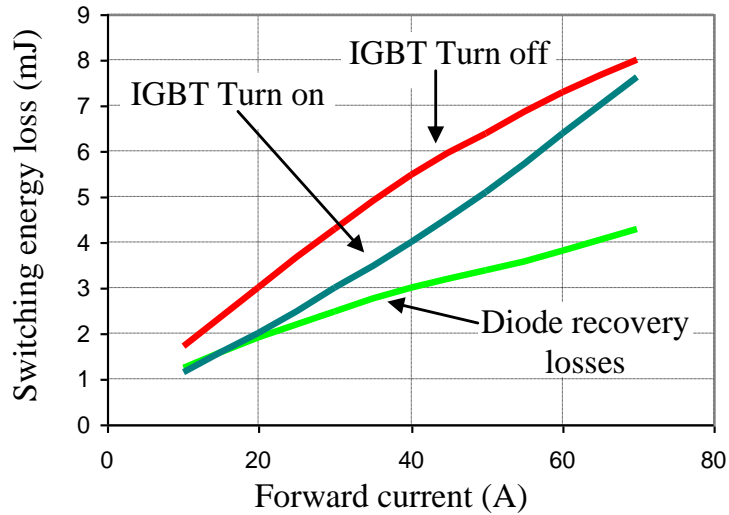


Figure 6-6 - Switching losses of an IGBT and a diode of the model used for the computer simulations, when the final voltage after turn-on and the initial voltage before turn-off is 600 V, and the junction temperature is 125°C

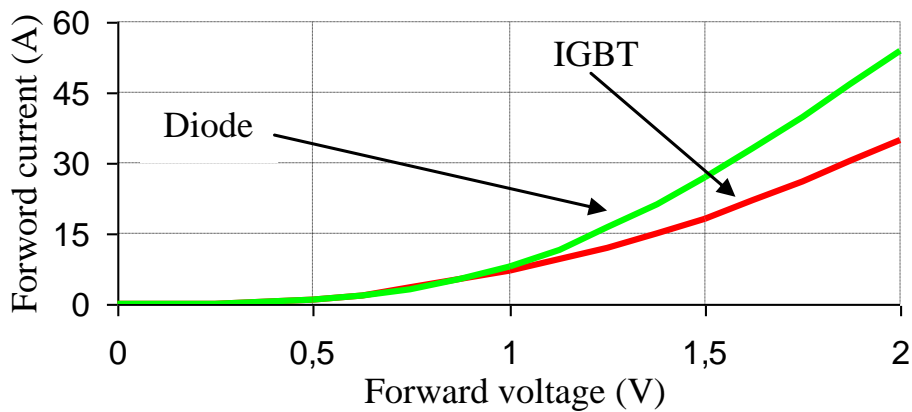


Figure 6-7 - Output characteristic of an IGBT and a diode of the model used for the computer simulations, when the junction temperature is 125°C

6.7 EXPERIMENTAL RESULT

A prototype of three-phase to three-phase MC has been used to verify the feasibility of the proposed modulation strategy. The basic scheme of the experimental setup is the same of Figure 6-4. The MC is built by using the FM35E12KR3 IGBT module produced by Infineon-Eupec. The control algorithm is implemented on a fixed-point digital signal processor by Texas Instruments (model TMSF2812). The switching frequency of the modulation strategy is 8 kHz and the well-known four-step commutation is used.

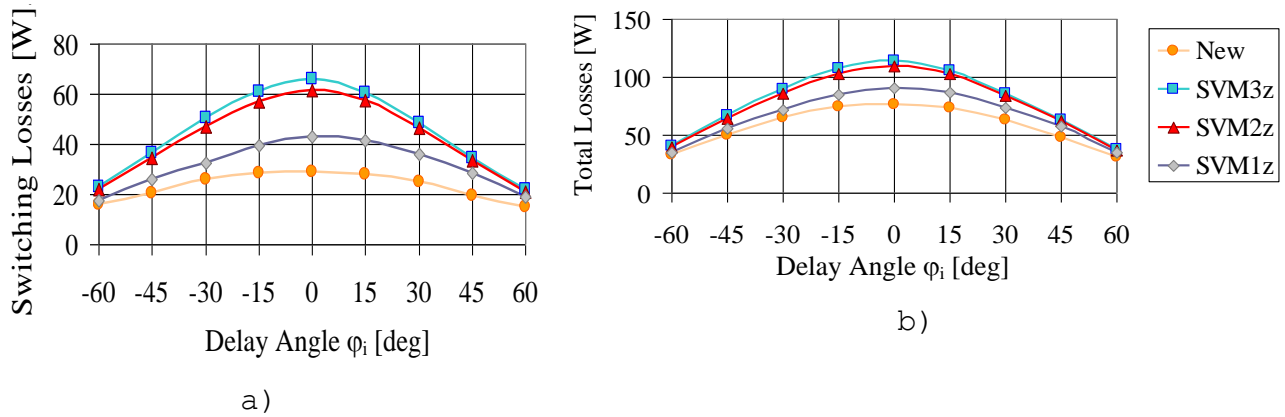


Figure 6-8 - Simulation results. Power losses for different modulation strategies as a function of the input delay angle ϕ_i . The load power factor is assumed equal to 0.5 and the voltage transfer ratio is calculated according to (15). (a) Switching losses. (b) Total losses

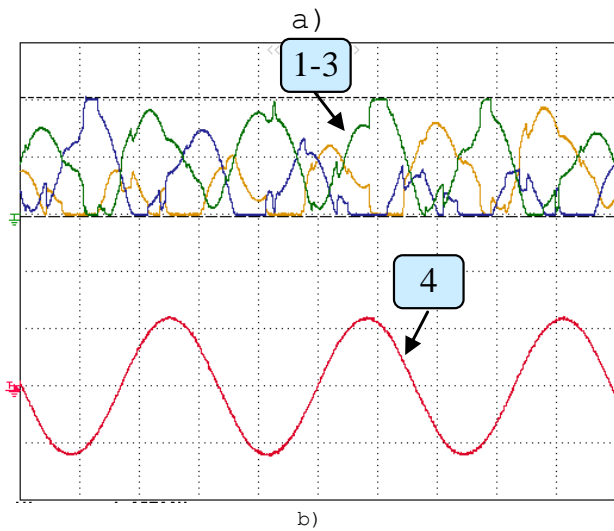
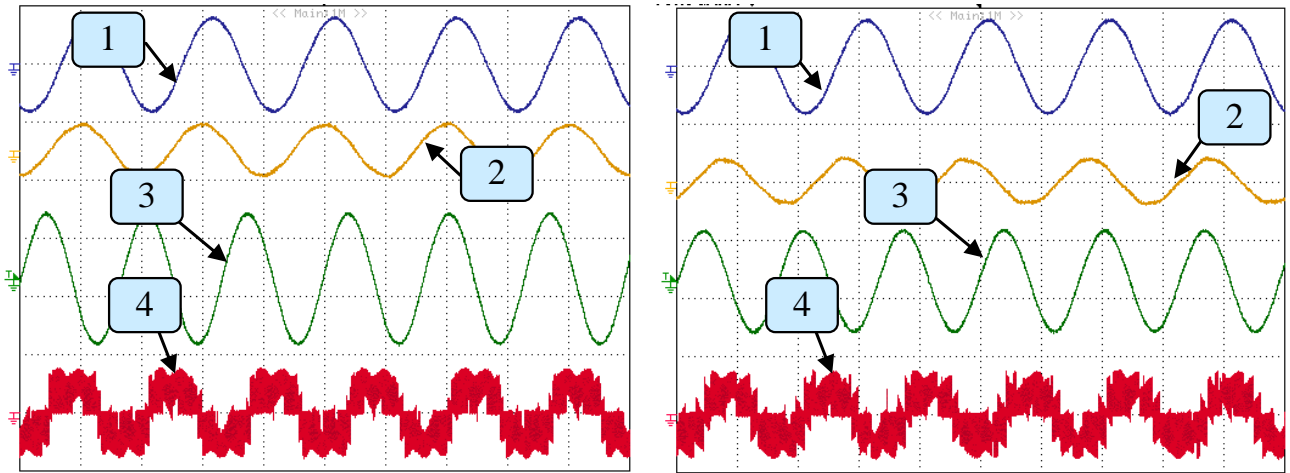


Figure 6-9 a) - Behaviour of the matrix converter for $\varphi_i = -30$ deg, $\varphi_o = 60$ deg. when ρ is 0.78. (1) Input line-to-neutral voltage (200 V/div). (2) Filtered input current (10 A/div). (3) Load current (10A/div). (4) Output line-to-line voltage (400 V/div).

Figure 6-10 b) - Behaviour of the matrix converter for $\varphi_i = -30$ deg, $\varphi_o = 60$ deg when ρ is 0.78. (1)-(3) Duty-cycles $m_{1,1}$, $m_{1,2}$, $m_{1,3}$. (4) Load current (10A/div).

Figure 6-11 c) - Behaviour of the matrix converter for $\varphi_i = -60$ deg, $\varphi_o = 60$ deg. when ρ is 0.54. (1) Input line-to-neutral voltage (200 V/div). (2) Filtered input current (10 A/div). (3) Load current (10A/div). (4) Output line-to-line voltage (400 V/div).

Figure 6-12 - Behaviour of the matrix converter for $\varphi_i = -60$ deg, $\varphi_o = 60$ deg when ρ is 0.54. (1)-(3) Duty-cycles $m_{1,1}$, $m_{1,2}$, $m_{1,3}$. (4) Load current (10A/div).

Figure 6-9 and Figure 6-10 show the behaviour of the matrix converter when the input displacement angle is -30° (the converter absorbs capacitive reactive power and acts as a power factor corrector) and the load delay angle is 60° , corresponding to a fundamental input power factor of 0.86 (capacitive) and a fundamental output power factor of 0.5. The voltage transfer ratio in Figs. 9 and 10 has been increased up to 0.78, which is greater than the limit given by (15), i.e., 0.74.

Figure 6-11 and Figure 6-12 show the behaviour of the converter in the same operating conditions, except for the input displacement angle, which is equal to -60° . The voltage transfer ratio of Figs. 11 and 12 is equal to 0.54, which is 25% greater than the traditional limit, 0.43.

In all figures, the behavior of the converter is satisfactory. The input and output quantities are almost sinusoidal and the duty-cycles are clamped in the interval $[0,1]$. As can be seen, the duty-cycles are frequently equal to 0 or to 1, which confirms the cancellation of some commutations.

6.8 CONCLUSION

In this chapter a modulation strategy that simultaneously improves the control range of matrix converter and reduces the switching losses is proposed.

The theoretical analysis shows that the zero-sequence component \bar{m}_0 can be used to minimize the power losses, whereas the remaining degree of freedom λ can be used to extend the control range of the converter.

Compared to the traditional SVM, the proposed modulation strategy is able to obtain higher voltage transfer ratios under the assumption that the desired power factor at the input and at the output of the converter is not unity.

As a result, the switching losses can be sensibly reduced compared to traditional modulation strategies. The simulation results, performed under the assumption that the load power factor is 0.5, show reductions in the switching losses up to 32% compared to SVM1z.

Chapter 7

MODULATION STRATEGY WITH MINIMUM SWITCHING LOSSES FOR THREE-PHASE AC-DC MATRIX CONVERTERS

7.1 ABSTRACT

Passive three-phase rectifier circuits are very popular for ac-dc power conversion. However, they do not have the capability to reverse the power flow, which is demanded by some recent potential smart-grid applications, such as vehicle-to-grid (V2G) power transfer.

As an alternative, this paper analyses the behaviour of three-phase ac-dc matrix converters. Among the modulation strategies that minimize the switching losses, the one leading to the minimum output current ripple is chosen. The behaviour of this modulation strategy is experimentally tested.

7.2 INTRODUCTION

Interconnection of power electronics to the grid has been performed for a long time by using passive three-phase rectifier circuits in combination with inductors located either on the ac or on the dc-side. These rectifier circuits are simple, show a high efficiency and are very robust, but result in a total harmonic distortion of the input currents (THDi) of typically 30-50% and show a considerably small power factor. In addition, they cannot allow a bidirectional power flow, and therefore they are not suitable for emerging applications, such as vehicle-to-grid (V2G) power exchange or smart grid applications [67] [68].

Due to upcoming standards containing rigorous input current harmonic limits, in many cases passive rectifiers cannot be used any more. Three-phase pulse width-modulated (PWM) voltage- and

current-source rectifiers (VSRs and CSRs) have consequently emerged [69]. Active three-phase PWM rectifiers offer unity power factor, a THDi below 5% and a high power density. These converters are typically used as active front-end to the grid, and their dc-link voltage is necessarily greater than the phase-to-phase input voltage, so they do not seem particularly suitable to feed low voltage loads, such as batteries, because they require an additional intermediate step-down power stage.

A converter topology that has not been deeply investigated as bi-directional active front end is the three-phase ac-dc matrix converter [70]. Its ability of supplying compensating leading or lagging input currents in a wide operating range makes it a strong candidate for potential applications in plug-in automotive, aircraft, ship and other three-phase powered standby dc supplies.

The international research has recently focused also on many converter topologies based on bidirectional power switches. An indirect ac-ac converter topology was proposed in [71], [72], where a current-source rectifier is directly connected in cascade to a two-level voltage source inverter, without using any intermediate energy storage element. This technology has obtained much attention in the ac-ac power conversion field in recent years [73], [74] and [75]. Other topologies can be derived from the indirect matrix converter topologies [76] [77], such as the sparse, the very sparse and ultrasparse matrix converter. These topologies have a reduced number of input switches but the same functionality of the standard indirect matrix converter. The ultrasparse matrix converter is the simplest one and consists of only nine electronics switches and 18 diodes [78].

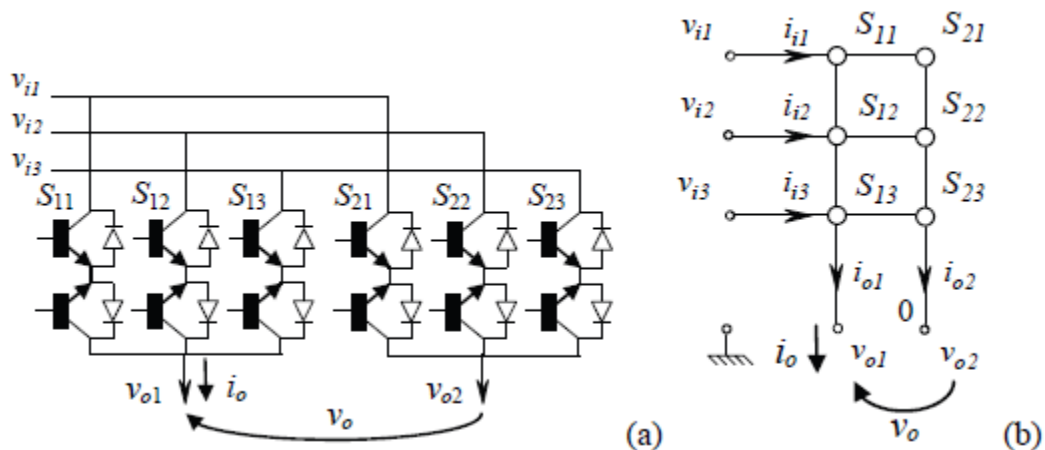


Figure 7-1 - Basic scheme of a three-phase ac-dc matrix converter. (a) Converter structure. (b) Simplified matrix representation.

The technology of matrix converter has been applied to ac-dc conversion with interesting results in [79] [80] [81] [82].

In this paper, the three-phase ac-dc direct matrix converter topology is analysed and the modulation strategies leading to the minimum converter losses are found. Finally, among them, the one producing the minimum output current ripple is identified as the best choice. This work can be considered as the prosecution of similar analyses carried out for direct, indirect and sparse matrix converters [76], [83] [84] [85] [86] [87] [88].

The feasibility and the performance of the proposed modulation strategy are confirmed by numerical simulation and experimental results.

7.3 MODULATION STRATEGY FOR AC/DC MATRIX CONVERTERS

The performance of matrix converters is strictly related to the adopted modulation strategy. Several modulation strategies, based on different mathematical approaches, have been presented in the past for traditional direct three-phase MCs [89]. Each of them shows different features in terms of number of switch commutations in a switching period or degree of utilization of the input voltage. Probably, the most used modulation strategy for MCs is the Space Vector Modulation (SVM), since it is particular suitable for digital implementation, provides adequate exploitation of the input voltage and good load current quality [45]. A general solution of the control problem of three-phase direct ac/ac matrix converters is presented in [49]. This solution is based on the representation of the switch states by means of space vectors, originally referred to as Duty-Cycle Space Vectors (DCSVs). This method results from a rigorous approach and it has the advantage to emphasize all the parameters that affect the performance of the modulation strategy and can be freely chosen. In addition it can be extended to more complex cases, as shown in [90], which analyses the control of a four-leg matrix converter. In the following, the same method will be adapted for the analysis of ac/dc matrix converters.

7.3.1 INPUT OUTPUT EQUATIONS OF THE AC/DC MATRIX CONVERTERS

With reference to Fig. 1, the expression of the output voltage v_o is as follows:

$$v_o = v_{o1} - v_{o2} = \sum_{k=1}^3 (m_{1,k} - m_{2,k}) v_{i,k} \quad (7-1)$$

where $v_{i,k}$ ($k=1,2,3$) are the input voltages and $m_{h,k}$ ($h=1,2$ and $k=1,2,3$) are the duty-cycles of the switches $S_{h,k}$.

Since the converter does not include elements that can store energy, if the converter power losses are neglected, the input power is equal to the output power, i.e.,

$$\sum_{k=1}^3 i_{i,k} v_{i,k} = v_o i_o = \sum_{k=1}^3 (m_{1,k} - m_{2,k}) v_{i,k} i_o \quad (7-2)$$

where i_o is the output current.

Equation (2) is verified for any value of $v_{i,k}$, so it is possible to conclude that the input currents are

$$i_{i,k} = (m_{1,k} - m_{2,k}) i_o \quad (7-3)$$

The duty-cycles $m_{1,k}$ and $m_{2,k}$ have to satisfy the usual constraints

$$\sum_{k=1}^3 m_{h,k} = 1 \quad h = 1,2 \quad (7-4)$$

which prevent short-circuits and over-voltages.

7.3.2 INPUT-OUTPUT EQUATIONS IN TERMS OF SPACE

VECTORS

The input equation voltages and current can be written in terms of space vectors \bar{v}_i and \bar{i}_i whose components are

$$v_{i,k} = \bar{v}_i \cdot \bar{\alpha}_k \quad (7-5)$$

$$i_{i,k} = \bar{i}_i \cdot \bar{\alpha}_k \quad (7-6)$$

where "." is the dot product, defined as the real part of the product between the first operand and the complex conjugate of the second operand, and

$$\bar{\alpha}_k = e^{j\frac{2\pi}{3}(k-1)} \quad (7-7)$$

The state of the converter legs can be represented by two complex numbers m_1 , m_2 defined as follows:

$$\bar{m}_k = \frac{2}{3} \sum_{k=1,2,3} m_{h,k} \bar{\alpha}_k \quad (7-8)$$

Replacing (5) and (6) in (1) and (3), and considering (8), the input-output equations of a three-phase ac-dc matrix converter can be written in terms of m_1 and m_2 as follows:

$$\bar{v}_o = \frac{3}{2} v_i (\bar{m}_1 - \bar{m}_2) \quad (7-9)$$

$$\bar{i}_i = i_o (\bar{m}_1 - \bar{m}_2) \quad (7-10)$$

Two new variables m_d and m_0 can be introduced to simplify the mathematical formulation of (9) and (10):

$$\bar{m}_d = \bar{m}_1 - \bar{m}_2 \quad (7-11)$$

$$\bar{m}_0 = \frac{\bar{m}_1 + \bar{m}_2}{2} \quad (7-12)$$

As a result, the input and output relationships of the converter become

$$v_o = \frac{3}{2} \bar{v}_i \cdot \bar{m}_d \quad (7-13)$$

$$\bar{i}_i = i_o \bar{m}_d \quad (7-14)$$

If the desired phase angle of the input current space vector is denoted by the unity vector ψ_{ref} and $v_{o,ref}$ is desired output voltage, by solving (13) and (14), it is possible to prove that m_d has the following expression

$$\bar{m}_d = \frac{2 v_{o,ref} \overline{\psi_{ref}}}{3 \bar{v}_i \cdot \overline{\psi_{ref}}} \quad (7-15)$$

Whereas \bar{m}_0 , usually referred to as "zero-sequence component", can be freely chosen to improve the performance of the modulation strategy.

Once \bar{m}_d has been calculated from (15), it is possible to find m_1 and m_2 by inverting (11)-(12):

$$\bar{m}_h = (-1)^{h-1} \frac{\bar{m}_d}{2} + \bar{m}_0 \quad (7-16)$$

The quantity m_0 is equivalent to two degrees of freedom that can be used to define any modulation strategy. The importance of m_1 and m_2 is in that they allow calculating the switch duty-cycles. In fact, the duty-cycles $m_{h,k}$, can be found by solving the set of equations (4) and (8), which give the following result:

$$\bar{m}_{h,k} = \frac{1}{3} + \bar{m}_h \cdot \bar{\alpha}_k \quad h = 1,2, \quad k = 1,2,3 \quad (7-17)$$

The general solution given in (15)-(17) includes all modulation strategies as particular cases.

7.3.3 CONTROL RANGE OF THE OUTPUT VOLTAGE

The duty-cycles are bounded between 0 and 1, i.e.,

$$0 \leq m_{h,k} \leq 1 \quad h = 1,2 \quad k = 1,2,3 \quad (7-18)$$

By considering (16) and (17), (18) can be rewritten as follows

$$0 \leq \frac{(-1)^{h-1}}{2} \bar{m}_d \cdot \bar{\alpha}_k + m_{0,k} \leq 1 \quad (7-19)$$

Where

$$m_{0,k} = \frac{1}{3} + \bar{m}_0 \cdot \bar{\alpha}_k \quad k = 1,2,3 \quad (7-20)$$

Equations (20) reveal that the quantities $m_{0,k}$ ($k=1,2,3$) can be regarded as the components of the vector \bar{m}_0 , i.e., \bar{m}_0 can be expressed as

$$\bar{m}_0 = \frac{2}{3} \sum m_{0,k} \alpha_k \quad (7-21)$$

And the sum of $m_{0,k}$ ($k=1,2,3$) is 1.

Inequalities (19) can be rewritten in such a way as to emphasize the upper and lower bounds of $m_{0,k}$.

$$-\frac{(-1)^{h-1}}{2} \bar{m}_d \cdot \bar{\alpha}_k \leq m_{0,k} \leq 1 - \frac{(-1)^{h-1}}{2} \bar{m}_d \cdot \bar{\alpha}_k \quad h = 1,2. \quad (7-22)$$

The dependence on the index h in (22) can be removed by writing the inequalities as follows:

$$\max_{h=1,2} \left\{ -\frac{(-1)^{h-1}}{2} \bar{m}_d \cdot \bar{\alpha}_k \right\} \leq m_{0,k} \leq \min_{h=1,2} \left\{ 1 - \frac{(-1)^{h-1}}{2} \bar{m}_d \cdot \bar{\alpha}_k \right\} \quad (7-23)$$

In the worst case, (23) shows that the upper and lower bounds for $m_{0,k}$ are

$$\frac{1}{2} |\bar{m}_d \cdot \bar{\alpha}_k| \leq m_{0,k} \leq 1 - \frac{1}{2} |\bar{m}_d \cdot \bar{\alpha}_k| \quad k = 1,2,3 \quad (7-24)$$

Since the upper bound of $m_{0,k}$ must be greater or equal to the lower bound, from (24) one finds the following constraint for \bar{m}_d :

$$|\bar{m}_d \cdot \bar{\alpha}_k| \leq 1 \quad k = 1,2,3 \quad (7-25)$$

Substituting (15) in (25) leads to the following result:

$$\left| \frac{2}{3} v_{o,ref} \frac{\bar{\Psi}_{ref} \cdot \bar{\alpha}_k}{\bar{v}_i \cdot \bar{\Psi}_{ref}} \right| \leq 1 \quad k = 1,2,3 \quad (7-26)$$

From (26) it is possible to verify that, in the worst case, i.e., when $\bar{\Psi}_{ref}$ is aligned with one of the vectors $\bar{\alpha}_k$ ($k=1,2,3$), the maximum voltage transfer ratio is as follows:

$$\frac{|v_{o,ref}|}{|\bar{v}_i|} \leq \frac{3}{2} \cos \varphi_i \quad (7-27)$$

where ϕ_i is the displacement angle between the input voltage vector and the input current vector.

If the constraint (27) is satisfied, the ac-dc matrix converter can operate in the linear modulation range and the modulation problem has feasible solutions. This means that there is at least one value of the zero sequence component \bar{m}_0 that makes all duty-cycles remain in the interval $[0,1]$. The optimal choice of \bar{m}_0 is not trivial and is discussed in the next section.

7.4 IMPROVEMENT IN THE SWITCHING LOSSES AND OUTPUT CURRENT RIPPLE

7.4.1 GENERAL EXPRESSION OF THE SWITCHING LOSSES

The values of the duty-cycles (17) of the switches are not sufficient to univocally identify a modulation strategy, because it is still possible to choose different switching sequences, i.e., different turn-on and turn-off ordering of the switches.

In this paper it is assumed that the same switching pattern is used for both output phases and that during a switching period each output phase is connected to the input phases in a specific order, depending on the amplitude of the input voltages. Each output phase is firstly connected to the input phase with the greatest voltage, than to the one with the intermediate voltage, and finally to the one with the lowest voltage (if the switching pattern is symmetric, the sequence is repeated in reverse order in the second half of the period). It is known that this switching pattern is the one that minimizes the switching losses of the converter, although it may be slightly detrimental for the input and output current quality. Let us suppose that the indices of the input voltages in descending order is given by the triplet (k_1, k_2, k_3) ,

$$v_{i,k_1} \geq v_{i,k_2} \geq v_{i,k_3} \quad (7-28)$$

then, if the four-step commutation is used, the switching losses of the converter in a switching period can be expressed as follows:

$$P_{SW,tot} = 2f_{sw}(\tau_{on} + \tau_{off} + \tau_{rec})|i_o| \sum_{h=1}^2 \left(|v_{i,k_1} - v_{i,k_2}| \delta'_h + |v_{i,k_2} - v_{i,k_3}| \delta''_h \right) \quad (7-29)$$

where f_{sw} is the switching frequency, τ_{on} and τ_{off} are coefficients (with the dimension of time) related to the energy loss process in the IGBTs during turn-on and turn-off, τ_{rec} is a coefficient (with

the dimension of time) related to the energy loss process in the diodes due to the reverse recovery currents during turn-off. The coefficient δ'_h is equal to 1 if the h th output voltage commutates between the maximum and the intermediate input voltage in the switching period, or 0 if this transition does not exist. Similarly, the coefficient δ''_h is 1 if the h th output voltage commutates between the intermediate and the minimum input voltage in the switching period. If the modulation strategy does not reduce the switching losses, the four coefficients δ'_h and δ''_h ($h=1,2$) are normally equal to 1, but a suitable choice of \bar{m}_0 may cancel two of them. However the previous analysis shows that, to reduce the switching losses, it is necessary to focus on the switches connected to input phases k_1 and k_3 , whereas those connected to input phase k_2 are not significant.

7.4.2 OPTIMAL ZERO SEQUENCE COMPONENT FOR THE REDUCTION OF THE SWITCHING LOSSES

It is possible to verify that there are only three values of \bar{m}_0 that leads to an effective reduction in the switching losses. The components m_{0,k_1} , m_{0,k_2} and m_{0,k_3} values can be deduced from Table I.

Let us focus on Case 1 of Table I. According to (24), the expression

$$m_{0,k_1} = 1 - \frac{1}{2} |\bar{m}_d \cdot \bar{\alpha}_{k_1}| \quad (7-30)$$

is the upper bound of m_{0,k_1} . Hence, if (30) is verified, one of the two duty-cycles, m_{1,k_1} or m_{2,k_1} , increases up to 1, i.e.,

$$m_{\hat{h},k_1} = 1 \quad (7-31)$$

where \hat{h} is the index of the output phase.

Necessarily, (31) forces the other duty-cycles of the same output leg to be zero. Consequently,

$$m_{\hat{h},k_3} = 0. \quad (7-32)$$

Equation (33) means that m_{0,k_3} is equal to its lower bound, which is

$$m_{0,k_3} = \frac{1}{2} |\bar{m}_d \cdot \bar{\alpha}_{k_3}|. \quad (7-33)$$

The component m_{0,k_2} can be calculated once the values of m_{0,k_1} and m_{0,k_3} are known.

$$m_{0,k_2} = 1 - m_{0,k_1} - m_{0,k_3}. \quad (7-34)$$

Equations (30), (33) and (34) are listed in the first row of Table I, corresponding to Case 1. The table entries of Cases 2 can be found with a similar reasoning.

The components m_{0,k_1} and m_{0,k_3} in Case 3 can be determined under the assumption that they both are set to their lower bounds, so that the duty-cycles of two switches are zero, i.e.,

$$m_{\hat{h},k_1} = m_{\tilde{h},k_3} = 0. \quad (7-35)$$

where \hat{h} and \tilde{h} identify the output phases.

Cases	m_{0,k_1}	m_{0,k_3}	m_{0,k_2}	δ'_h, δ''_h
Case 1	$m_{0,k_1} = 1 - \frac{1}{2} \overline{m}_d \cdot \overline{\alpha}_{k_1} $	$m_{0,k_3} = \frac{1}{2} \overline{m}_d \cdot \overline{\alpha}_{k_3} $	$m_{0,k_2} = 1 - m_{0,k_1} - m_{0,k_3}$	$\delta'_h = \delta''_h = 0$
Case 2	$m_{0,k_1} = \frac{1}{2} \overline{m}_d \cdot \overline{\alpha}_{k_1} $	$m_{0,k_3} = 1 - \frac{1}{2} \overline{m}_d \cdot \overline{\alpha}_{k_3} $	$m_{0,k_2} = 1 - m_{0,k_1} - m_{0,k_3}$	$\delta'_h = \delta''_h = 0$
Case 3	$m_{0,k_1} = \frac{1}{2} \overline{m}_d \cdot \overline{\alpha}_{k_1} $	$m_{0,k_3} = \frac{1}{2} \overline{m}_d \cdot \overline{\alpha}_{k_3} $	$m_{0,k_2} = 1 - m_{0,k_1} - m_{0,k_3}$	$\delta'_h = \delta''_h = 0$

Table 7-1 - Value of the zero-sequence components

Finally, the case when the components m_{0,k_1} and m_{0,k_3} are equal to their upper bounds,

$$m_{0,k_1} = 1 - \frac{1}{2} |\overline{m}_d \cdot \overline{\alpha}_{k_1}| \quad (7-36)$$

$$m_{0,k_3} = 1 - \frac{1}{2} |\overline{m}_d \cdot \overline{\alpha}_{k_3}| \quad (7-37)$$

does not produce feasible values of the duty-cycles and is not considered.

It is worth noting that the expression of m_{0,k_2} deduced from Table I for Case 1 is

$$m_{0,k_2} = \frac{1}{2} \overline{m}_d \cdot (\overline{\alpha}_{k_1} - \overline{\alpha}_{k_3}) \quad (7-38)$$

while for Case 2 it is

$$m_{0,k_2} = \frac{1}{2} \overline{m}_d \cdot (\overline{\alpha}_{k_1} - \overline{\alpha}_{k_3}) \quad (7-39)$$

Since (38) and (39) are opposite to each other, one of them is certainly negative and does not comply with the lower bounds given by (24), which are positive. These means that, among the three cases of Table I, only two of them can provide feasible solutions to the modulation problem.

7.4.3 OPTIMAL EXPRESSION OF THE SWITCHING LOSSES

If in every switching period the zero-sequence component is chosen according to Cases 1, 2 or 3 of Table I, the expression of the total power losses (29) can be simplified because some coefficients among δ'_1 , δ''_1 , δ'_2 and δ''_2 are zero, as shown in the last column of Table I, whereas the remaining coefficients are equal to 1. It turns out that the simplified expression of (29) is independent of the specific Case 1, 2 or 3, and is as follows:

$$P_{SW,tot} = 2f_{sw}(\tau_{on} + \tau_{off} + \tau_{rec})|i_o|(|v_{i,k_1} - v_{i,k_2}| + |v_{i,k_2} - v_{i,k_3}|) = 2f_{sw}(\tau_{on} + \tau_{off} + \tau_{rec})|i_o|(v_{i,k_1} - v_{i,k_3}) \quad (7-40)$$

which means that all Cases theoretically produce the same minimum amount of switching losses. In a fundamental period of the input voltage, the average switching losses of the converter are

$$P_{sw,avr} = \frac{6\sqrt{3}}{\pi}(\tau_{on} + \tau_{off} + \tau_{rec})f_{sw}|\bar{v}_i||i_o| \quad (7-41)$$

Consequently it is not possible to identify an optimal modulation strategy among Cases 1, 2 and 3 without introducing a further quality index. The simplest idea is to choose, among the strategies leading to the minimum switching losses, the one producing the minimum output current ripple.

As shown in the next Section, the numerical simulations suggest that this strategy is the one corresponding to Case 3, which therefore should be preferred to the others.

7.4.4 NUMERICAL SIMULATIONS

Some computer simulations have been performed to assess the behaviour of the modulation strategies corresponding to Cases 1, 2 and 3 of Table I. Fig. 2 shows a schematic of the system in terms of space vectors, and the system parameters are listed in Table II. The switching frequency is 8 kHz.

Fig. 3 shows the behaviour of the converter when the voltage transfer ratio is maximum, i.e., 1.5, and the input power factor is equal to 1. The input currents are sinusoidal and the output current is constant. Case 3 is the optimal choice for the reduction of the switching losses and for the reduction of the output current ripple for the following reasons:

1. the solutions corresponding to Cases 1 and 2 are not always feasible;
2. Case 3 leads to a switching ripple of the load current that is always lower than that resulting from Cases 1 and 2.

Fig. 3 shows the trend of the rms value of the ripple of the

load current for all Cases. The rms value of the current ripple is calculated as follows:

$$\Delta I_{RMS} = \sqrt{\frac{1}{T_{SW}} \int_0^{T_{SW}} \Delta i_o(t)^2 dt} \quad (7-42)$$

where $\Delta i_o(t)$ is the load current ripple, i.e., the difference between the actual load current and its mean value over a switching period T_{SW} . The current ripple $\Delta i_o(t)$ is numerically estimated by solving the following approximated differential equation in each switching period,

$$L_l \frac{d}{dt} \Delta i_o \cong v_o(t) - v_{o,ref} \quad (7-43)$$

under the assumption that the current ripple is zero at the beginning and at the end of the switching period, due to the symmetry of the switching pattern, and $v_o(t)$ changes according to the switching pattern resulting from Cases 1, 2 or 3.

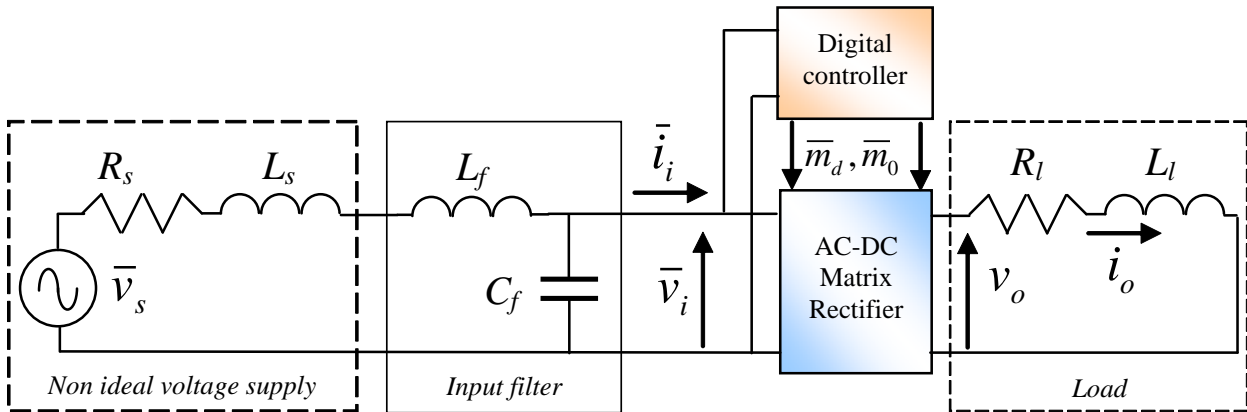


Figure 7-2 - Basic scheme of AC/DC conversion system

Table 7-2 - Simulation Paramters

Supply	Filter	Load
$V_i = 220V_{LLrms}, \omega_s = 2\pi 50 \frac{rad}{s}$ $R_s = 0.2\Omega, L_s = 0.80mH$	$L_f = 1.1mH$ $C_f = 25 \mu F (Y)$	$R_l = 50 \Omega$ $L_l = 0.010 H$

As can be seen from Fig. 3, the rms value of the current ripple corresponding to Case 3 is always the lowest one. The rms value of the current ripple for Cases 1 and Case 2 is alternatively equal to zero, because the corresponding duty-cycles are not admissible.

Fig. 4 shows the behaviour of the converter when the voltage transfer ratio is 0.5. As can be seen, the conclusion remains that Case 3 is the best choice.

Furthermore, Figs. 3 and 4 show the waveform of the duty-cycles

m_{11} , m_{12} and m_{13} . In all cases, the duty-cycles are repeatedly clamped to zero, thus demonstrating that some commutations are avoided. To assess the improvement in the converter efficiency, the PLECS toolbox has been used to model the converter switches, based on the IGBT module FM35E12KR3 produced by Infineon-Eupec.

Fig. 5 compares the power losses of the proposed modulation strategy to those produced by space vector modulation using three equally-spaced zero vectors (SVM3z). As expected, the proposed modulation strategy leads to a consistent reduction (greater than 30%) in the switching losses. Surprisingly, Fig. 6 shows that the THD of the line currents produced by the new modulation strategy is better than that of SVM3z in the whole range of the voltage transfer ratio, whereas the THD of the load current is slightly better for high values of the voltage transfer ratio.

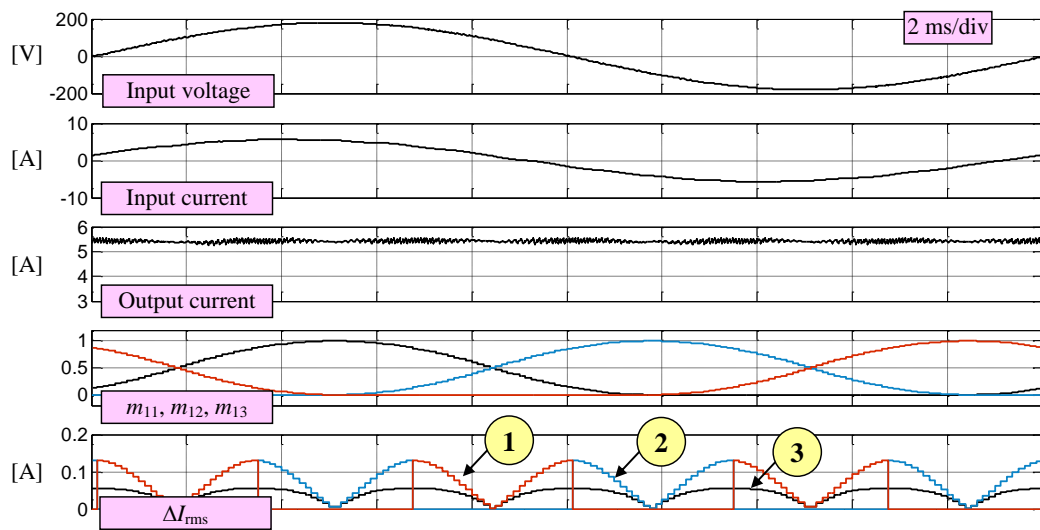


Figure 7-3 - Simulation results. Behaviour of the converter when the voltage transfer ratio is 1.5 and the input power factor is 1.

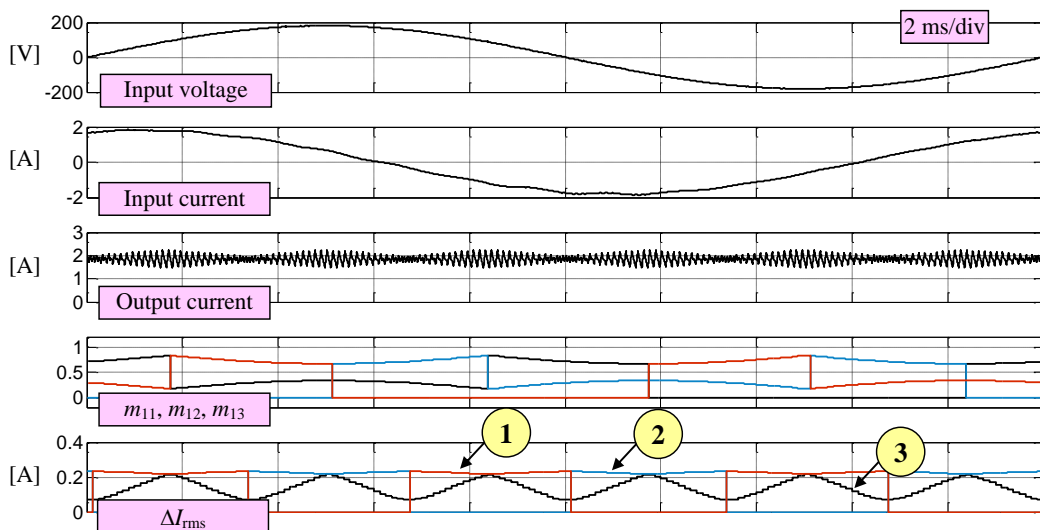


Figure 7-4 - Simulation results. Behavior of the converter when the voltage transfer ratio is 0.5 and the input power factor is 1

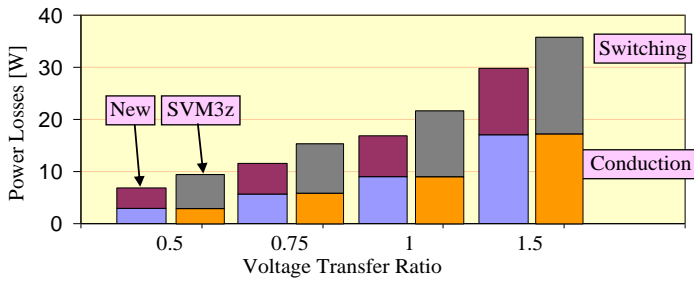


Figure 7-5 - Power losses of the new modulation strategy of the space vector modulation with three zero vectors (SVM3z), when the input power factor is 1.

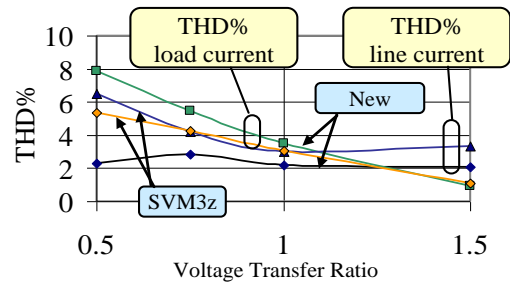
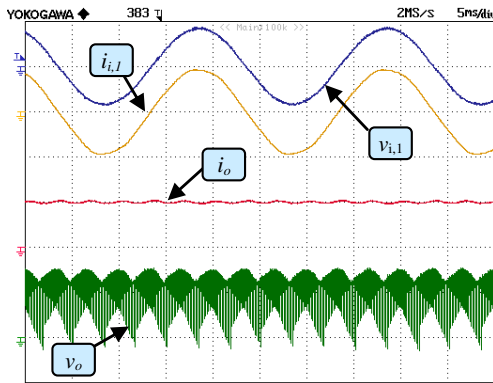
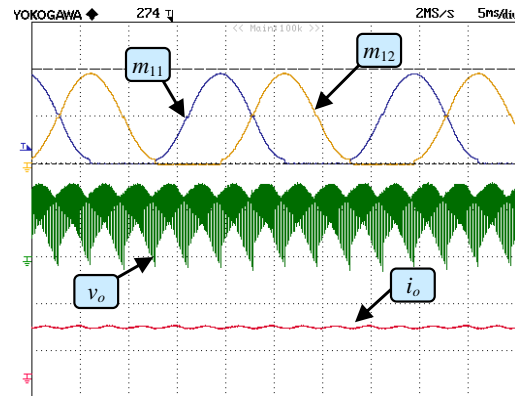


Figure 7-6 - THD of line and load currents for the new modulation strategy and for the space vector modulation with three zero vectors (SVM3z), when the input power factor is 1.

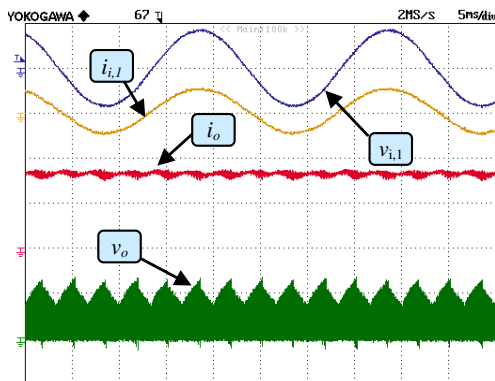


a)

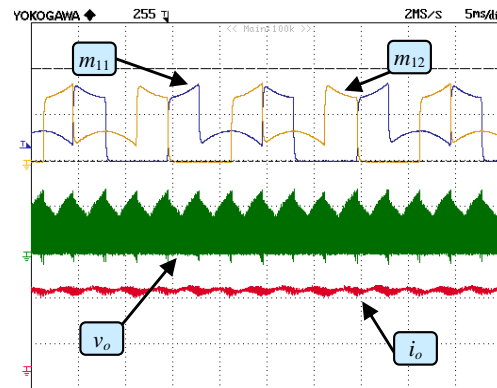


b)

Figure 7-7 - Behaviour of the matrix converter when the input power factor is 1 and the voltage transfer ratio is 1.5. Input voltage (200 V/div). Input current (5 A/div). Load current (5A/div). Output voltage (200 V/div).



a)



b)

Figure 7-8 - Behaviour of the matrix converter when the input power factor is 1 and the voltage transfer ratio is 0.5. Input voltage (200 V/div). Input current (5 A/div). Load current (1A/div). Output voltage (200 V/div).

7.5 EXPERIMENTAL RESULTS

Experimental tests have been carried out to verify the performance of the proposed modulation strategy. The basic scheme of the experimental setup is the same of Fig. 2. The converter is based on the IGBT module FM35E12KR3. The control algorithm is implemented on a fixed-point digital signal processor produced by Texas Instruments (model TMSF2812). The parameters of the system are the same of those shown in Table II, and the four-step commutation is used.

Figs. 7-8 show the behaviour of the converter when the voltage transfer ratio is equal to 1.5 and 0.5. For each operating condition, each figure shows the waveforms of the input line-to-neutral voltage, of the input current (filtered to remove the switching harmonics), of the output voltage and of the output current. As can be seen, the input voltage is practically in phase with the input current, thus confirming that the input power factor is equal to one.

The waveforms of the duty-cycles m_{11} and m_{12} (Fig. 7b and 8b) are in good agreement with the simulation results shown in Figs. 3 and 4. These signals are discontinuous and are repeatedly clamped to zero, thus producing the expected reduction of the switching losses.

7.6 CONCLUSION

This chapter proposes a coherent and exhaustive methodology to analyse the performance of three-phase ac-dc matrix converters. The modulation strategy allowing the minimum switching losses and the minimum output current ripple has been determined. This strategy reduces the switching losses at least by 30% in comparison to the space vector modulation that uses three equally-spaced zero vectors. Some experimental results confirm the feasibility of the proposed technique.

FINAL CONCLUSION

The aim of this thesis, carried out at the LEMAD Laboratory of University of Bologna, is the analysis and design of electrical machines for vehicle and aircraft applications. In particular, during the Ph.D. period I realized two prototype of induction machine (with two different rotor, one in Fe-Si and other rotor in Fe-Co) for aircraft applications and a synchronous machine (PMSM) for automotive application. Moreover, I also realized a drives system to control this electrical machines.

As we have seen, in the previous chapters, the adoption of particular ferromagnetic material such as Fe-Co allows to increase the density torque in the same size. This aspect is absolutely not to be neglected in aircraft application. However, a method to reduce carbon emissions and fuel consumption is presented.

The second part of this dissertation is dedicated to the "matrix converter" and a modulation strategy that simultaneously improves the control range of matrix converter and reduces the switching losses is proposed. Compared to the traditional SVM, the proposed modulation strategy is able to obtain higher voltage transfer ratios under the assumption that the desired power factor at the input and at the output of the converter is not unity. As a result, the switching losses can be sensibly reduced compared to traditional modulation strategies.

LIST OF THE MAIN USED ACRONYMS

AEA	All Electrical Aircraft
APU	Auxiliary Control Unit
BLDC	Brushless Direct Current Motor
CVG	Constant velocity Gearbox
GUI	Graphical User Interface
EBHA	Electrical Backup Hydraulic Actuators
EHA	Electrical Hydraulic Actuator
Fe-Co	Iron Cobalt
Fe-Si	Iron Silicon
FEMM	Finite Element Method Magnetics
GCU	Generator Control Unit
HP	High Pressure
IAP	Integrated Actuator Package
IDF	Integrated Drive Generator
JAA	Joint Aviation Authority
LP	Low Pressure
MEA	More Electric Aircraft
MEE	More Electric Engine
MESA	Magnetostrictive Equipment and System for More electric Aircraft (project)
PMSM	Permanent Magnet Synchronous Machine
POA	Power Optimised Aircraft
RAT	Ram Air Turbine

REFERENCES

- [1] A. Boglietti, A. Cavagnino, A. Tenconi, and S. Vaschetto, "The safety critical electric machines and drives in the more electric aircraft: A survey," in , Porto, Portugal, 2009.
- [2] C. R. W. A. D. K. S.L. Botten, "Flight Control Actuation Technology for Next-Generation All-Electric Aircraft," 2000.
- [3] A. C., "'A380: 'More Electric' Aircraft'," October 2001.
- [4] J. A. Weimer, "The role of electric Machine and drives in the more electric aircraft," in , Madison.
- [5] M. Khatre and A. G. Jack, "Simulation of PMSM VSI Drive for Determination of the Size Limits of the DC-Link Capacitor of Aircraft Control Surface Actuator Drives," in , 2006.
- [6] D. R. Trainer and C. R. ,. Whitley, "Electric actuation-power quality management of aerospace flight control systems," in .
- [7] P. A. Robson, et al., "The impact of matrix converter technology on motor design for an integrated flight control surface actuation system," in , 2003.
- [8] T. f. e. Wikipedia. (2013,) Wikipedia. [Online]. [http://commons.wikimedia.org/wiki/File:Ram Air Turbine on F-104S Starfighter \(14199964717\).jpg](http://commons.wikimedia.org/wiki/File:Ram_Air_Turbine_on_F-104S_Starfighter_(14199964717).jpg)
- [9] M. A. Maldonado and G. J. Korba, "Power management and distribution system for a more-electric aircraft (MADMEL)".
- [10] A. G. Boulanger, A. C. Chu, S. Maxx, and D. L. Waltz, "'Vehicle Electrification: Status and Issues". Proceedings of the IEEE, 2011, vol. 99, no. 6, pp. 1116-1138."
- [11] A. Tenconi and P. Wheeler, "'Introduction to the Special Section on The More Electric Aircraft: Power Electronics, Machines, and Drives", IEEE Trans. Ind. Electron., 2012, Vol. 59, No. 9, pp. 3521-3522."
- [12] A. Avizienis, J. .-C. Laprie, B. Randell, and C. Landwehr, "'Basic concepts and taxonomy of dependable and secure computing" IEEE Trans. on Dependable and Secure Computing, vol. 1, 2004."

- [13] "Advisory Council for Aeronautics Research in Europe, "Strategic Research Agenda", Volume 1, Oct. 2002."
- [14] "ICAO, "International Standard and Recommended Practices - Environmental Protection", Annex 16 to the Convention on International Civil Aviation, Volume II Aircraft Engine Emissions, Third Edition, Jul. 2008."
- [15] G. M. D., et al., ""Initial Assessment of Open Rotor Propulsion Applied to an Advanced Single-Aisle Aircraft", AIAA 2011-7058, 11th AIAA Aviation Technology, Integration, and Operation (ATIO) Conf., 20-22 Sept. 2011."
- [16] L. Larsson and T. a. K. K. G. Gronstedt, ""Conceptual Design and Mission Analysis for a Geared Turbofan and an Open Rotor Configuration", ASME GT2011-46451."
- [17] M. D. Guynn, B. J. J., K. L. Fisher, W. J. ,. T. M. T. Haller, and T. D. R., ""Analysis of Turbofan Design Options for an Advanced Single-Aisle Transport Aircraft", AIAA 2009-6942, 9th AIAA Aviation Technology, Integration, and Operations (ATIO) Conf."
- [18] R. N. Argile, B. C. Mecrow, D. J. Atkinson, A. G. Jack, and P. Sangha, " "Reliability Analysis of Fault Tolerant Drive Topologies", Conf. Rec. PEMD, 2008, pp. 11-15."
- [19] B. J.W., B. C. Mecrow, D. J. Atkinson, and G. J. Atkinson, ""Safetycritical design of electromechanical actuation systems in commercial aircraft", IET-Electr. Power Appl., 2011, vol. 5, no. 1, pp. 37-47."
- [20] X. Roboam, " "New trends and challenges of electrical networks embedded in More Electrical Aircraft", Conf. Rec. IEEE-ISIE, 2011, pp. 26-31."
- [21] B. A., C. A., T. A., and V. S, " "Key design aspects of electrical machines for high-speed spindle applications." IEEE IECON 2010."
- [22] G. Scutaru, A. Negoita, and R. M. Ionescu, ""Three-phase induction motor design software". IEEE International Conference on Automation Quality and Testing Robotics AQTR 2010, Vol 3."
- [23] W. Cai, "Comparison and Review of electric machines for integrated starter Alternator applications."
- [24] A. Tani, et al., "Dynamic Stator Current Sharing in quadruple Three-Phase Induction Motor Drives," *IECON*, 2013.

- [25] "IEEE Standard "Test Procedure for Polyphase Induction Motors and Generators" (ANSI), IEEE Std. 112-2004".
- [26] Boglietti, A. Cavagnino, L. Ferraris, and M. Lazzari, ""Skin effect experimental validations of induction motor squirrel cage parameters", *COMPEL Journal*, Vol. 29, No. 5, 2010, pp. 1257-1265".
- [27] E. LEvi, R. Bojoi, F. Profumo, H. A. Toliyat, and S. Williamson, "Multiphase induction motor drives - a technology status review".
- [28] E. Levi, "Multiphase electric machines for variable-speed applications," May 2008.
- [29] M. J. D. W. P. H. N. A. R. E. L. M. J. H.S. Che, "DC-link voltage balancing of six-phase wind energy systems with series-connected machine-side converters and NPC grid-side converter," *IECON 2012*, Oct. 2012.
- [30] A. Tessarolo and C. Bassi, "Stator harmonic currents in VSI-fed synchronous motors with multiple three-phase armature windings," *IEEE Trans. on Energy Conversion*," Dec. 2010.
- [31] A. Tessarolo, G. Zocco, and C. Tonello, "Design and testing of a 45-MW 100-Hz quadruple-star synchronous motor for a liquefied natural gas turbo-compressor drive," 2011.
- [32] F. Scuiller, J. F. Charpentier, and E. Semail, "Multi-star multi-phase winding for a high power naval propulsion machine with low ripple torques and high fault tolerant ability," 2010.
- [33] B. C. M. G. J. A. J. W. B. D. J. A. W. Cao, "Overview of electric motor technologies used for More Electric Aircraft (MEA)," Sep. 2012.
- [34] A. Cavagnino, Z. Li, A. Tenconi, and S. Vaschetto, "Integrated generator for More Electric Engine: design and testing of a scaled size prototype," *ECCE 2012*, 2012.
- [35] T. A. L. Y. Zhao, "Space vector PWM control of dual three-phase induction machine using vector space decomposition".
- [36] A. T. P. S. D. O. G. Grandi, "Multi-phase multi-level AC motor drive based on four three-phase two-level inverters," *SPEEDAM 2010*, 2010.
- [37] L. B. D. H. A. K. A. R. K. Marouani, "A new PWM strategy based on a 24-sector vector space decomposition for a six-phase VSI-fed dual stator induction motor," *IEEE Trans.*, May 2008.

- [38] G. S. A. T. G. Grandi, "Space vector modulation of nine-phase voltage source inverters based on three-phase decomposition," *EPE 2007*, Sep. 2007.
- [39] J. Rodriguez, M. Rivera, J. W. Kolar, and P. W. Wheeler, "A Review of Control and Modulation Methods for Matrix Converters," *IEEE Trans. on Industrial Electronics*, Jan. 2012.
- [40] A. Alesina and M. Venturini, "Solid-state power conversion: a Fourier analysis approach to generalized transformer synthesis," *IEEE Trans. on Circuits and Systems*, vol. 28, No. 4, pp. 319-330, April 1981".
- [41] A. Alesina and M. G. B. Venturini, "Analysis and design of optimum-amplitude nine-switch direct AC-AC converters," *IEEE Trans. on Power Electronics*, vol. 4, pp. 101-112, January 1989.
- [42] P. D. Ziogas, S. I. Khan, and M. H. Rashid, "Analysis and design of forced commutated cycloconverter structures with improved transfer characteristics," *IEEE Trans. on Industrial Electronics*, vol. 33, No. 3, pp. 271-280, August 1986."
- [43] L. Huber and D. Borojevic, "Space vector modulation with unity input power factor for forced commutated cycloconverters," in *Proc. IEEE IAS Conf.*, 1991, pp. 1032-1041."
- [44] L. Huber and D. Borojevic, "Space vector modulated three-phase to three-phase matrix converter with input power factor correction," *IEEE Trans. on Industry Applications*, Vol. 31, No. 6, pp. 1234-1246, Nov./Dec. 1995".
- [45] D. Casadei and G. Serra, "Reduction of the input current harmonic content in matrix converters under input/output unbalance," *IEEE Trans. on Industrial Electronics*, vol. 45, No. 3, pp. 401-411, June 1998."
- [46] Y. D. Yoon and S. K. Sul, "Carrier-based modulation technique for matrix converter", *IEEE Trans. on Power Electronics*, Vol. 21, No.6, pp. 1691-1703, Nov. 2006."
- [47] S. Muller, U. Ammann, and S. Rees, "New time-discrete modulation scheme for matrix converters," *IEEE Trans on Industrial Electronics*, Vol. 52, No 6, pp. 1607 - 1615, Dec. 2005."
- [48] M. Rivera, C. Rojas, P. W. J. Rodriguez, and J. E. B. Wu, "Predictive Current Control With Input Filter Resonance Mitigation for a Direct Matrix Converter", *IEEE Trans. on Power Electronics*, Vol. 26, No. 10, October 2011, pp. 2794-

2803."

- [49] D. Casadei, G. Serra, A. Tani, and L. Zarri, "Matrix converter modulation strategies: a new general approach based on space-vector representation of the switch state", IEEE Trans. on Industrial Electronics, Vol. 49, No. 2, pp. 370-381, April 2002."
- [50] K. Kobravi, R. Iravani, and H. A. Kojori, "Three-Leg/Four-Leg Matrix Converter Generalized Modulation Strategy – Part I: A New Formulation", IEEE Trans. on Industrial Electronics, Vol. 60, No. 3, March 2013, pp. 848-859."
- [51] P. Nielsen, F. Blaabjerg, and J. K. Pedersen, "Space vector modulated matrix converter with minimized number of switchings and a feedforward compensation of input voltage unbalance", in Proc. PEDES Conf., 1996, pp. 833-839."
- [52] L. Helle and S. Munk-Nielsen, "A novel loss reduced modulation strategy for matrix converters", in Proc. IEEE PESC Conf., 2001, pp. 1102-1107."
- [53] M. Apap, J. C. Clare, P. W. Wheeler, and K. J. Bradley, "Analysis and comparison of AC-AC matrix converter control strategie", in Proc. IEEE PESC Conf., 2003, Vol. 3, pp. 1287-1292."
- [54] L. Helle, K. B. Larsen, A. H. Jorgensen, and S. Munk-Nielsen, "Evaluation of modulation schemes for three-phase to three-phase matrix converters", IEEE Trans. on Industrial Electronics, Vol. 51, No. 1, pp. 158-171, Feb. 2004."
- [55] F. Bradaschia, M. C. Cavalcanti, F. A. S. Neves, and H. E. P. d. Souza, "A Modulation Technique to Reduce Switching Losses in Matrix Converters", IEEE Trans. on Industrial Electronics, Vol. 56, No. 4, April 2009, pp. 1186-1195."
- [56] K. Kobravi and R. Iravani, "A novel modulation strategy to minimize the number of commutation processes in the matrix converter", Proc. of ECCE 2010, pp. 1867-1874."
- [57] H.-H. Lee, Hoang, and M. Nguyen, "An Effective Direct-SVM Method for Matrix Converters Operating With Low-Voltage Transfer Ratio", IEEE Trans. on Power Electronics, Vol. 28, No. 2, February 2013, pp. 920-929."
- [58] J. Igney and M. Braun, "A new matrix converter modulation strategy maximizing the control range," Proc. of PESC 2004, Vol.4, pp. 2875 - 2880."
- [59] J. Igney and M. Braun, "Space vector modulation strategy for conventional and indirect matrix converters", Prof. of EPE

2005, Dresden, Germany, 2005, pp.1-10, CD-ROM."

- [60] M. Braun and A. Stahl, "Enhancing the control range of a matrix converter with common mode free output voltage", Proc. of Optim 2008, Brasov, 22-24 May 2008, pp. 189 - 195."
- [61] S. Tanaka and T. Takeshita, "Controllable range expansion of input power factor for matrix converters reducing the number of commutations", Proc. of ICEMS 2009, Tokyo, 15-18 Nov. 2009, pp. 1-6."
- [62] Y. Lu, H. L. Hess, and B. K. Johnson, "Implementation and test of an optimization-based space vector modulation method for the 3 ϕ -3 ϕ matrix converter", Proc. of IEMDC 2009, pp. 152 - 157."
- [63] H. H. Lee, H. M. Ngutwn, and T.-W. Chun, "Input power factor compensation algorithms using a new direct-SVM method for matrix converter", IEEE Trans. on Industrial Electronics, Vol. 58, No. 1, Jan. 2011, pp. 232-243."
- [64] L. Zarri, M. Mengoni, and J. Ojo, "Improvement in the control range of matrix converters", Proceeding of the IEEE ECCE2012, Energy Conversion Congress and Exposition, Phoenix, Arizona, Sept. 17-22, 2011, pp. 529-536."
- [65] H. Hojabri, H. Mokhtari, and L. Chang, "A generalized technique of modeling, analysis, and control of a matrix converter using SVD", IEEE Transactions on Industrial Electronics, Vol. 58, No. 3, March 2011, pp. 949 - 959."
- [66] F. Shafmeister and J. W. Kolar, "Novel Hybrid Modulation Schemes Significantly Extending the Reactive Power Control Range of All Matrix Converter Topologies with Low Computational Effort", IEEE Trans. on Industrial Electronics, Vol. 59, No. 1, January 2012, pp. 194-210."
- [67] H. Mao, C. Y. Lee, D. Boroyevich, and S. Hiti, "Review of high performance three-phase power-factor correction circuits," IEEE Trans. on Ind. Electron. , vol. 44, issue 4, Aug 1997, pp. 437-446."
- [68] J. W. Kolar and T. Friedli, "The essence of three-phase PFC rectifier systems," in Proc. Telecommunications Energy Conference (INTELEC), 2011, IEEE 33rd International, Amsterdam, Oct. 2011, pp. 1-27."
- [69] B. Singh, A. C. B. N. Singh, K. Al-Haddad, and A. P. a. D. P. Kothari, "A review of three-phase improved power quality AC-DC converters," IEEE Trans. Ind. Electron., vol. 51, no. 3, pp. 641-660, June 2004".

- [70] D. G. Holmes and T. A. Lipo, "Implementation of a controlled rectifier using AC-AC matrix converter theory," IEEE Trans. Pow. Electron., Vol. 7, No. 1, Jan. 1992, pp. 240-250."
- [71] J. Kolar, M. Baumann, F. Schafmeister, and H. Ertl, "Novel three-phase ac-dc-ac sparse matrix converter - Part I: Derivation, basic principle of operation, space vector modulation, dimensioning," in APEC 2002. Conf. Expo., Dallas, TX, Mar. 2002, vol. 2, pp. 777-787."
- [72] L. Wei, T. A. Lipo, and H. Chan, "Matrix converter topologies with reduced number of switches," in Power Electron. Spec. Conf., Jun. 2002, vol. 1, pp. 57-63."
- [73] A. Odaka, et al., "A PAM control method for matrix converter based on virtual AC/DC/AC conversion method," IEEE Trans. IA., vol. 126, no. 9, pp. 1185-1192, 2006."
- [74] R. Pena, R. Cardenas, E. Reyes, J. Clare, and a. P. Wheeler, "Control strategy of an indirect matrix converter with modifying DC voltage," in Proc. Eur. Power Electron. Appl., 2009, pp. 1-8."
- [75] Y. Sun, M. Su, G. Weihua, H. Wang, and a. X. Li, "Indirect four-leg matrix converter based on robust adaptive back-stepping control," IEEE Trans. on Industrial Electronics., vol. 58, no. 9, pp. 4288-4298, Sep. 2011."
- [76] F. Schafmeister, M. Baumann, and a. J. Kolar, "Analytically closed calculation of the conduction and switching losses of three-phase ac-ac sparse matrix converters," in Proc. Int. Conf. Eur. Power Electron.- Power Electron. Motion Control, Sep. 2002, pp. 1-13."
- [77] S. Round, et al., "Comparison of performance and realization effort of a very sparse matrix converter to a voltage dc link PWM inverter with active front end," IEEE Trans. Inst. Electr. Eng. Jpn., vol. 126-D, no. 5, pp. 578-588, May 2006."
- [78] J. Schonberger, T. Friedli, S. D. Round, and J. W. Kolar, "An ultra sparse matrix converter with a novel active clamp circuit," in Proc. Power Conv. Conf., Nagoya, Japan, Apr. 2-5, 2007, pp. 784-791."
- [79] R. García-Gil, J. M. Espí, E. J. Dede, and E. Sanchis-Kilders, "A bidirectional and isolated three-phase rectifier with soft-switching operation," IEEE Trans. on Industrial Electronics, Vol. 52, No. 3, June 2005, pp. 765-773."
- [80] R. Metidji, B. Metidji, and B. Mendil, "Design and implementation of a unity power factor fuzzy battery charger using an ultrasparse matrix rectifier," IEEE Trans. on Power

Electronics, Vol. 28, No. 5, May 2013, pp. 2269-2276."

- [81] Z. Yan, K. Zhang, J. Li, and W. Wu, "A novel absolute value logic SPWM control strategy based on de-re-coupling idea for high frequency link matrix rectifier," IEEE Trans. on Industrial Informatics, Vol. 9, No. 2, May 2013, pp. 1188-1198."
- [82] K. You, D. Xiao, M. F. Rahman, and M. N. Uddin, "Applying reduced general direct space vector modulation approach of AC-AC matrix converter theory to achieve direct power factor controlled three-phase AC-DC matrix rectifier", IEEE Trans. on Industry Application. Accepted for future publication, early preprint."
- [83] J. W. K. a. F. Schafmeister, "Novel modulation schemes minimizing the switching losses of sparse matrix converters," in Proc. IEEE Conf. Ind. Electron. Soc., Nov. 2003, pp. 2085-2090."
- [84] L. Helle and S. Munk-Nielsen, "A novel loss reduced modulation strategy for matrix converters," in Proc. IEEE PESC Conf., 2001, pp. 1102-1107."
- [85] P. Nielsen, F. Blaabjerg, and J. K. Pedersen, "Space vector modulated matrix converter with minimized number of switchings and a feedforward compensation of input voltage unbalance," in Proc. PEDES Conf., 1996, pp. 833-839."
- [86] L. Helle, K. B. Larsen, A. H. Jorgensen, and S. Munk-Nielsen, "Evaluation of modulation schemes for three-phase to three-phase matrix converters," IEEE Trans. Ind. Electron., Vol. 51, No. 1, pp. 158-171, Feb. 2004."
- [87] F. Bradaschia, M. C. Cavalcanti, F. A. S. Neves, and H. E. P. d. Souza, "A modulation technique to reduce switching losses in matrix converters," IEEE Trans. Ind. Electron., Vol. 56, No. 4, Apr. 2009, pp. 1186-1195."
- [88] K. Kobravi and R. Iravani, "A novel modulation strategy to minimize the number of commutation processes in the matrix converter," Proc. of ECCE 2010, pp. 1867-1874."
- [89] J. Rodriguez, M. Rivera, J. W. Kolar, and P. W. Wheeler, "A review of control and modulation methods for matrix converters," IEEE Trans. on Industrial Electronics, Vol. 59, No. 1, Jan. 2012, pp. 58-70."
- [90] K. Kobravi, R. Iravani, and H. A. Kojori, "Three-leg/four-leg matrix converter generalized modulation strategy-Part I: a new formulation," IEEE Trans. on Industrial Electronics, Vol. 60,

No. 3, March 2013, pp. 848-859."

APPENDIX A

HARDWARE

DRIVER BOARD

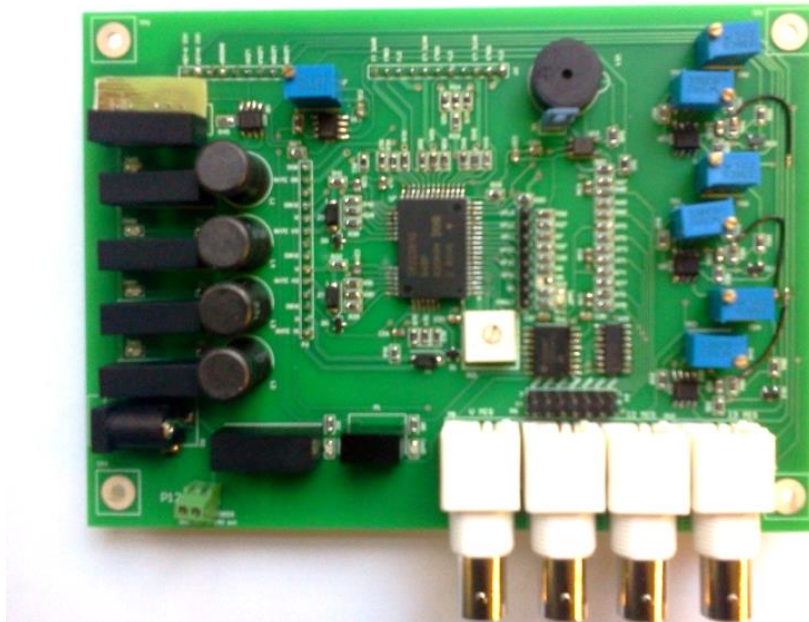
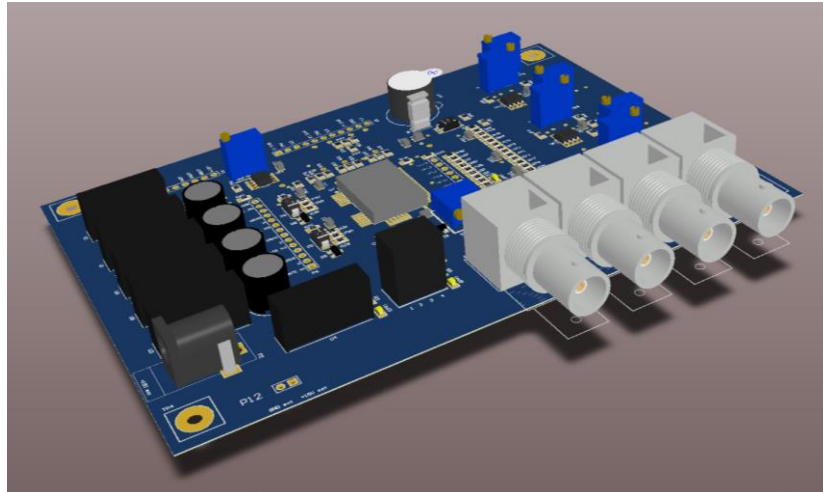
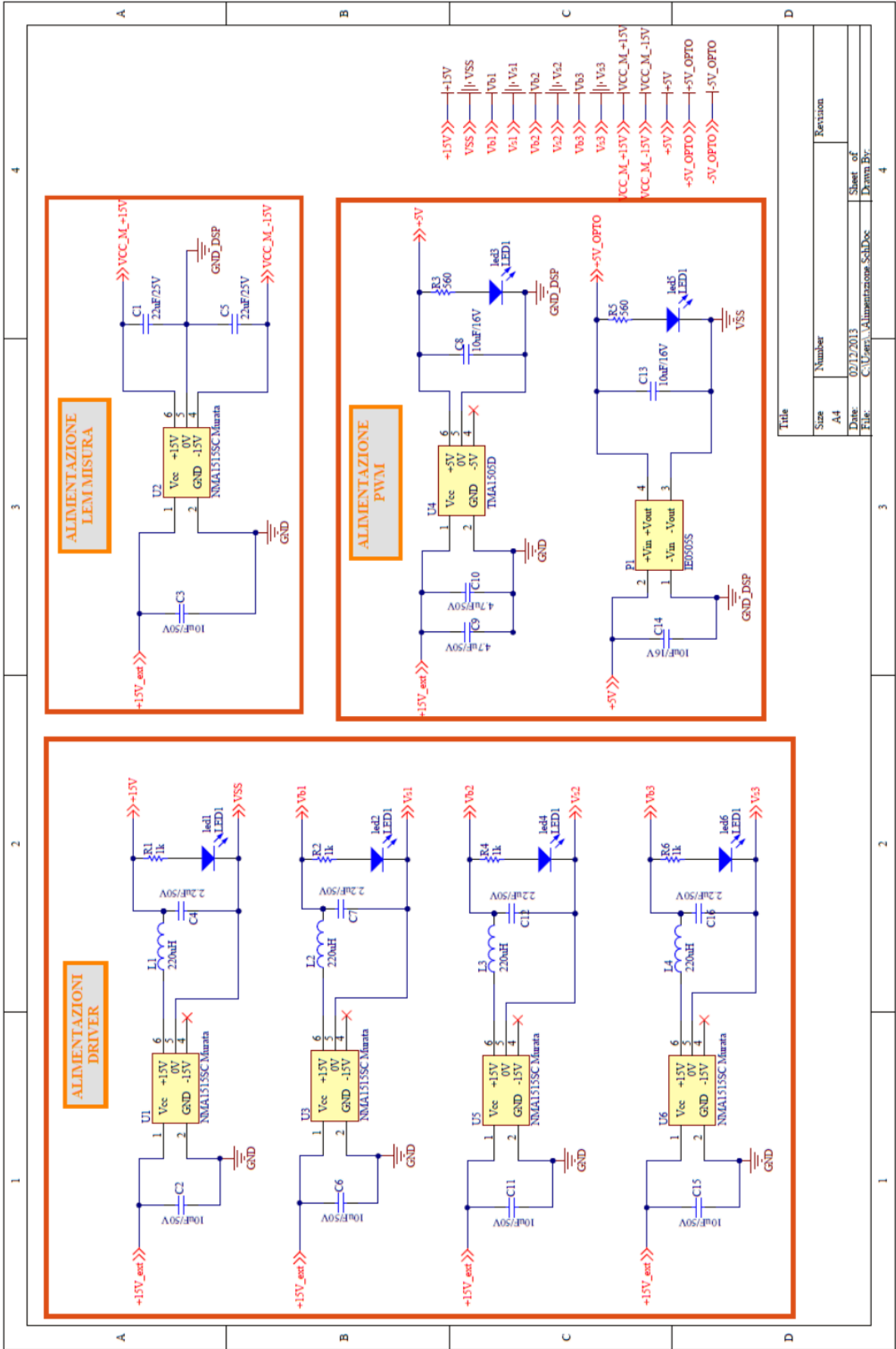
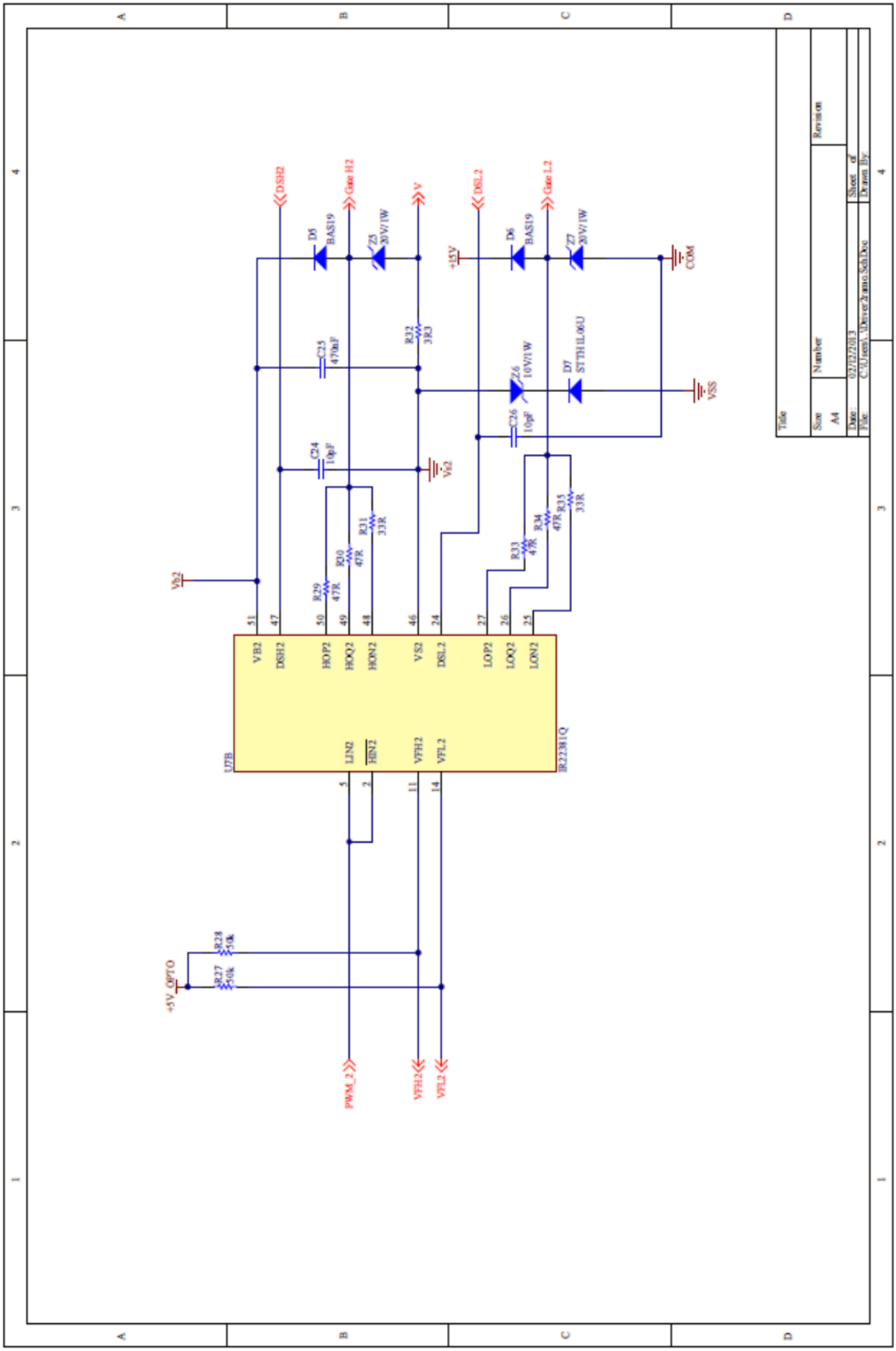


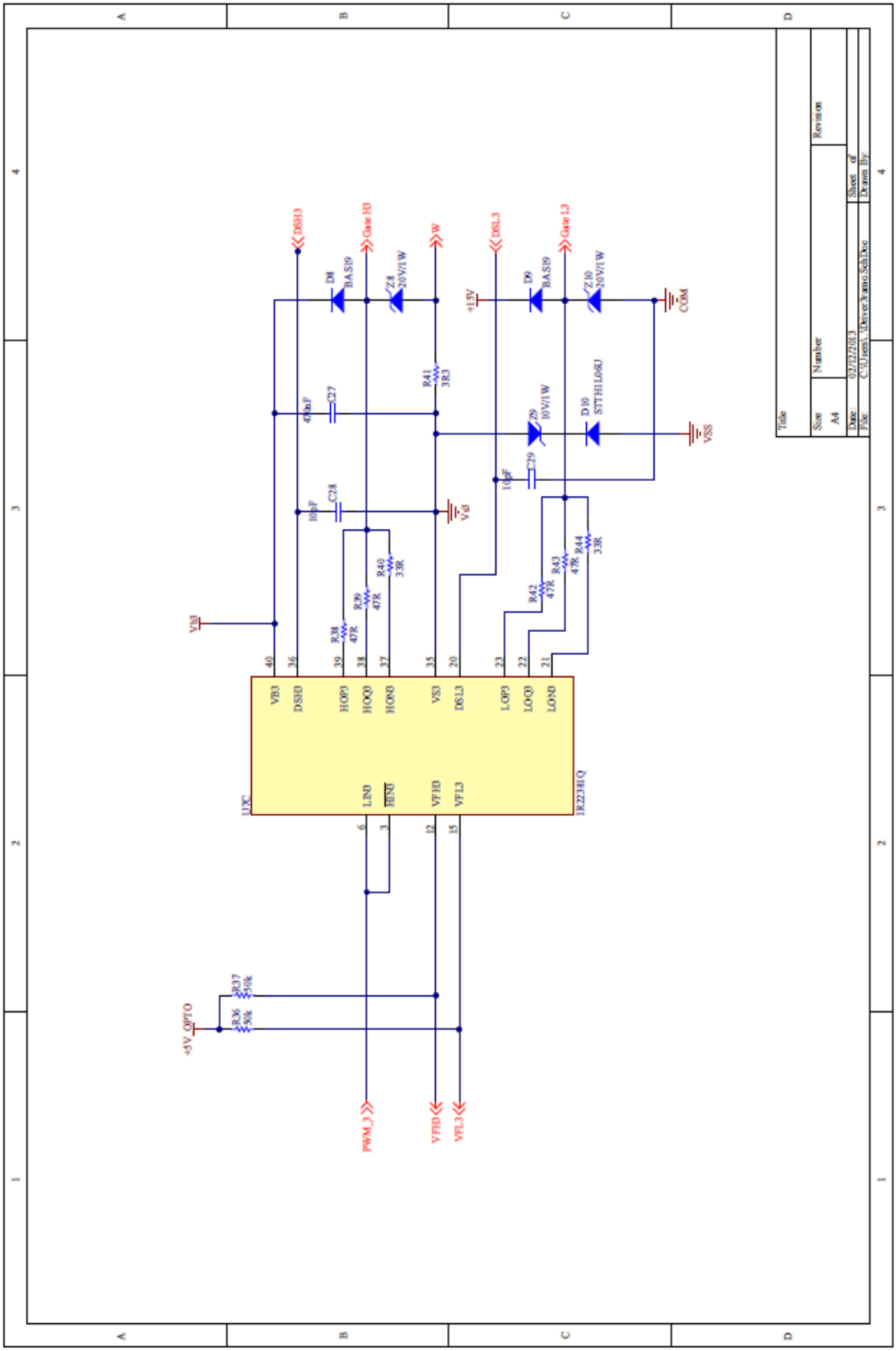
Figure A-0-1 - 3D Model and prototype PCB

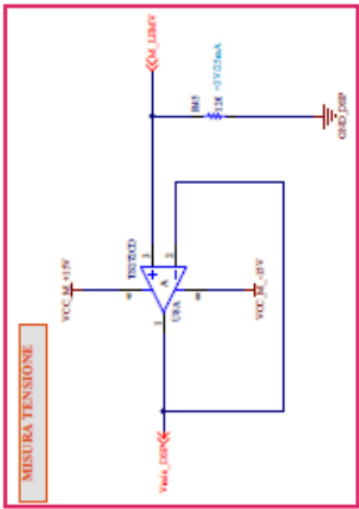


Title		Revision	
Size	Number		
A4			
Date	07/12/2013	Sheet of	
File	C:\Ugenti\Alimentazione SchDoc	Drawn By	

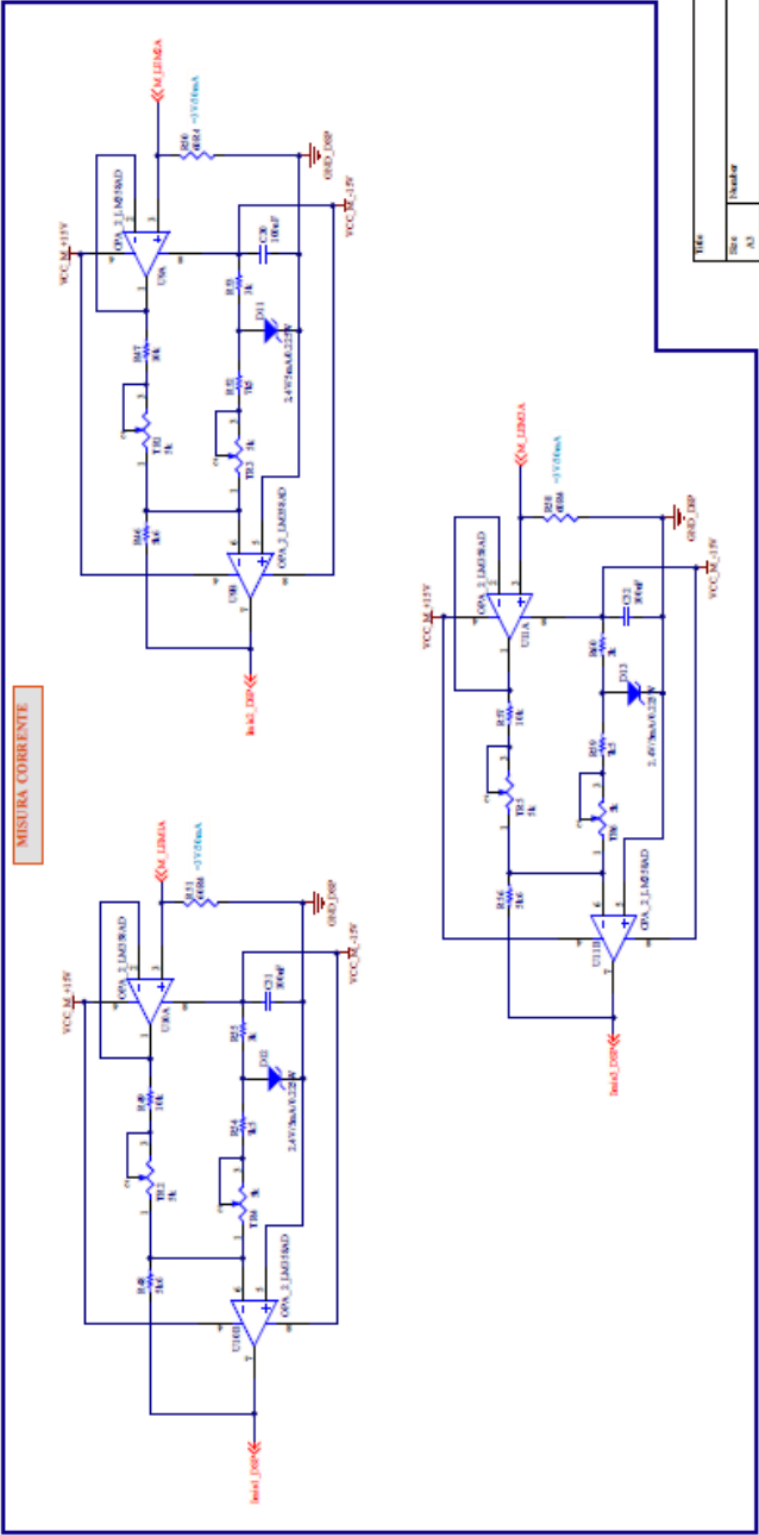


Title	
Size	Number
A4	Revision
Date: 02/02/2013	Sheet of
File: C:\Users\Uwever\Documents	Drawn by:

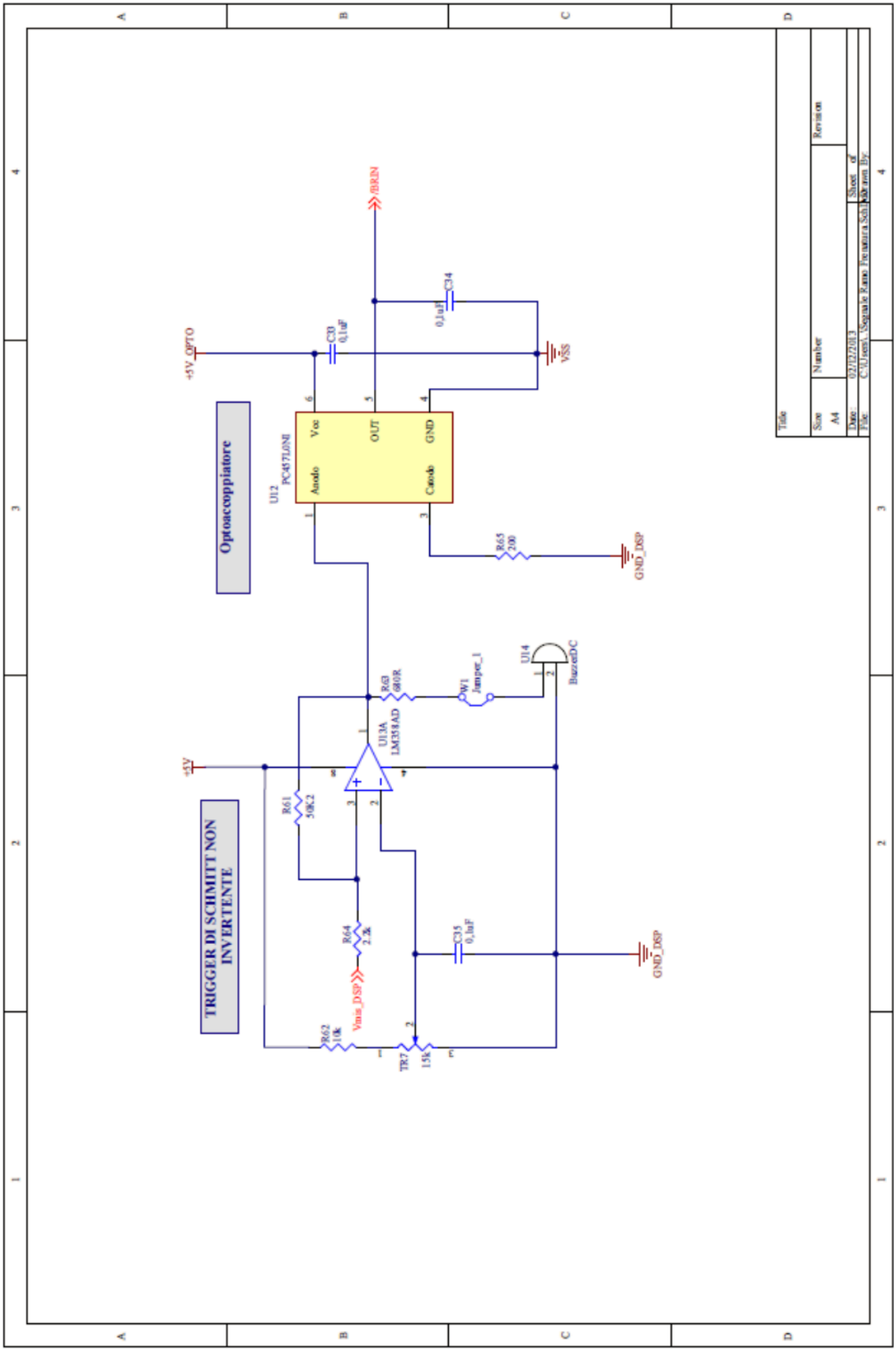




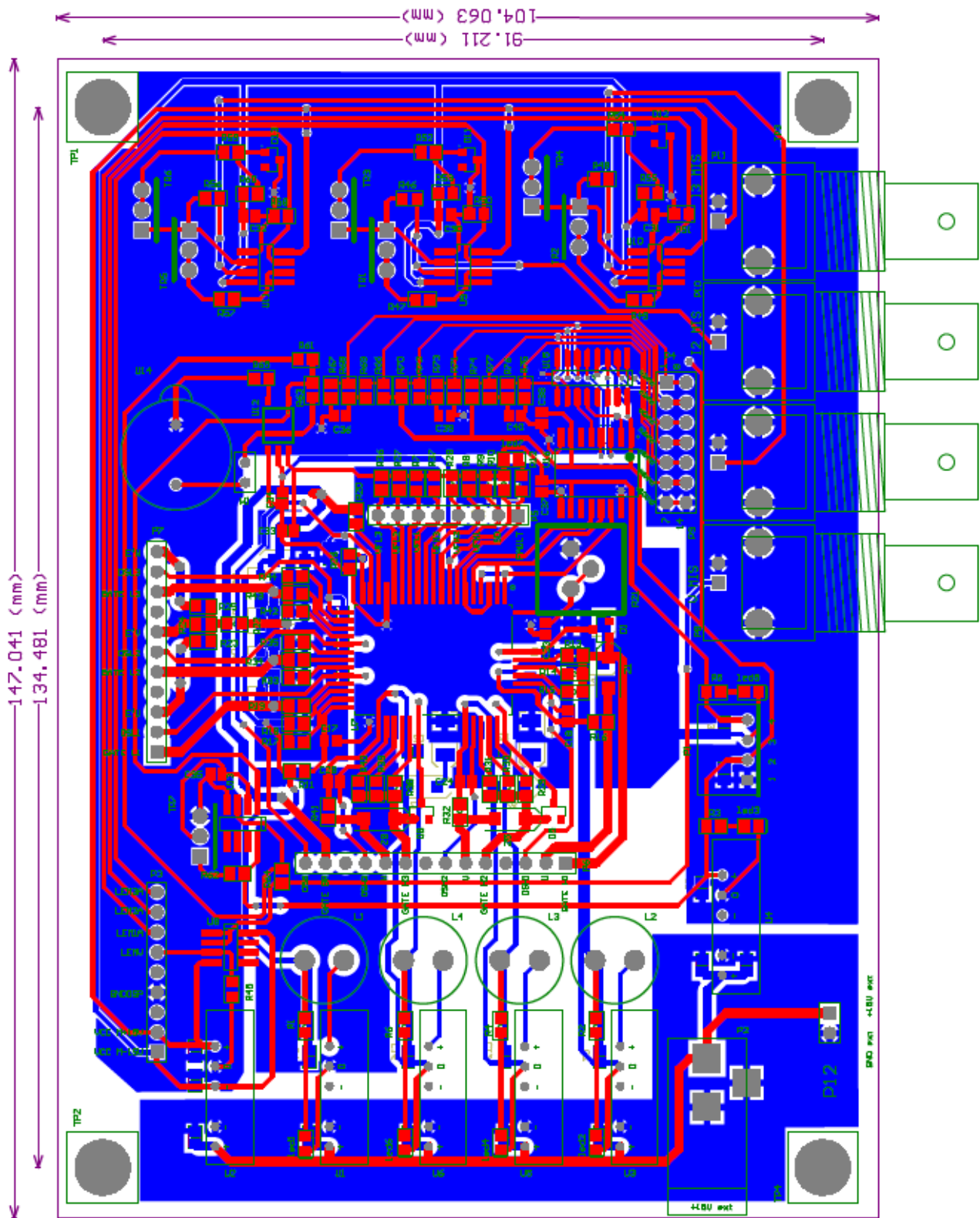
MISURA CORRENTE



Titolo			
Disegnato	Verificato	Revisione	
AS			
DATA	01/11/2023	Foglio 2	
PROG.	C:\Users\luciano\Documents\LABORATORIO	Lavoro 10	



Title	
Size	Number
A4	Revision
Date:	Sheet of
File:	Sub item for



POWER BOARD

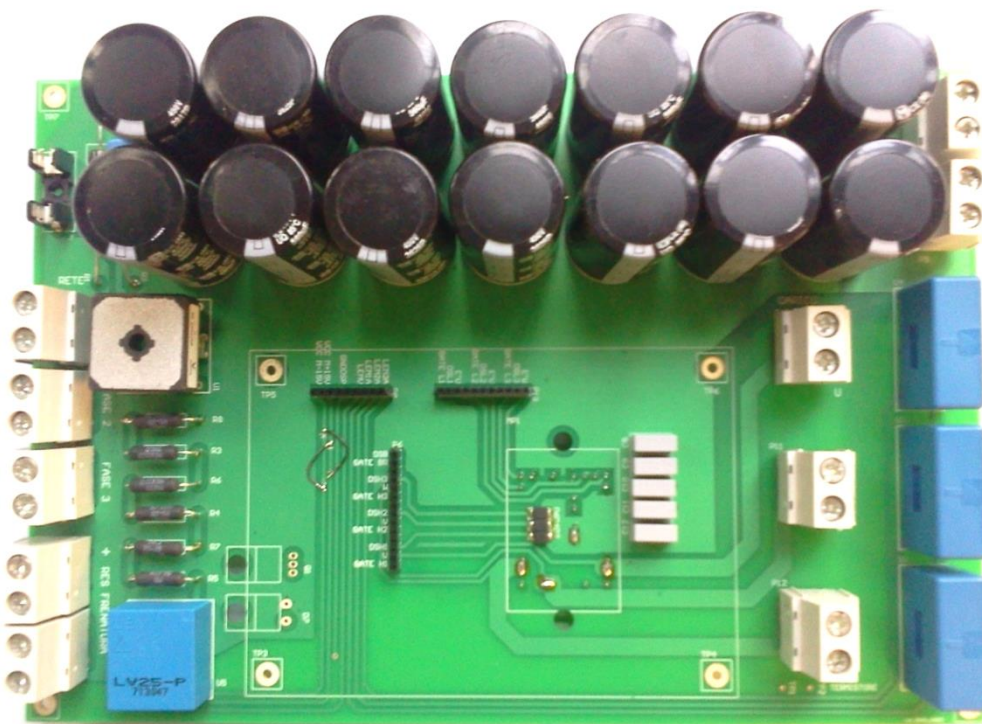
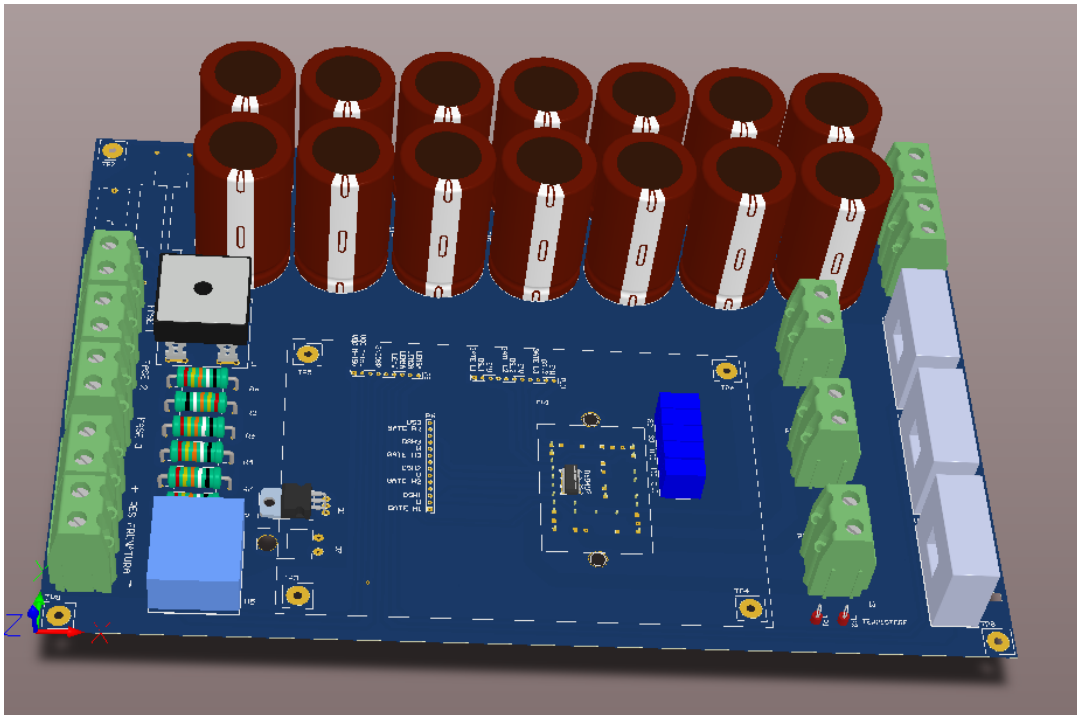
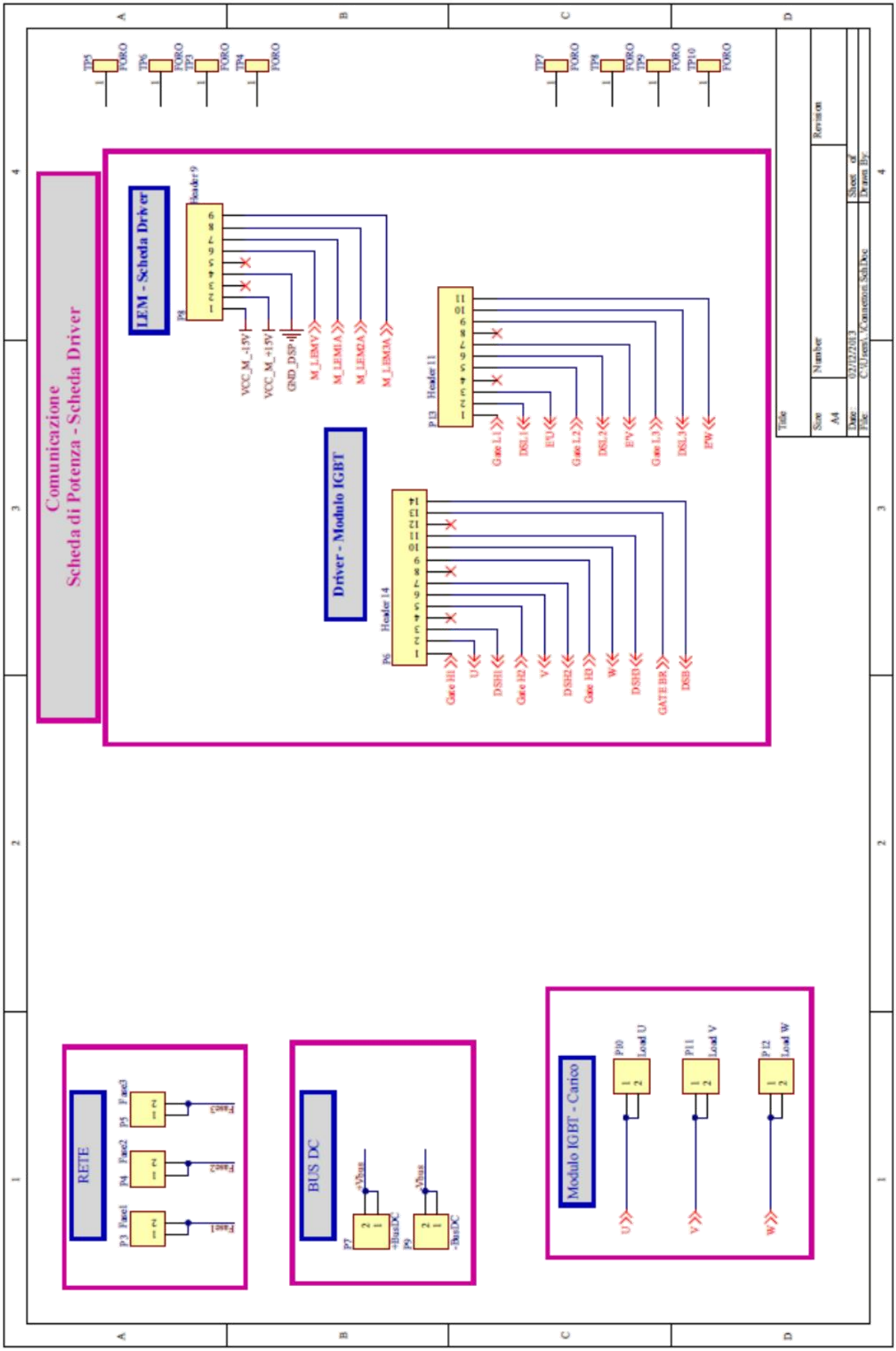
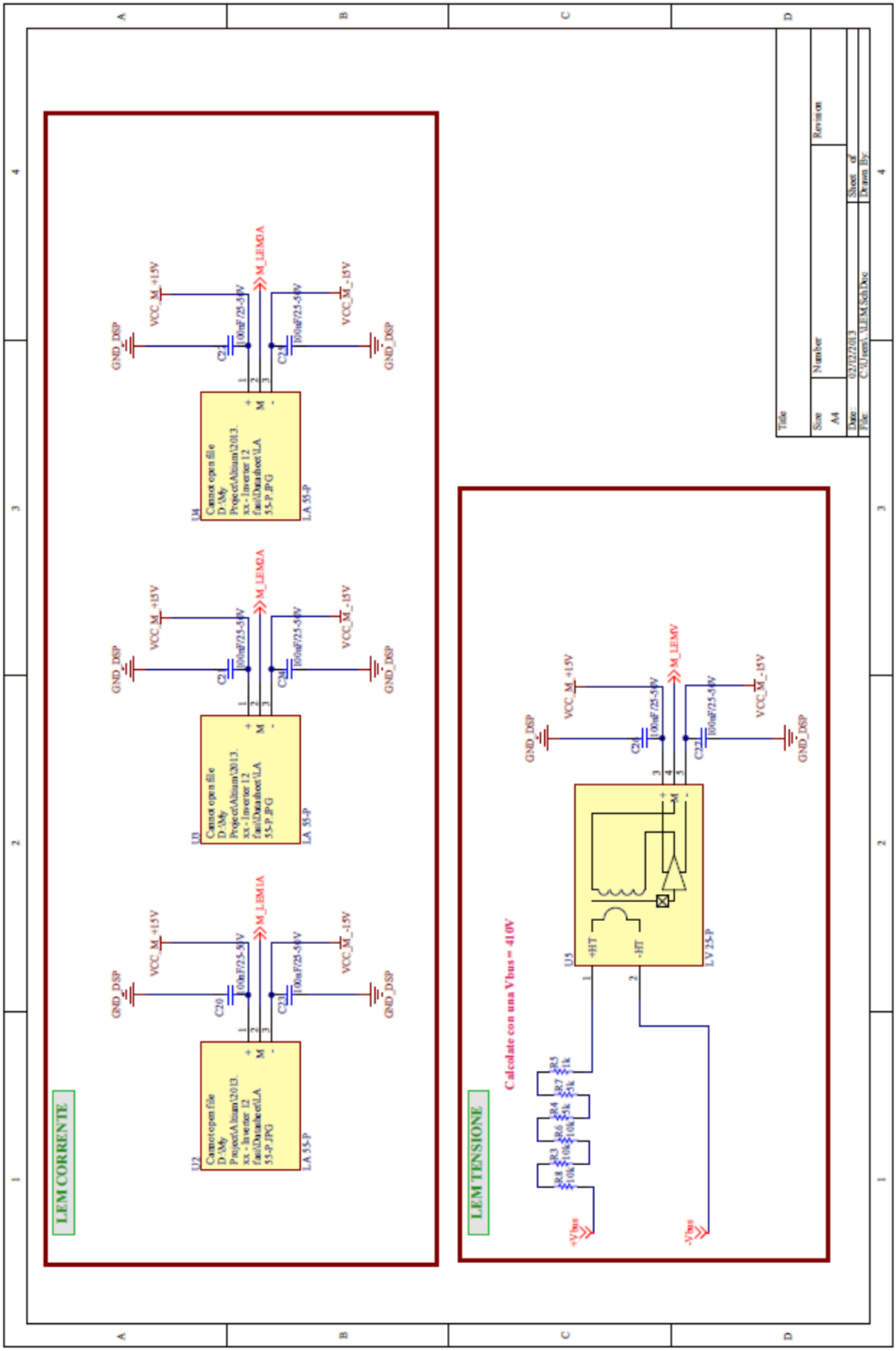


Figure 0-2 - 3D Model and prototype of power board



Title	
Size	Number
AA	AA
Date:	02/12/2013
File:	C:\Users\Commenon\Salvo
Sheet of	Revision
Drawn By:	

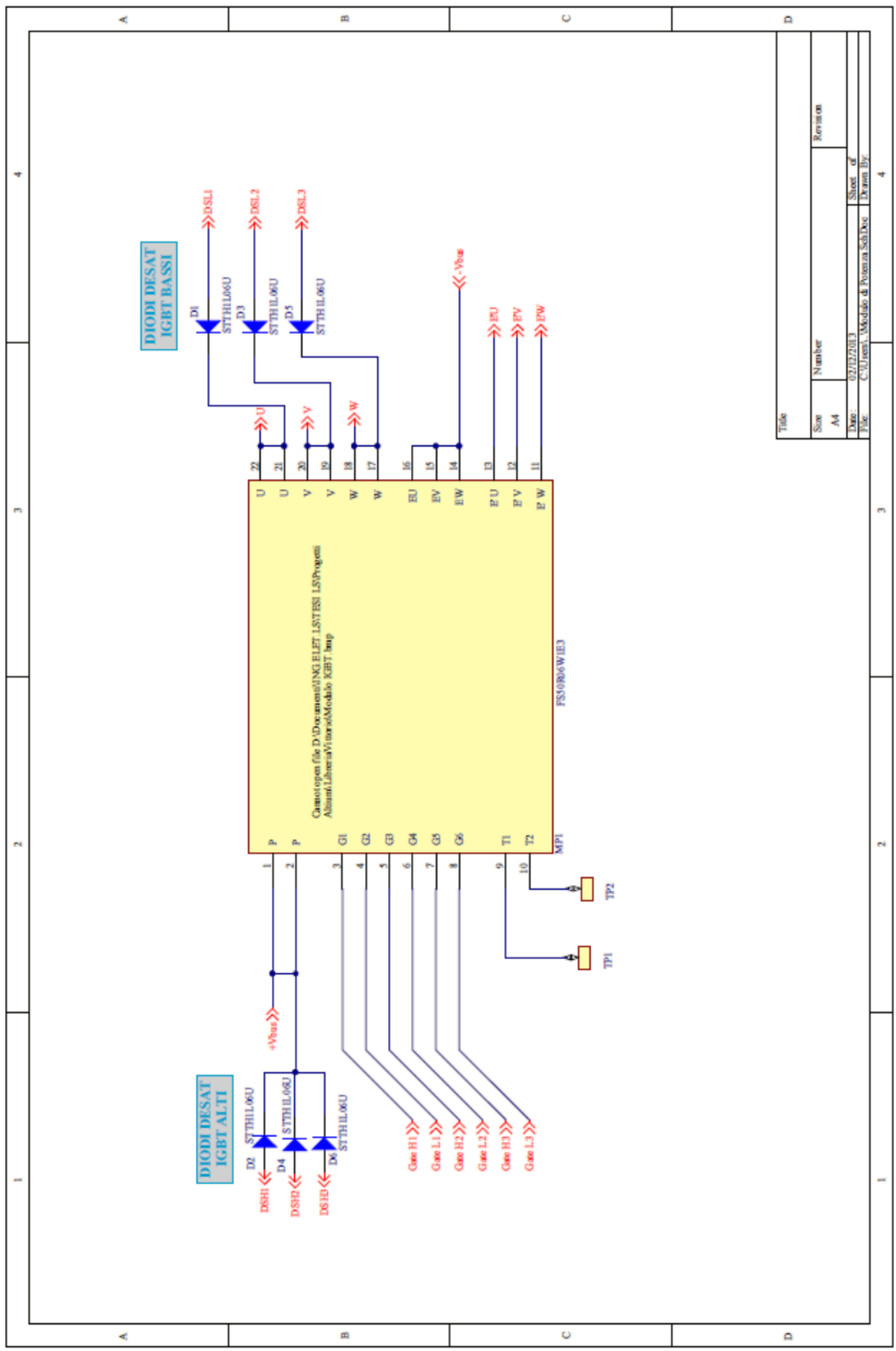


LEM CORRENTE

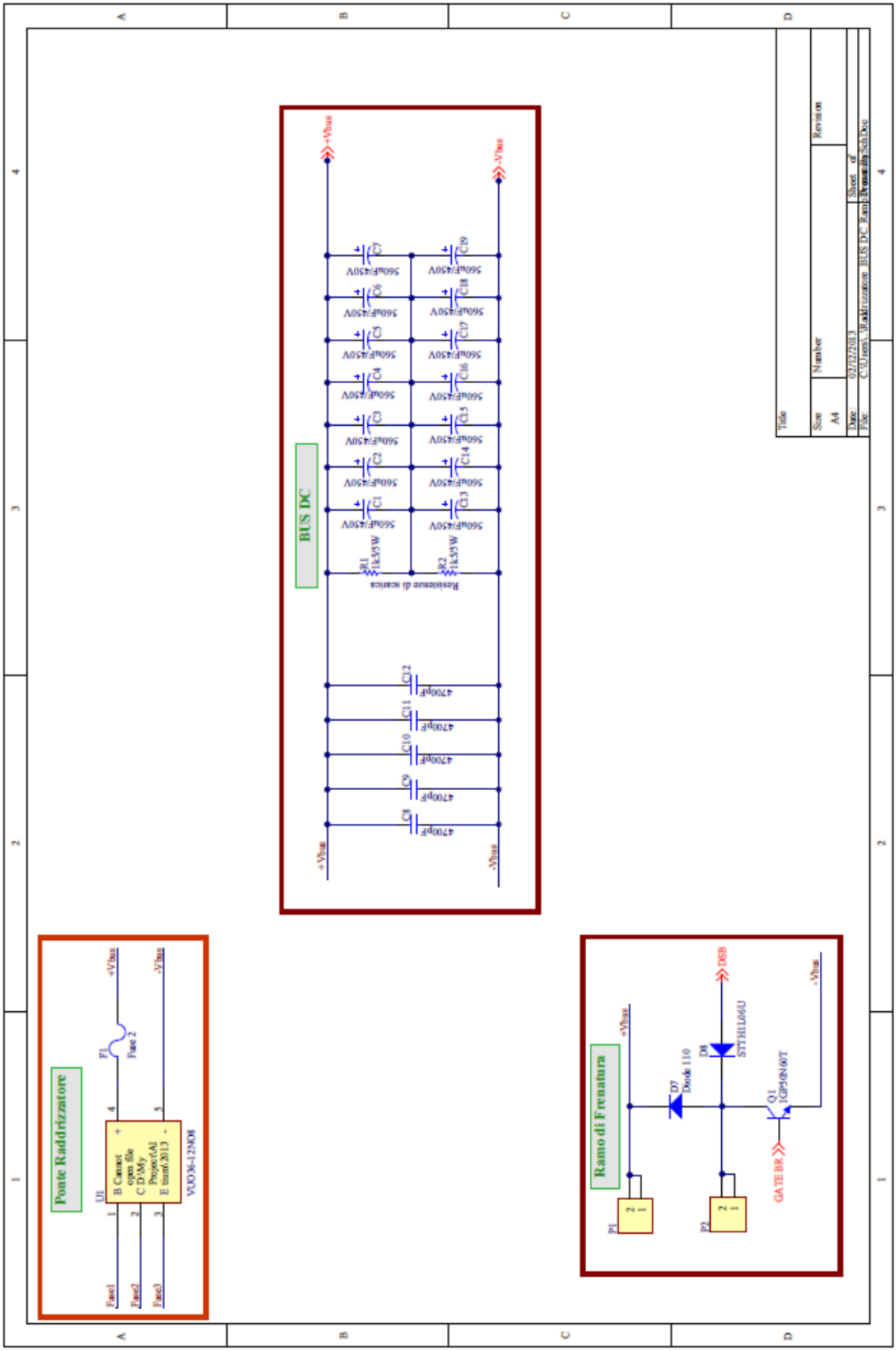
LEM TENSIONE

Calcolate con una $V_{bus} = 410V$

Title		Revision	
Size	Number		
A4			
Date:	02/02/2013	Sheet of	4
File:	C:\Users\LEMM\Documents	Drawn by:	



Title		Revision	
Size	Number		
A4			
Date:	02/02/2013	Sheet of	4
File:	C:\Users\Aldo\Documents\Modulo di Potenza Sch.Dxe	Drawn by:	



Title		Revision	
Size	Number		
AA			
Date:	02/02/2013	Sheet of	4
File:	C:\Users\giallizzano\BUS DC Ramo Frenatura\Sch.Dwg		

LIST OF PAPER OF GIANCARLO RINI

1. G. Rini, M. Mengoni, L. Zarri, A. Tani, G. Serra and D. Casadei, "[A Modulation Strategy for Matrix Converter with Extended Control Range and Reduced Switching Power Losses](#)", ECCE 2013.
2. G. Rini, A. Tani, G. Serra, M. Mengoni, L. Zarri, D. Casadei, "[Dynamic Stator Current Sharing in Quadruple Three-Phase Induction Motor Drives](#)", IECON 2013.
3. G. Rini; Mengoni, M.; Zarri, L.; Tani, A.; Serra, G.; Casadei, D., "[Modulation strategy with minimum switching losses for three-phase AC-DC matrix converters](#)", Power Electronics and Applications (EPE'14-ECCE Europe), 2014 16th European Conference